Investigation of the optical isotropy of space by refraction of light

V. V. Ragul'skiĭ
Institute of Mechanics Problems, Russian Academy of Sciences, 117526 Moscow, Russia

(Submitted 20 February 1997)
Pis'ma Zh. Éksp. Teor. Fiz. **65**, No. 7, 497–501 (10 April 1997)

It is demonstrated experimentally that the refraction of light by a condensed medium is independent of the spatial orientation of the medium to within $5\cdot10^{-8}$. © *1997 American Institute of Physics.* [S0021-3640(97)00107-2]

PACS numbers: 42.25.Gy, 42.68.Ay

According to modern theory, space is isotropic with respect to optical phenomena. On this basis it is generally accepted[1] that the refractive effect of a condensed medium on light waves propagating in opposite directions is same.[a)] However, one would like to have better experimental grounds for this view.

The problem is that thus far a direct comparison of the refractive properties of a medium for oppositely propagating light beams has been made with accuracy no better than $\sim3\cdot10^{-5}$ (see the article by Arago[3]). According to the results of observations of stars through an achromatic glass prism,[3] to the accuracy stated the index of refraction does not depend on whether the light source is located in front of or behind the prism in respect to the Earth's orbital path.

Measurements of the change in the polarization of counterpropagating light beams passing through a tilted glass plate were made in Refs. 4 and 5, and the corresponding refractive indices were calculated from the data with the use of the Fresnel formulas.[4,5] Although similar methods were employed in those studies, their results are contradictory. According to Fizeau's data,[4] if one beam propagates eastward and the other propagates westward, then the ''counter'' refractive indices are *different*, and the difference Δn is time-dependent and reaches $3\cdot10^{-4}$. But Brace[5] asserts, on the basis of his own measurements (whose error is equivalent to $\Delta n\sim4\cdot10^{-5}$), that the ''eastward'' and ''westward'' refractive indices are *identical*.

General speaking, it has not been ruled out that various factors can affect the isotropy of the observed optical processes. For example, it is assumed in the above-mentioned papers that optical isotropy may be affected by rapid motion.[b)] As is well known, the theory of relativity postulates that there is no such effect, but a postulate is not a proof. Only experiment can reveal how well the postulate corresponds to reality.

It was shown above that the aforementioned experimental results concerning the refraction of light are at variance with each other even in the fourth decimal place. In addition, they were obtained only for a few preferred azimuths. More accurate experiments could clear up this situation. This letter describes one such experiment.

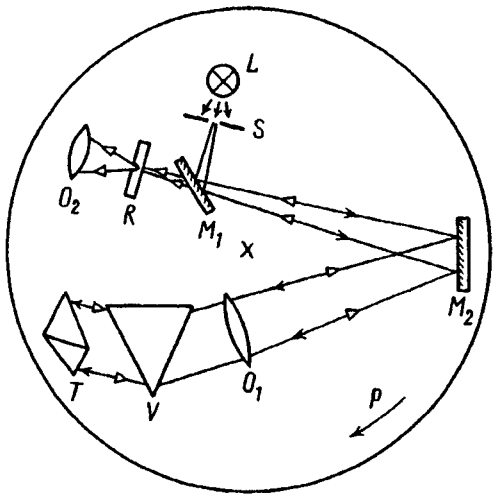

FIG. 1. Diagram of the experimental apparatus: L — incandescent lamp; S — slit 10 μm wide; O_1 — achromatic objective with a focal length of 1.5 m; V — K-8 glass prism with a refraction angle of 65°; T — glass triple prism; the light beam reflected by this prism is 5 cm in diameter; M_1 — flat half-transmitting mirror, the back side of which is coated with an antireflection coating; M_2 — flat mirror with a nontransmitting aluminum coating; R — movable glass plate with a ruled line 3 μm wide; O_2 — eyepiece with 100× magnification; P — turntable.

The idea of the experiment is as follows: Let a light beam pass through a refracting prism and then turn it by an angle of precisely 180°. Then the light will once again pass through the prism, but this time in the opposite direction. If the counter refractive indices are identical, then the counterpropagating beam will remain collinear with the initial beam even after the prism. Otherwise a deviation from collinearity proportional to Δn will appear. The problem will ultimately reduce to detecting this deviation, which can be done with high accuracy. The angular dependence of Δn can be determined by varying the spatial orientation of the optical scheme discussed above.

As we can see, such a scheme makes it possible to *measure* Δn *directly* (while in previous investigations this parameter had to be *calculated* using data on the values of the counter refractive indices). The effect of the identical parts of the counter indices is automatically compensated here. This sharply decreases the effect of the instability of the external conditions on the final results.

The main elements of the experimental arrangement are shown in Fig. 1. An electric lamp L, which illuminates a narrow slit S located in the focal plane of the objective O_1, serves as the light source. The parallel beam formed by this objective is refracted by the prism V and enters a high-quality triple prism T, i.e., into a corner reflector with three mutually orthogonal faces. It is well known that a beam incident on such a reflector is always turned by 180° irrespective of the angle of incidence. The reflected light passes through the prism V in the opposite direction and is focused by the objective O_1. Then, part of the reflected light exits through the half-transmitting mirror M_1 and is spatially

separated from the initial radiation. The mirror M_2 is inserted into this scheme in order to decrease the dimensions of the apparatus.

A thin line engraved on a plane-parallel plate R serves as a reference for determining the angular position of the beam which has passed twice through the prism. The reference line is located in the plane where this beam, when focused, produces an image of the slit S. The plate is secured to a carriage that can be moved with the aid of a micrometer screw so as to make the line merge with this image. The merging of the image and the line is monitored visually through an eyepiece O_2 with a large magnification. All elements are placed on a turntable P so that the orientation of the apparatus can be changed without rearranging the elements.

If space is anisotropic to some degree and the counter refractive indices are therefore unequal, then a rotation of the apparatus will be accompanied by a shift of the image of the slit. Indeed, suppose that for a certain position of the apparatus refractive index for the ''backward'' direction is greater than for the ''forward'' direction. In this situation the deflection of the backward beam by the prism is *greater* (by an angle $\Delta\varphi$) than that of the initial beam. A rotation of the entire apparatus by 180° reverses the orientation of the beams. Correspondingly, as a result of this operation the backward beam will be deflected *less* than the initial beam by an amount $\Delta\varphi$. The objective O_1 (with focal length f) converts angular deflections into spatial deviations. Therefore if the image of the slit is initially shifted by a distance $\Delta x \equiv f\Delta\varphi$ from the point that it would occupy in the case $\Delta n = 0$, then in the second position the displacement from this point equals $-\Delta x$. Therefore a rotation of the turntable by 180° should result in a shift of the image by $2\Delta x$.

It is easy to determine how such a shift is related to Δn. We use the fact that the index of refraction is

$$n = \sin\,\alpha/\sin\,\beta, \tag{1}$$

where α and β are the angles between the perpendicular to the interface of the media and the refracted rays measured on different sides of this boundary (in our case the surface of the prism). In the apparatus described above, the prism was placed in the position of minimum deflection. In this case, as is well known, light passes straight through the prism parallel to the base. The corresponding geometric construction gives $\beta = \gamma/2$ and $\alpha = (\varphi + \gamma)/2$. Here γ is the refracting angle of the prism and φ is the angle by which the light beam is deflected by the prism. Differentiating Eq. (1) after substituting these relations gives

$$\Delta n = \frac{\cos\,\alpha}{\sin\,\beta}\,\frac{\Delta\varphi}{2} = \frac{\sqrt{1 - n^2\,\sin^2(\gamma/2)}}{2\,\sin(\gamma/2)}\,\frac{\Delta x}{f}. \tag{2}$$

The last expression in Eq. (2) is obtained by substituting Eq. (1) and using the relation between $\Delta\varphi$ and Δx. Substituting here the known characteristics of the apparatus ($\gamma = 65°$, $n = 1.52$, $f = 1.5\cdot 10^2$ cm), we get $\Delta n = 3.6\cdot 10^{-3}\ \text{cm}^{-1}\cdot\Delta x$.

It is obvious that the smallest observable value of Δx is determined by how stable and reproducible is the position of the reference line with respect to the focused backward beam. In the scheme discussed above, instability can arise only on account of an uncontrolled variation in the relative positions of the elements S, M_1, and R. To prevent this,

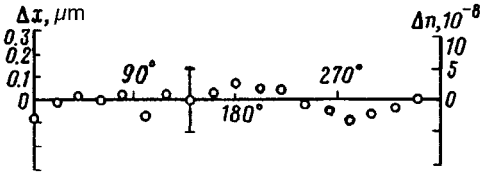

FIG. 2. Results of the determination of Δn as a function of the angle of rotation of the turntable.

these elements were secured, at small distances from one another, to the same rigid metal body, which was thermally insulated and also shielded from magnetic and electric fields. All other optical elements were covered with a sheath made of dense paper. Of course, the reinforced concrete walls of the building housing this apparatus also served as a shield from external perturbations.

Preliminary experiments showed that the angular position of the beam of interest to us can be most accurately followed according to the diffraction pattern produced when the beam strikes the reference line. The symmetry of this pattern, observed 0.5 mm from the line through the eyepiece O_2, is so sensitive to transverse shifts of the line relative to the center of the light field incident on it (and comparable to them in width) that shifts of ~ 0.1 μm are easily observable. Of course, the shifts must be recorded with an error which is just as small. To achieve this, the carriage R carrying the plate was oriented so that the carriage moves (under the action of the micrometer screw) almost parallel to the reference line: The angle between them was $\approx 1°$. Under these conditions the motion of the carriage is accompanied mainly by a longitudinal displacement of the line, which does not change the position of the line relative to the light field under study. The shift in the transverse direction is 60 times smaller. Ultimately, a displacement of the micrometer thimble by 1 mm corresponded to a transverse shift of the line by only 0.2 μm; this made it possible to perform quite accurate measurements.

The apparatus described above was used to find Δx for different positions of the turntable (separated from one another by 20°). In each position the reading on the micrometer thimble for which the line coincided with the center of the image of the slit was determined 10 times. After each measurement the reference line was shifted sideways, and a new determination was started.

The averaged results of the measurements are presented in Fig. 2. The figure also shows the standard deviation of the measurements. The position for which the initial beam passes through the prism in the northward direction was taken as the zero angle of rotation of the turntable. An angle of 90° corresponds to an eastward orientation of this beam. The units of measurement of Δx are plotted along one ordinate and the corresponding values of Δn are plotted along the other ordinate.

As we can see, the recorded deviations of this parameter from zero do not exceed the measurement error ($\approx 5 \cdot 10^{-8}$). Hence it follows that, at least to this accuracy, space is isotropic with respect to the refraction of light.

[a)]Specifically, this assumption is widely used in phase-conjugation theory and practice (see, for example, Ref. 2).
[b)]It was assumed that the Earth moves with a velocity of 30 km/s along a circumsolar orbit. Later it was found that the Sun itself moves even faster: Its velocity is ≈ 400 km/s.[6]

[1]G. G. Slyusarev, in *Encyclopedia of Physics* [in Russian], Bol'shaya Rossiĭskaya Éntsiklopediya, Moscow, 1992, Vol. 3, p. 382.
[2]V. V. Ragul'skiĭ, *Phase Conjugation in Stimulated Light Scattering* [in Russian], Nauka, Moscow, 1990.
[3]F. Arago, C. R. Acad. Sci. **36**, 38 (1853).
[4]H. Fizeau, C. R. Acad. Sci. **49**, 717 (1859).
[5]D. B. Brace, Philos. Mag. (Ser. 6) **10**, 591 (1905).
[6]G. F. Smoot, M. V. Gorenstein, and R. A. Muller, Phys. Rev. Lett. **39**, 898 (1977).

Translated by M. E. Alferieff

Efficiency of conversion of heat flux into hard x rays

L. I. Rudakov,[a)] A. B. Kukushkin, and V. S. Lisitsa
Kurchatov Institute Russian Science Center, 123182 Moscow, Russia

A. N. Starostin and I. I. Yakunin
TRINITI, 142092 Troitsk, Moscow Region, Russia

(Submitted 12 November 1996; resubmitted 5 February 1997)
Pis'ma Zh. Éksp. Teor. Fiz. **65**, No. 7, 502–506 (10 April 1997)

The efficiency of conversion of the heat flux into hard x radiation (HXR) is analyzed, via time-dependent two-temperature one-dimensional non-LTE-radiation-hydrodynamic numerical modeling, for a heat-to-radiation flux converter linked to the edge of a low-atomic-number hot Z-pinch. The domain of parameters in this scheme is found where about the same HXR yield can be achieved at values of input energy which are an order of magnitude lower than in the conventional scheme of a radially imploding plasma. © *1997 American Institute of Physics.* [S0021-3640(97)00207-7]

PACS numbers: 52.25.Nr, 52.55.Ez

FORMULATION OF THE PROBLEM

Pulsed Power Generator-based Z-pinch plasmas have proved to be an effective and prolific source of soft x rays (SXR).[1] Here a multiwire array approach to creation of a high-Z plasma provides a high efficiency of conversion of magnetic energy into SXR blackbody radiation. An alternative approach, the magnetic pressure-driven acceleration of a hollow heavy-atom plasma cylinder (the liner) and transformation of the kinetic energy into Z-pinch plasma thermal energy and radiation yield in the spectral region of the L-shell and K-shell transitions in heavy atoms (Ar, Kr, Xe) is now under investigation.[2] These energy conversion schemes have limited control of the redistribution of the radiation flux over the spectrum (specifically, toward the hard x rays (HXR)). The latter takes place because of the rather slow energy transfer from hot ions to cold electrons, which results in a long lifetime of ionization states where multiple transitions in L-shell and higher-lying atomic shells dominate. The necessity of making the emitted x-ray spectrum harder, as required for a number of scientific and technological applications which are currently being actively discussed, makes it worthwhile to seek ways of (i) speeding up the ionization process in the HXR radiator, and (ii) having more freedom in increasing the electron density (and HXR intensity, respectively) in the HXR radiator. Pursuing these goals suggests the following two-step progression of energy:

1) producing and heating the electron plasma in a conventional Z-pinch with *minimal* radiation losses, and

2) fast ''transfer'' of the resulting high electron temperature to a converter taken in the form of a conventional target which is linked to the edge of the Z-pinch plasma (i.e.,

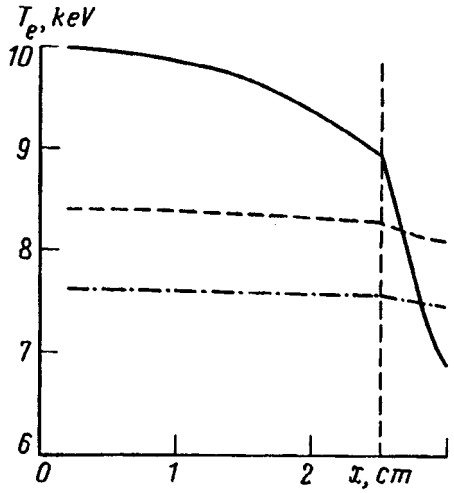

FIG. 1. Evolution of the electron temperature profile in the Z-pinch (on the left from vertical dashed line; the Z-pinch axis would be a horizontal line) and the converter (on the right) $W^{(0)}_{\rm pinch}=1.25$ MJ, $M_{\rm rad}=0.8$ mg, $l=0.5$ cm, $M_{\rm pinch}=1$ mg, $L=2.5$ cm, $S=1$ cm^2, $T^{(0)}_{\rm pinch}=15$ keV. Solid curve, 1 ns; dashed curve, 4 ns; dash-dot curve, 10 ns.

the target is situated at the point where the edge of the cylindrical Z-pinch stops at its stagnation stage, cf. Fig. 1).

The time ordering of the above two processes is possible because of strong temperature dependence of thermal flux ($\propto T_e^{7/2}$) caused by electron heat conduction. This scheme appears advantageous in the following aspects of energy progression. First, the energy cost of atom ionization $E_{\rm min}$, i.e., the sum of the ionization energies and the ion and electron thermal energies required to reach the He-like stage of the relevant element of atomic number Z, appears, for rather large Z of the radiating plasma, to be smaller, due to smaller losses on excitation (and subsequent radiation emission) during ionization. And, second, the profit in decreasing the $E_{\rm min}$ value is closely related to the faster reaching of the relevant degree of ionization (i.e., lower ''time cost'' of a He-like ion) due to higher electron temperatures at initial stage of producing the radiating plasma (cf. the thorough investigation of the time-dependent kinetics effects in Ref. 2).

In this scheme the ''load function'' is separate from the conversion of thermal energy into radiation flux. Such a separation broadens the possibilities for the ''generator–load'' matching. Indeed, the use of a light-atom gas liner instead of heavy-atom gas liner (typically, krypton) allows (i) the formation of a thicker liner and thus the achievement of a more stable regime of compression, and (ii) ''matching'' of the generator and load system with more freedom, because of weaker constraints imposed over the implosion velocity. This freedom makes it possible to optimize the radiation yield by varying the density of the radiating plasma.

The present approach called the ''Liner–Converter'' scheme has been originally proposed in the Kurchatov Institute[3] for conversion of heat flux into SXR radiation.

However it appears that this scheme is most valuable and efficient precisely for the conversion of heat into HXR radiation.

INPUT ENERGY THRESHOLD FOR PRODUCING A RADIATING PLASMA IN THE CONVERTER (''ROUGH'' OPTIMIZATION OF THE CONVERTER)

A rough estimate of the energy required for producing a radiating plasma in the converter can be made, assuming approximate equalization of the temperatures in the Z-pinch and converter (''pinch–converter thermalization'') after a short stage of target ionization and heating (this approximation is suggested by numerical simulation results; see Fig. 1 and the next section). Neglecting the radiation losses during thermalization stage, we arrive at a simple relationship between the following parameters: $W_{\rm pinch}^{(0)}$, the initial thermal energy of the Z-pinch plasma (in MJ); $M_{\rm rad}$, total mass of the gas in the converter (in mg); A, the atomic mass; $T_{\rm pinch}^{(0)}$, the initial electron temperature in the Z-pinch; $T_{\rm rad}^{(0)}$, the initial electron temperature in the converter at the HXR emission stage (or, equivalently, final temperature in the Z-pinch and converter at the thermalization stage) (in 10 keV units); $Z_{\rm rad}^{(0)}$, the initial average charge of the converter plasma at the HXR emission stage; $E_{\rm ion} \simeq 0.045[(Z-2)/10]^3$, the minimal energy (in 100 keV units) required for producing a He-like ion for an atom of atomic number Z (i.e., the sum of respective ionization potentials):

$$W_{\rm pinch}^{(0)}(1-T_{\rm rad}^{(0)}/T_{\rm pinch}^{(0)}) \sim 9.6(M_{\rm rad}/A)[1.5(Z_{\rm rad}^{(0)}/10)T_{\rm rad}^{(0)}+E_{\rm ion}], \quad (1)$$

where we omitted the losses to atomic/ionic excitation during ionization because of their relative smallness, as mentioned above.

The optimal value of $Z_{\rm rad}^{(0)}$ for HXR radiating converter (in K_α lines) should be close to the atomic number Z (specifically, $Z_{\rm rad}^{(0)} \approx Z-2$). The value of optimal Z can be evaluated from the fact that the relatively slow evolution of temperatures and ionization balance at the HXR emission stage makes the values of $Z_{\rm rad}^{(0)}$ and $T_{\rm rad}^{(0)}$, related to each other in a way which scales rather close to the coronal equilibrium average charge $\langle Z \rangle$ at a temperature T (cf. Ref. 4).

Using Eq. (1), one may evaluate optimal mass $M_{\rm rad}$ of the converter gas for given values of optimal temperature and atomic number Z. The latter values are determined, in turn, by the desired spectral range of the radiation. Thus, for $\hbar\omega > 10$ keV (and correspondingly, $Z > 30$) a krypton slab seems to be an optimal converter. Here, one has $T_{\rm rad}^{(0)} \approx 1$, and Eq. (1) gives $M_{\rm rad} \sim W_{\rm pinch}^{(0)}$.

NUMERICAL SIMULATIONS

For evaluating the efficiency of the Liner–Converter scheme and comparing it with that of the conventional Z-pinch scheme, numerical simulations are carried out for both these schemes, for various values of input energy Q (or, equivalently, $W_{\rm pinch}^{(0)}$), with the help of numerical code SS-9 (Ref. 5), which treats self-consistently the level population kinetics, radiative transfer, and gasdynamics (see also Ref. 6).

The HXR yield is calculated in a certain spectral region, integrated over certain time interval $\Delta t_{\rm rad}$. The radiation kinetics allows for the ionization states from Ne-like to H-like ions. For H-, He- and Li-like ions the excited atomic levels, up to the $n=5$ level,

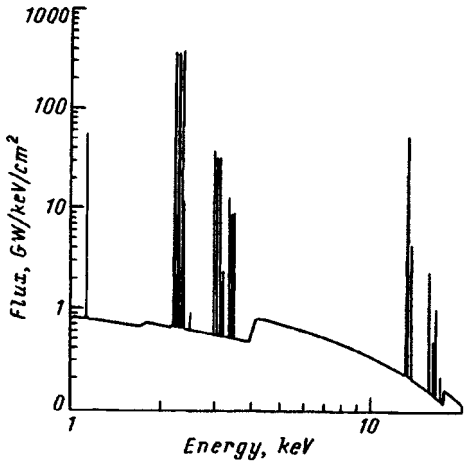

FIG. 2. Spectral distribution of radiation flux from free surface of Kr converter at $t=6$ ns (in double logarithmic scale) for $l=0.2$ cm and all other parameters from Fig. 1.

are taken into account, with allowance for the fine structure of the $2P$ levels in the Li-like ions. Each line is covered by at least a 15-point spectral mesh. We present here the results of calculations which do not allow for gasdynamics. The simulations are carried out for the following conditions:

a) conventional Z-pinch scheme: plasma column (cylinder, length L, square S) of a heavy-atom gas (krypton, total mass $M_{\rm rad}$);

b) Liner–Converter scheme: plasma slab (thickness l) of a heavy-atom gas (krypton, total mass $M_{\rm rad}$) linked to plasma slab of a light-atom gas (nitrogen, total mass $M_{\rm pinch}$, initial electron and ion temperature $T^{(0)}_{\rm pinch}$). A slab geometry of the Z-pinch plasma is chosen in order to simplify the simulations, though the final results for the radiation yield are presented for an equivalent cylindrical geometry with the same cross section S of the Z-pinch.

The results, are presented in terms of (i) the spectral distribution of radiation flux (for the Liner–Converter scheme at specific time, $t=6$ ns, shown in Fig. 2), (ii) time-integrated (from zero to a current time t) and frequency-integrated (from zero to a current value ω) radiation flux, $Q_{\rm rad}(t,\omega)$ (for the Liner–Converter and conventional Z-pinch schemes shown in Fig. 3), and (iii) time-integrated HXR yield, $Q_{\rm HXR}$, which allows for the photon energies $\hbar\omega>12.5$ keV (see numbers below).

The input and HXR output parameters in the case of a 60-MA driver are as follows:

a) $W^{(0)}_{\rm pinch}=10$ MJ, $M_{\rm rad}=15$ mg, $L=5$ cm, $\Delta t_{\rm rad}=10$ ns, $S=1$ cm^2, $Q_{\rm HXR}=890$ kJ; and $S=4$ cm^2, $Q_{\rm HXR}=84$ kJ;

b) $W^{(0)}_{\rm pinch}=10$ MJ, $M_{\rm rad}=4$ mg, $l=0.4$ cm, $M_{\rm pinch}=4$ mg, $L=5$ cm, $S=1$ cm^2, $T^{(0)}_{\rm pinch}=30$ keV, $\Delta t_{\rm rad}=10$ ns, $Q_{\rm HXR}=1.6$ MJ.

Under conditions of multi-megajoule driver both numerical simulations and semi-

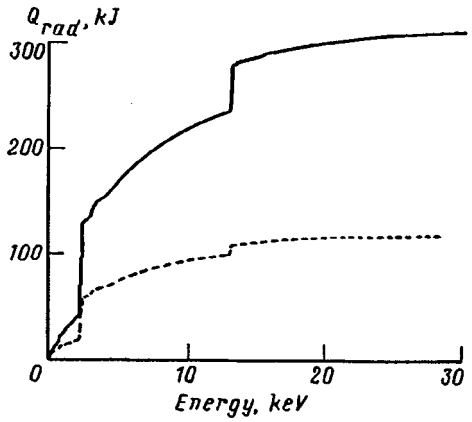

FIG. 3. Spectral distribution of time- and frequency-integrated radiation flux $Q_{\rm rad}$ at $t=10$ ns ($W^{(0)}_{\rm pinch}=1.25$ MJ) for the Liner–Converter scheme ($M_{\rm rad}=0.8$ mg, $l=0.2$ cm, $M_{\rm pinch}=1$ mg, $S=1$ cm^2, $L=2.5$ cm, $T^{(0)}_{\rm pinch}=15$ keV) (solid curve) and the conventional Z-pinch scheme ($M_{\rm rad}=1.9$ mg, $L=2.5$ cm, $S=1$ cm^2) (dashed curve).

analytical estimates show that both the Liner–Converter scheme and the conventional Z-pinch scheme attain the optimal regime of HXR emission within their own frames, though radiation yield in the conventional scheme appears to be more sensitive to the degree of plasma compression. Thus, in the conventional scheme a 70% population of He-like ions is achieved for $S=1$ cm^2 and $S=4$ cm^2 at the 5th and 8th ns, respectively, whereas for Liner–Converter scheme this happens at 1 ns. With decreasing input energy the efficiency of emission of the energy $Q_{\rm HXR}$ during relevant time period (~ 10 ns) in the HXR spectral region ($\hbar\omega > 12.5$ keV) in the conventional Z-pinch scheme goes down faster (and scales approximately as Q^2) as compared with the Liner–Converter scheme (where it scales as Q). The following comparative example illustrates this phenomenon. In this domain of lower input energies the Liner–Converter scheme attains its threshold for the optimal HXR radiator, whereas the conventional Z-pinch scheme fails to do the same:

a) $W^{(0)}_{\rm pinch}=1.25$ MJ, $M_{\rm rad}=1.9$ mg, $L=2.5$ cm, $\Delta t_{\rm rad}=10$ ns, $S=1$ cm^2, $Q_{\rm HXR}=21$ kJ; and $S=2$ cm^2, $Q_{\rm HXR}=5$ kJ;

b) $W^{(0)}_{\rm pinch}=1.25$ MJ, $M_{\rm rad}=0.8$ mg, $M_{\rm pinch}=1$ mg, $L=2.5$ cm, $S=1$ cm^2, $T^{(0)}_{\rm pinch}=15$ keV, $\Delta t_{\rm rad}=10$ ns, $l=0.2$ cm, $Q_{\rm HXR}=82$ kJ; and $l=0.5$ cm, $Q_{\rm HXR}=31$ kJ.

It should be noted that omitting the low-Z ionization states beyond Ne-like ions substantially overestimates the radiation yield in conventional scheme (cf. Ref. 2), whereas the values of $Q_{\rm HXR}$ in the Liner–Converter scheme are much less sensitive to this approximation.

It follows that in Liner–Converter scheme about the same HXR yield can be achieved at values of the input energy which are an order of magnitude lower than in the

conventional scheme. This makes the Liner–Converter approach a sound candidate for designing a Pulsed Power Generator-based HXR source in the range of moderate input energies.

The authors are grateful to Drs. Yu. K. Kochubey and P. D. Gasparyan for making it possible to use their numerical code SS-9.

[a)]e-mail: rudakov@rec.msk.su

[1] J. P. Quintenz, R. G. Adams, J. E. Bailey *et al.*, in *Proc. 11-th Int. Conf. High Power Particle Beams (''Beams-96''), Prague: Czech Rep. Acad. Sci.* **1**, 1 (1996).
[2] J. Davis, J. L. Giuliani, Jr., J. Rogerson, and J. W. Thornhill, *ibid.* **2**, 709 (1996).
[3] L. I. Rudakov, Yu. G. Kalinin, V. D. Korolev, and M. A. Kumakhov, Phys. Fluids B **3**, 2414 (1991).
[4] D. E. Post, R. V. Jensen, C. B. Tarter *et al.*, At. Data Nucl. Data Tables **20**, No. 5 (1977).
[5] B. A. Voinov, P. D. Gasparyan, Yu. K. Kochubey, and V. I. Roslov, Voprosy Atomnoi Nauki i Tehniki, Ser. Methods and Codes for Mathematical Physics Problems (in Russian) **2**, 39 (1993).
[6] G. S. Volkov, V. P. Smirnov, A. N. Starostin *et al.* Zh. Éksp. Teor. Fiz. **101**, 479 (1992) [Sov. Phys. JETP **74**, 253 (1992)].

Published in English in the original Russian Journal. Edited by Steve Torstveit.

Characteristic features of the phosphorescence of the complex ''naphthalene-d8–β-cyclodextrin'' at 77 K

V. B. Nazarov,[a)] V. I. Gerko, and M. V. Alfimov
Institute of Chemical Physics, Russian Academy of Sciences, 142432 Chernogolovka, Moscow District, Russia

(Submitted 14 January 1997; resubmitted 6 March 1997)
Pis'ma Zh. Éksp. Teor. Fiz. **65**, No. 7, 507–510 (10 April 1997)

It is found that the phosphorescence of naphthalene-d8 in an inclusion complex in crystalline β-cyclodextrin at 77 K differs substantially from that of frozen homogeneous solutions: The vibrational structure of the spectrum is better-resolved, the Stokes shift in the spectrum is smaller, and the lifetime is longer than the values known previously. Similar effects are observed for naphthalene-h8 and phenanthrene. © *1997 American Institute of Physics.* [S0021-3640(97)00307-1]

PACS numbers: 33.50.Dq, 33.20.Tp

Intense fluorescence and phosphorescence of glassy solutions of aromatic molecules (AMs) are observed under photoexcitation. The luminescence spectra consist of wide bands with a weakly resolved vibrational structure.[1–5]

The low resolution of the structure of the absorption and luminescence spectra of aromatic hydrocarbons in glassy matrices is due to inhomogeneous broadening which arises because the random arrangement of the aromatic molecules relative to the solvent molecules in glassy matrices makes for a wide energy distribution of the local fields produced by the environment of the aromatic molecules. The use of a molecularly organized system could give a more uniform environment around the AMs and a correspondingly narrower distribution over local fields than in homogeneous solutions. This letter examines an organized system in the form of inclusion complexes of AMs in β-cyclodextrin with a subsequent organization of the cyclodextrin into a microcrystal.

Cyclodextrins (CD) are cyclic formations which have the form of a truncated hollow cone and consist of glucose units connected with one another by oxygen bridges: α-, β-, and γ-CD contain 6, 7, and 8 glucose units, respectively, with cavity diameters of 5.7, 7.8, and 9.5 Å. The presence of a hydrophobic cavity and a hydrophilic outer surface enables CD to form stable inclusion complexes with nonpolar molecules in an aqueous medium.[6] Aromatic molecules in a CD cavity acquire, as a result of specific actions, new properties, including room-temperature phosphorescence.[7–9] However, in such complexes long-lived phosphorescence, whose spectra and lifetimes are close to those observed in frozen homogeneous solutions at 77 K,[10] exists only in the case when the cyclodextrin is organized in the form of microcrystals.

Our objective in the present work was to compare the phosphorescence spectra and lifetimes of octadeuteronaphthalene in homogeneous frozen solutions and in molecularly organized systems at the same temperature 77 K. Diethyl ether, cyclohexane, and hexane

were used for the homogeneous solutions. The molecularly organized systems consisted of the following: a) an aqueous solution of the complex ''naphthalene-d8–β-CD;'' b) an inclusion complex of naphthalene-d8 in a crystal hydrate of β-CD in water; and, c) an aqueous suspension of microcrystals prepared by adding cyclohexane (precipitant) to an aqueous solution of the complex naphthalene-d8–β-CD.

The phosphorescence spectra were recorded on a Élyumin-2M spectrofluorimeter with a of 1.5 nm spectral width of the slits in front of the observation monochromator and were left uncorrected, since the samples exhibited substantial light scattering and the measurements were comparative. At the indicated slit width a small broadening of the lines in the phosphorescence spectrum occurs, but it is the same for all samples, making it possible to compare the spectra. Narrower slits substantially decreased the signal and prevented making a comparison of the spectra because of strong noise.

The procedure for preparing samples for the measurements of the phosphorescence decay time and spectra is described in Ref. 11. To obtain fine-grained polycrystalline samples containing ''aromatic molecule–β-CD–precipitant''aggregates, cyclohexane (CH) was used as the precipitant. According to recent investigations,[11,12] cyclohexane can form microcrystals with the highest yield of long-lived phosphorescence at room temperature. This property of the CH molecules is probably due to their capability of effectively forming mixed ''β-CD–precipitant'' microcrystals with close packing of the aromatic molecules within the β-CD planes, which provides effective protection from quenching of the phosphorescence of the aromatic molecules by oxygen molecules dissolved in the water. The exact structure of these formations has not yet been established. The crystal hydrates, ranging in size up to 0.5 mm, were obtained from a CD-supersaturated aqueous solution of the complex ''naphthalene-d8–β-CD'' heated to 90 °C and cooled slowly to room temperature.

Except for diethyl ether, the solvents employed became polycrystalline on freezing.

The phosphorescence spectra of octadeuteronaphthalene at 77 K in different matrices are displayed in Fig. 1. For visual clarity, the spectra are shifted with respect to one another along the vertical axis.

For all samples containing an inclusion complex of naphthalene in β-CD (curves *1, 4, 5*), as compared with samples of the solutions of naphthalene-d8 in organic solvents (curves *2, 3, 6*), the following features of the phosphorescence spectra are observed:

1) The spectra are shifted in the short-wavelength direction ($\Delta\nu \approx 100$ cm^{-1}), possibly because of lower Stokes losses in the molecularly organized system;

2) the peak near 20000 cm^{-1} is resolved (curves *1* and *5*);

3) the narrowest electronic–vibrational lines are observed in the spectra of microcrystals containing naphthalene-d8–β-CD–CH aggregates (curve *1*), while when CH (curve *3*) or frozen aqueous solutions of CD (curve *4*) are used separately as the matrices, the structural resolution of the observed spectra is weaker;

4) the spectra in the crystal hydrate (curve *5*) and in the frozen acqueous solution of β-CD (curve *4*) are virtually identical, but the signal/noise ratio is much lower in the latter case, since naphthalene-d8 in a β-CD cavity is less isolated from contact with water

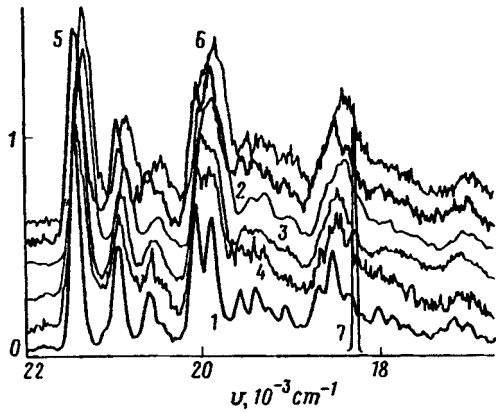

FIG. 1. Uncorrected phosphorescence spectra of naphthalene-d8 ($C=1\cdot10^{-4}$ M) at 77 K in *1*) microcrystals containing β-CD ($C=5\cdot10^{-3}$ M) and CH ($C=9\cdot10^{-2}$ M) in water, *2*) ether, *3*) cyclohexane, *4*) β-CD ($C=5\cdot10^{-3}$ M) in water, *5*) β-CD crystal hydrates ($C=0.18$ M) in water, and *6*) hexane. The units along the ordinate are arbitrary. Excitation with light from a xenon lamp at $\lambda=295$ nm with a spectral width of the monochromator slits equal to 18 nm. Curve *7* shows the instrument function of the apparatus at $\lambda=546$ nm with a spectral width of the slits for observation equal to 1.5 nm.

molecules, and, according to our observations, there is no phosphorescence in a frozen aqueous solution of naphthalene-d8.

The phosphorescence lifetimes τ of the experimental molecules, measured in the same matrices at 77 K, are given in Table I. The lifetime was determined by averaging at least 10 measurements, and since the sample preparation and the measurements were performed under identical conditions, the relative measurement error was quite low.

Comparison of the data in Table I shows that the longest phosphorescence lifetime at 77 K is obtained in microcrystals containing aggregated complexes ''naphthalene-d8–β-CD + CH'' in H_2O. Similar behavioral regularities were observed for naphthalene-h8 and phenanthrene.

In summary, the 77 K phosphorescence spectra and decay times for samples containing naphthalene-d8, which forms an inclusion complex of the ''guest–host'' type (later organized into microcrystals of CH) in the cavity of β-CD, or for a supersaturated solution differ appreciably from those of samples with homogeneous solutions. The samples obtained in this manner possess two levels of organization: inclusion complex and microcrystal. In this case, on account of a decrease in the inhomogeneous line

TABLE I. Lifetimes of the phosphorescence of naphthalene-d8 at 77 K in different matrices.

Matrix	Ether	β-CD + H_2O	CH	β-CD+H_2O+CH	Hexane
τ, s	21.7±0.3	18.1±0.4	20.1±0.3	25.1±0.5	17.2±0.3

Concentrations: naphthalene-d8 — $1\cdot10^{-4}$ M, β-CD — $5\cdot10^{-3}$ M, CH in aggregated complex — $9\cdot10^{-2}$ M, β-CD in crystal hydrates — 0.18 M.

broadening, a higher resolution of the structure of the phosphorescence spectra is obtained than in the case of the homogeneous solutions.

It remains to determine the structure of a complex in the case of such an organization of the medium and to identify the interactions of an aromatic molecule with the environment in the complex that are responsible for the observed effects.

This work was supported by the Russian Fund for Fundamental Research (Project No. 94-03-09961a).

[a)]e-mail: nazarov@icp.ac.ru

---

[1] J. Czekalla, G. Brieger, W. Herre, and H. J. Vahlensieck, Z. Elektrochem. **63**, 715 (1959).
[2] J. Czekalla and K. J. Mager, Z. Elektrochem. **66**, 65 (1962).
[3] I. Zimmermann and H. W. Zimmermann, Berichte der Bunsen-Gesellschaft **80**, 991 (1976).
[4] K. Gustav and M. Storch, Monatsh. Chem. **117**, 1007 (1986).
[5] A. P. Marchetti and D. R. Kearns, J. Am. Chem. Soc. **89**, 768 (1967).
[6] J. Szejtli, *Cyclodextrins and Their Inclusion Complexes*, Akademiai Klado-Budapest, 1982.
[7] M. D. Richmond and R. J. Hurtubise, Anal. Chim. Acta **255**, 335 (1991).
[8] A. M. Alak and T. Vo-Dinh, Anal. Chem. (Germany) **60**, 596 (1988).
[9] F. J. DeLuccia and L. J. Cline Love, Anal. Chem. **56**, 2811 (1984).
[10] M. D. Richmond and R. J. Hurtubise, Anal. Chem. **61**, 2646 (1989).
[11] V. B. Nazarov, V. I. Gerko, and M. V. Alfimov, Izv. Akad. Nauk Ser. Khim., No. 9, 2225 (1996).
[12] W. Jin, Y. Wei, A. Xu *et al.*, Spectrochim. Acta A **50**, 1769 (1994).

Translated by M. E. Alferieff

New polaron effect in magnetooptic phenomena in a quantum well

L. I. Korovin and I. G. Lang
A. F. Ioffe Physicotechnical Institute, Russian Academy of Sciences, 194021 St. Petersburg, Russia

S. T. Pavlov
P. N. Lebedev Physics Institute, 1179924 Moscow, Russia

(Submitted 21 February 1997)
Pis'ma Zh. Éksp. Teor. Fiz. **65**, No. 7, 511–515 (10 April 1997)

It is predicted that resonance coupling between two discrete electron energy levels corresponding to different size-quantization quantum numbers and different Landau quantum numbers can occur in a quantum well in a quantizing magnetic field. The resonance coupling is due to the interaction of an electron with *LO* phonons and results in the formation of polaron states of a new type. It is shown that for a certain value of the magnetic field, which depends on the splitting of the electron size-quantization levels, the absorption peak and the two-phonon resonance Raman scattering peak split into two components, the separation between which is determined by the electron–phonon coupling constant. The resonance coupling between size-quantization levels with the same Landau quantum numbers is also studied. The splitting of the peaks in this case is virtually independent of the magnetic field and can be observed in much weaker fields. The experimental observation of the effect will make it possible to determine the relative position of the electronic levels and the electron–phonon coupling constant. © *1997 American Institute of Physics.* [S0021-3640(97)00407-6]

PACS numbers: 71.38.+i, 78.20.Ls

1. The energy levels of a system consisting of an electron and *LO* phonons in a strong magnetic field cross as a function of the cyclotron frequency $\Omega = |e|H/m_e c$ at the points

$$n\Omega = \omega_{LO} \tag{1}$$

where e is the electron charge, H is the magnetic field, m_e is the electron effective mass, c is the speed of light in vacuum, ω_{LO} is the *LO* phonon frequency, and n is an integer. For such values of the magnetic field a resonance coupling is possible between bands with Landau quantum numbers 0 and n, or 1 and $n+1$, and so on. The electron–phonon interaction lifts the degeneracy at the crossing point of the levels; this is seen in magnetooptic effects such as interband absorption and Raman scattering. For example, in the three-dimensional (3D) case with $n=1$ and magnetic fields corresponding to $\Omega \cong \omega_{LO}$, two interband absorption peaks are observed instead of one,[1] and the splitting between the peaks is proportional to $\alpha^{2/3}$ (Ref. 2), where α is the dimensionless Fröhlich

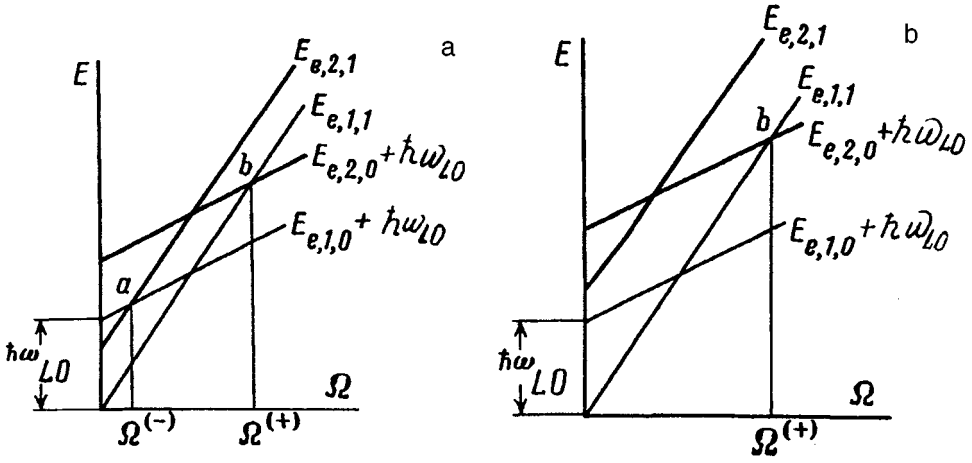

FIG. 1. a) Energy levels of an electron–phonon system as a function of the cyclotron frequency Ω. *a* and *b* — Level crossings corresponding to the condition (4). The thick lines correspond to size-quantization levels $m=2$. b) Energy levels of an electron–phonon system as a function of the cyclotron frequency Ω for the case $\omega_e(2)-\omega_e(1)>\omega_{LO}$. The thick lines correspond to size-quantization levels $m=2$.

electron–phonon coupling constant. In a quasi-two-dimensional system this effect is enhanced, and the separation between the components of the split peak is proportional to $\alpha^{1/2}$ (Refs. 3–6).

2. In a quantum well, regarded as an example of a quasi-two-dimensional system, in a magnetic field directed perpendicular to the plane of the well the electron and hole energy levels are discrete and in the effective mass approximation have the form

$$E_{e,m,n}=\hbar\omega_e(m)+(n+1/2)\hbar\Omega,$$
$$E_{e,m_v,n_v}=\hbar\omega_h(m_v)+(n_v+1/2)\hbar\Omega_h, \tag{2}$$

where $\hbar\omega_e(m)$ is the size-quantization energy corresponding to a level with size-quantization quantum number m. The indices h and v refer to a hole. In such a system of discrete levels the condition for resonance Raman scattering, whereunder the electron–phonon interaction couples electronic levels with different quantum numbers m and n, can be satisfied together with the condition (1).

For simplicity, we shall consider electronic size-quantization levels corresponding to $m=1$ and $m=2$. Satisfaction of the simplest condition for Raman resonance coupling between two levels

$$\hbar\omega_{LO}=|E_{e,2,n\pm1}-E_{e,1,n}|=\hbar|\Omega\pm[\omega_e(2)-\omega_e(1)]| \tag{3}$$

makes possible a transition of an electron from one level to another with the emission of a single *LO* phonon (the temperature is assumed to be low so that the optical phonon branches of the crystal are not excited). When the inequality $\omega_e(2)-\omega_e(1)<\omega_{LO}$ is satisfied, there are two crossings of the Raman terms of the electron–phonon system, as one can see from Fig. 1a (points *a* and *b*) for the resonance values of the cyclotron

frequency

$$\Omega^{(\mp)}=\omega_{LO}\mp[\omega_e(2)-\omega_e(1)]. \tag{4}$$

For $\Omega=\Omega^{(-)}$ two levels cross: the level $E_{e,2,1}$ and the level $E_{e,1,0}+\hbar\omega_{LO}$. This crossing occurs in fields which are much weaker than the fields required for the condition (1) to hold, provided that $n=1$. For $\Omega=\Omega^{(+)}$ the levels $E_{e,1,1}$ and $E_{e,2,0}+\hbar\omega_{LO}$ cross.

If $\omega_e(2)-\omega_e(1)>\omega_{LO}$, then only the crossing corresponding to the minus sign in Eq. (3) (point *b* in Fig. 1b) remains. The resonance Raman coupling lifts the degeneracy of the levels (the levels repel one another).

3. If the conditions (3) hold for an electron and do not hold for a hole, then the interaction of the holes with the *LO* phonons can be neglected, since it is nonresonant. Then the light absorption coefficient $K(\omega)$ is determined by the single-particle electron Green's function[2,3]

$$K(\omega)=B\sum_{m,m_v,n}\frac{|\xi_{m_v,m}|^2}{\omega_{cv}}\,\mathrm{Re}\,\frac{i}{\omega-\omega_{cv}-\Sigma+i\delta},\quad B=\frac{e^2}{c\hbar n_0}\frac{|p^y_{cv}|^2}{m_0^2R_0^2d}, \tag{5}$$

where ω is the light frequency, n_0 is the index of refraction of the quantum-well material, m_0 is the free-electron mass, p^y_{cv} is the interband matrix element of the momentum operator (for *s* polarization of the light wave propagating in the *xz* plane), d is the width of a square quantum well, $R_0^2=c\hbar/|e|H$,

$$\omega_{cv}=\omega_g+\omega_h(m_v)+\omega_e(m)+(n+1/2)(\Omega+\Omega_h), \tag{6}$$

$$\xi_{m_v,m}=\int_{-\infty}^{\infty}dz\chi_{m_v}(z)\chi_m(z), \tag{7}$$

$E_g=\hbar\omega_g$ is the band gap, $\chi_i(z)$ is the wave function describing motion in the valence band ($i=m_v$) and in the conduction band ($i=m$) in a direction perpendicular to the plane of the well. For a square quantum well with infinitely high barriers, which is considered below, $\xi_{m_v,m}=\delta_{m_v,m}$ and $\omega_{e(h)}=\pi^2\hbar m^2/2d^2m_{e(h)}$ (m_h is the hole effective mass). It is assumed that the wavelength of the light is large compared to d.

The splitting of the peak in formula (5) is determined by the mass operator Σ. If two levels of the electron–phonon system cross, then it is sufficient to take account of the simplest diagrams (two vertices connected by electron and phonon lines) in the mass operator. In the case when the condition (3) holds exactly, $K(\omega)$ can be expressed by the formula

$$K(\omega)=\frac{\pi B}{2\omega_{LO}\omega_{cv}}[\delta(\Gamma-\sqrt{\eta F})+\delta(\Gamma+\sqrt{\eta F})], \tag{8}$$

$$\Gamma=\frac{\omega-\omega_{cv}}{\omega_{LO}},\quad \eta=\frac{\alpha}{2}\sqrt{\frac{\Omega}{\omega_{LO}}},$$

where $\delta(x)$ is the Dirac delta function and F is a numerical factor. In the case of a transition to the point *a* in Fig. 1a one has $m_v=m=2$ and $n=1$ in expression (6) for ω_{cv}. For a transition to the point *b* one has $m_v=m=1$ and $n=1$.

Repulsion of the levels of the electron–phonon system under the conditions (3) should also appear in two-phonon resonance Raman scattering (RRS). The frequency dependence of the differential scattering cross section under resonance conditions in the case of direct production of an electron–hole pair (input resonance) is determined by the expression

$$\frac{d\sigma_2}{d\o d\omega_s} \sim \frac{\eta^2}{(\Gamma-\sqrt{\eta F})^2(\Gamma+\sqrt{\eta F})^2}\Gamma^2\delta(\omega-\omega_s-2\omega_{LO}), \tag{9}$$

where ω_s is the frequency of the scattered light. The distance Δ between the peaks in Eqs. (8) and (9) equals

$$\Delta = 2\eta^{1/2}\sqrt{F}\hbar\omega_{LO}. \tag{10}$$

The coefficient F depends on the quantum numbers m and n characterizing the optical transition and the transition involving the emission of an *LO* phonon, and on the parameter $\beta=\sqrt{2}d/R_0$. Strictly speaking, the coefficient F must be calculated using the interaction of electrons and holes with ''trapped'' *LO* phonons.[7,8] To obtain an estimate, the Fröhlich interaction is used below. If $\alpha=0.06$, $\hbar\omega_{LO}=0.036$ eV, and $m_e=0.06m_0$, then for $d=250$ Å one gets $\Delta_a=2.6\times10^{-3}$ eV ($F=0.120$, $H=2.53$ T) at the point *a* and $\Delta_b=5.2\times10^{-3}$ eV ($F=0.129$, $H=33.9$ T) at the point *b*.

4. Together with the splitting of the absorption and two-phonon RRS peaks discussed above, another type of splitting is also possible for a definite width of the quantum well if

$$\omega_e(2)-\omega_e(1)=\omega_{LO}. \tag{11}$$

As one can see from Fig. 1, in this case the levels $E_{e,2,1}$ and $E_{e,1,1}+\hbar\omega_{LO}$ and also the levels $E_{e,2,0}$ and $E_{e,1,0}+\hbar\omega_{LO}$ coincide for any value of the magnetic field. The Fröhlich interaction splits the levels for any magnetic fields strong enough to form Landau levels. For the resonance (11) the splitting Δ between the peaks is determined by expression (10), and the frequency dependence of the absorption coefficient and the scattering cross section for two-phonon RRS are determined by Eqs. (8) and (9), respectively. For the levels $E_{e,2,0}$ and $E_{e,1,0}+\hbar\omega_{LO}$ we have $m_v=m=2$ and $n=0$ in Eq. (6) for ω_{cv}; for the other pair of levels $m_v=m=2$ and $n=1$. The two types of splitting differ by the magnetic-field dependence of the intensity of the split components. If the condition (3) does not hold and the magnetic field is somewhat different from the resonance field, then we obtain instead of Eqs. (8) and (9)

$$K(\omega)=\frac{\pi B}{2\omega_{LO}\omega_{cv}Q}[(Q+\lambda/2)\delta(\Gamma-\Gamma^{(+)})+(Q-\lambda/2)\delta(\Gamma-\Gamma^{(-)})], \tag{12}$$

$$\frac{d\sigma_2}{d\o\,9d\omega_s} \sim \frac{\eta^2}{(\Gamma-\Gamma^{(+)})^2(\Gamma-\Gamma^{(-)})^2}(\Gamma+\lambda)^2\delta(\omega-\omega_s-2\omega_{LO}), \tag{13}$$

$$Q=\sqrt{\frac{\lambda^2}{4}+\eta F};\quad \Gamma^{\pm}=-\frac{\lambda}{2}\pm Q;\quad \lambda=\frac{|\omega_e(2)-\omega_e(1)|+\Omega-\omega_{LO}}{\omega_{LO}}. \tag{14}$$

One can see from these formulas that a deviation from the exact Raman resonance condition (3) results in a change in the relative intensity of the peaks: The right-hand peak predominates for $\lambda > 0$ and the left-hand peak predominates for $\lambda < 0$. However, if the condition (11) holds, then for any magnetic field the intensities of the split peaks are equal and are determined by Eqs. (8) and (9). In the quantum-well model employed here the condition (11) holds for $d = 232$ Å ($\hbar\omega_{LO} = 0.036$ eV). The splittings Δ between the peaks for the levels $E_{e,2,0}$ and $E_{e,1,0} + \hbar\omega_{LO}$ for the above-chosen values of α, m_e, and $\hbar\omega_{LO}$ and $d = 232$ Å equal 2×10^{-3} eV ($H = 1$ T), 3.8×10^{-3} eV ($H = 5$ T), and 4.8×10^{-3} eV ($H = 10$ T). For the levels $E_{e,2,1}$ and $E_{e,1,1} + \hbar\omega_{LO}$ we get $\Delta = 1.8 \times 10^{-3}$ eV ($H = 1$ T), $\Delta = 3.2 \times 10^{-3}$ eV ($H = 5$ T), and $\Delta = 4 \times 10^{-3}$ eV ($H = 10$ T).

In closing, we call attention to Ref. 9, where a theory of one-phonon scattering of light in a square quantum well is developed and it is shown that, in the linear approximation in the electron–phonon interaction, a sharp intensification of scattering occurs if the condition (11) is satisfied. When the resonance coupling between the size-quantization levels is taken into account in a consistent way, a splitting of the scattering peak into two components should also occur in addition to an intensification of the scattering.

This work was supported in part by the Russian Fund for Fundamental Research (No. 96-02-17115-a, 95-02-04184-a) and the ''Physics of Solid-State Nanostructures'' Program (No. 1-009) of the MNTK.

[1] E. J. Johnson and D. M. Larsen, Phys. Rev. Lett. **16**, 655 (1966).
[2] L. I. Korovin and S. T. Pavlov, Zh. Eksp. Teor. Fiz. **53**, 1708 (1967) [Sov. Phys. JETP **26**, 979 (1967)]; JETP Lett. **6**, 50 (1967).
[3] L. I. Korovin, S. T. Pavlov, and B. É. Éshpulatov, Fiz. Tverd. Tela (Leningrad) **20**, 3594 (1978) [Sov. Phys. Solid State **20**, 2077 (1978)].
[4] Das Sarma and O. Madhukar, Phys. Rev. B **22**, 2823 (1980).
[5] A. O. Govorov, Solid State Commun. **92**, 977 (1994).
[6] F. M. Peeters and J. T. Devreese, Phys. Rev. B **31**, 3689 (1985).
[7] C. Trallero-Giner and F. Comas, Phys. Rev. B **37**, 4583 (1988).
[8] N. Mori and T. Ando, Phys. Rev. B **40**, 6175 (1989).
[9] A. Cros, A. Cantarero, C. Trallero-Giner, and M. Cardona, Phys. Rev. B **46**, 12627 (1992).

Translated by M. E. Alferieff

Anisotropy of low-temperature field evaporation of metals

I. M. Mikhaĭlovskiĭ, V. A. Ksenofontov, and T. I. Mazilova
Kharkov Physicotechnical Institute National Science Center, 310108 Kharkov, Ukraine

(Submitted 21 February 1997)
Pis'ma Zh. Éksp. Teor. Fiz. **65**, No. 7, 516–520 (10 April 1997)

A metal-surface microtopography formed by low-temperature field evaporation is analyzed by the methods of field-ion microscopy and computer modeling. It is shown that the anisotropy of the field evaporation and the regional distribution of the brightness of the ion-microscope image correspond to the configuration of the first Brillouin zones. © *1997 American Institute of Physics.*
[S0021-3640(97)00507-0]

PACS numbers: 79.70.+q, 61.16.Fk

The phenomenon of field evaporation is the underlying basis of the field-ion microscope, the atomic probe, and some types of efficient ion sources.[1,2] Despite the progress made in understanding this phenomenon, quantitative results can be obtained only in a few cases. Specifically, the anisotropy of the evaporation, which is responsible for the formation of the specific faceting of a surface during low-temperature application of high electric fields, remains in question. This makes it much more difficult to interpret ion-microscope images of metal surfaces.[3,4] Thus far, the interpretation of ion-microscope images of a solid surface is still based on geometric models supplemented with computer calculations. This letter reports the results of investigations of field evaporation anisotropy. It is shown that the microtopography of the surface formed by field evaporation in metals with bcc and fcc lattices corresponds to the configuration of the first Brillouin zones.

The anisotropy of low-temperature field evaporation of metals with bcc (tungsten) and fcc (iridium) lattices was studied. The investigations were performed in a two-chamber field-ion microscope with the samples cooled to temperatures in the range 21–78 K. The residual-gas pressure in the working chamber of the microscope was equal to $10^{-7}-10^{-6}$ Pa and the imaging gas (helium) pressure was equal to 10^{-3} Pa. After placement in the microscope, needle-shaped samples with a radius of curvature of 10–50 nm were subjected to field evaporation until an atomically smooth tip was formed.

Field evaporation anisotropy is manifested in a nonhemispherical shape of the tip of a sample after evaporation and in the presence of regular variations of the local field intensity and of the regional brightness of the ion-microscope image. The variations of the local field intensity were determined according to the displacement of the contour of constant field intensity upon a change in the working voltage. Threshold intensities of the low-temperature evaporation and field ionization of the imaging gas were used as reference field intensities.[1]

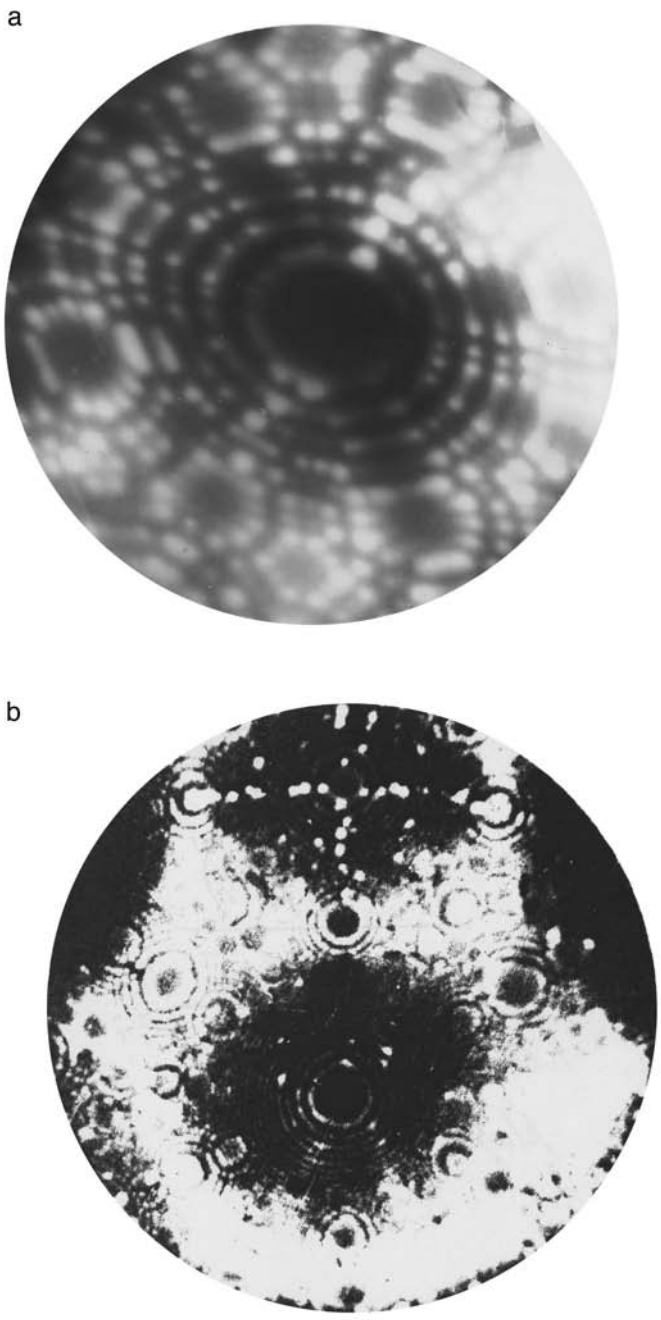

FIG. 1. Field-ion microscope images of tungsten (a) and iridium (b) surfaces. The images were formed by low-temperature field evaporation.

The ion-microscope images were modeled assuming that atoms whose centers are located inside a thin surface layer participate in image formation. The relative brightness of the imaged atoms was associated to the diameter of the corresponding spot in the model images.[3] It was assumed that for the voltage of the best image the brightness is proportional to the local field intensity.

Ion-microscope images formed of the surfaces of the tungsten and iridium single crystals by low-temperature field evaporation are displayed in Fig. 1. The intensity of the field ionization is distributed nonuniformly over the surface. The brightness of the image is higher on sections with higher local surface curvature and therefore higher field intensity. The maximum brightness in the images of tungsten (Fig. 1a) and other metals with a bcc lattice is observed on sections with a high curvature near the poles $\langle 111\rangle$ and the minimum brightness is observed on flattened sections near the poles $\langle 110\rangle$. The surface curvature is maximum on the sections between the poles $\langle 111\rangle$ and $\langle 100\rangle$. In the process of low-temperature field evaporation of iridium (fcc lattice), flattened areas form near the {100} and {111} faces (Fig. 1b). The lines with maximum intensity of the evaporation field pass through the poles $\langle 113\rangle$, $\langle 012\rangle$, and $\langle 110\rangle$.

Different modifications of the models developed by Müller[1] and Gomer and Swanson[5] are used to describe the evaporation process in strong electric fields. The first model treats field evaporation as a removal of a metal ion through a field-lowered barrier due to the image forces and the second model treats the process as a transition from an atomic state into an ionic state at the critical charge-exchange distance. The behavior of the evaporated ions in vacuum near an electronic surface is described satisfactorily in these models. In Ref. 6 it is shown that field evaporation is controlled by two potential barriers, one barrier lying in the surface layer of the metal (beneath the effective electronic surface) and the second barrier (the Schottky barrier) lying outside the surface region. At low temperatures the inner barrier is overcome as a result of a displacement of the atoms from their positions of equilibrium, equal approximately to the screening length of the electric field.

Analysis of the results of theoretical investigations of the binding forces which are characteristic for adhesion and adsorption[7] and field evaporation processes[8,9] has shown that there exists a universal interaction potential which describes these phenomena. The Thomas–Fermi screening length λ is used in the potential as the unit of length. In these processes disintegration under the action of external forces occurs when the atoms are displaced by $\lambda\xi$ from their position of equilibrium, where ξ is a coefficient of order 1; this agrees satisfactorily with the results of Ref. 6. The use of the universal potential in the theory of field evaporation has also made it possible to describe quantitatively the thermal-field characteristics of this phenomenon.[8]

In accordance with the model proposed in Ref. 9, low-temperature (nonactivational) field evaporation is preceded by a displacement of the parallel surfaces of the atomic layers from the position of equilibrium a_m, corresponding to vanishing of the second derivative of the energy E with respect to the coordinate a normal to the surface. To describe the configuration of the inner barrier controlling the field evaporation, we shall employ a semiempirical universal potential in the form[10]

$$E_0(a) = \Delta E_0 E^*(a^*), \tag{1}$$

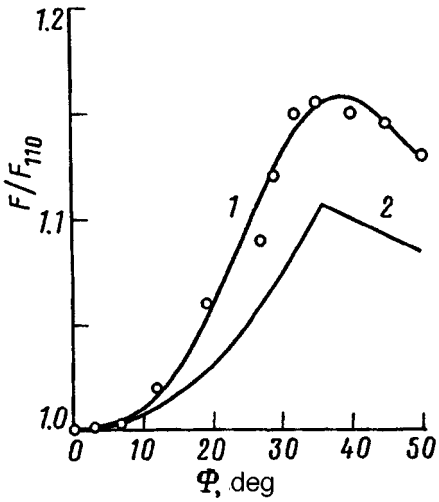

FIG. 2. Orientational dependence of the intensity of nonactivational field evaporation of tungsten near the pole [110].

where

$$E^*(a^*) = -(1+\beta_a^*)\exp(-\beta_a^*), \tag{2}$$

$a^* = (a - a_m)/\lambda$ and β is a dimensionless coefficient approximately equal to one.

The density σ of the ponderomotive electric-field forces giving rise to a displacement of the surface atomic layer by the amount $a - a_m$ equals

$$\sigma = \Delta E/\lambda\beta^2 a^* \exp(-\beta a^*). \tag{3}$$

The threshold field intensity at which nonactivational evaporation of an atomic monolayer occurs corresponds to the condition $d^2E/da^2 = 0$ and equals

$$F = 2(2\pi\Delta E/(e\lambda)\beta)^{1/2}. \tag{4}$$

To determine the evaporation energy ΔE of a monolayer we employ the relation[7]

$$\left.\frac{d^2E}{da^2}\right|_{a=a_m} = \frac{C_{11}}{(\mathbf{m}\cdot\mathbf{n})D}, \tag{5}$$

where C_{11} is the elastic stiffness constant in a direction **n** normal to the surface, **m** is a unit vector normal to the close-packed crystallographic plane, and D is the interplanar spacing. The scalar product $(\mathbf{m}\cdot\mathbf{n})$ determines the magnitude of the component of the ponderomotive forces that gives rise to stretching along the normal **n**.

It follows from relations (4) and (5) that the minimum threshold intensity of the evaporation field should be observed in the region where the poles of the close-packed planes, characterized by the maximum values of D, emerge at the surface. In accordance with experiment, flattened areas, observed as a decreased brightness of the ion-microscope image (Fig. 1), form on these sections during low-temperature evaporation.

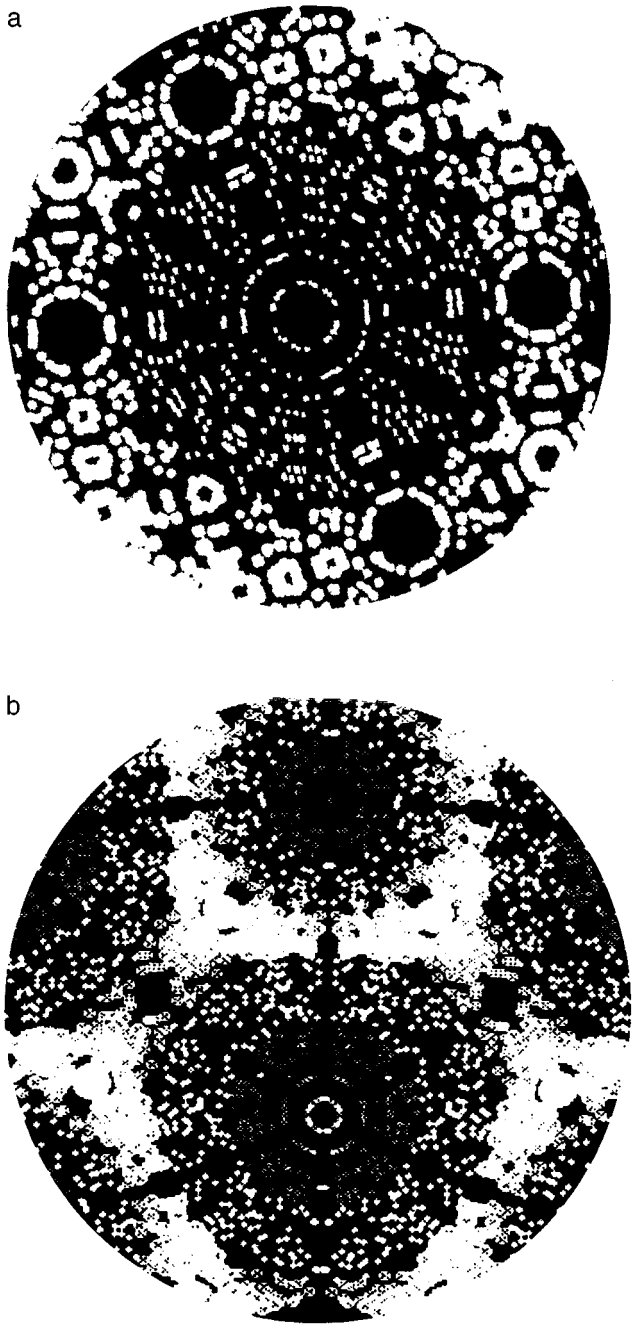

FIG. 3. Computer models of ion-microscope images formed by low-temperature field evaporation of metals with bcc (a) and fcc (b) lattices. Parameters of the model: radii of curvature 31.6 and 38.3 nm, thicknesses of the imaged shells 1.2×10^{-2} and 9.5×10^{-3} nm, crystallite orientations [110] and [131] for bcc and fcc lattices, respectively.

In the general case, when **m** and **n** are not parallel, the expression $(\mathbf{m}\cdot\mathbf{n})D=(\mathbf{G}\cdot\mathbf{n})/\mathbf{G}^2$, where **G** is a reciprocal lattice vector. From relations (1), (4), and (5) we obtain an expression for the threshold field intensity for nonactivational evaporation:

$$F=2\left[\frac{2\pi\lambda C_{11}}{\beta e}\,\frac{\mathbf{G}^2}{\mathbf{G}\cdot\mathbf{n}}\right]^{1/2}. \tag{6}$$

The experimental (1) and computed (2) curves of the ratio F/F_{110} as a function of the angle ϕ between the [110] direction and **n**, where F_{110} is the field intensity above the [110] face of tungsten, are presented in Fig. 2. Here the vectors **n** belong to the crystallographic pole $[\bar{1}10]$. In constructing the curve *2*, the vectors **G** corresponding to the minimum values of F determined from relation (6) were chosen. It follows from Fig. 2 that the analytical model describes satisfactorily the character of the low-temperature field evaporation anisotropy. The computed curves, however, give absolute values of the anisotropy factor which are too low. A more detailed correspondence can apparently be achieved by taking account of the characteristic features of the evaporation of atoms from the kinks in the surface steps.

According to relation (6), the density of the ponderomotive forces at the threshold field intensity $F^2/8\pi$ is inversely proportional to the projection of a reciprocal-lattice vector on a vector normal to the surface. Therefore, in the present model, the evaporation of a hemispherical surface of the samples proceeds by field-removal of the closest-packed surface planes with the lowest values **G**. The surface characterizing the anisotropy of the local mechanical stresses σ which arise with field evaporation is a polyhedron constructed from planes which are perpendicular to the smallest reciprocal-lattice vectors **G**. In bcc metals, such a polyhedron is a rhombic dodecahedron formed by the {110} crystallographic planes; in fcc metals the polyhedron is a truncated octahedron bounded by the {111} and {100} planes. These polyhedra are geometrically similar to the corresponding first Brillouin zones. The surface microtopography formed by field evaporation can be described such polyhedra with smoothed edges. Figure 3 displays computer models of the field-ion images of metals with bcc (a) and fcc (b) lattices; the images were constructed taking account of the anisotropy of the evaporation field intensity determined by relation (6). Comparing the computer and real ion-microscope images shows that the regional distribution of the brightness of the ion-microscope images, which reflects the low-temperature field evaporation anisotropy, corresponds to the configuration of the first Brillouin zones.

We thank V. I. Gerasimenko and V. V. Slezov for helpful discussions. This work was supported in part by the Ukrainian State Committee on Problems of Science and Technology: the Funds for Fundamental Research (Project No. 2.3/933) and the State Scientific-Technical Programs (Projects Nos. 5.42.06/040 and 7.02.05/093).

[1] E. W. Müller and T. T. Tsong, *Field-Ion Microscopy, Field Ionization, and Field Evaporation*, Pergamon Press, New York, 1973 [Russian transl. Nauka, Moscow, 1980].
[2] M. K. Miller and G. D. W. Smith, *Atom Probe Microanalysis: Principles and Applications to Materials Problems*, Oak Ridge National Laboratory, 1990 [Russian transl. Mir, Moscow, 1993].
[3] A. L. Suvorov, *The Structure and Properties of Surface Atomic Layers of Metals* [in Russian], Énergoatomizdat, 1989.

[4] V. A. Ksenofontov and I. M. Mikhailovsky, in *Abstracts of the 43rd International Field Emission Symposium*, Moscow, 1996, p. 59.
[5] R. Gomer and L. W. Swanson J. Chem. Phys. **38**, 1613 (1963).
[6] I. M. Mikhaĭlovskiĭ, Zh. I.Dranova;, V. A. Ksenofontov *et al.*, Zh. Éksp. Teor. Fiz. **76**, 1309 (1979) [Sov. Phys. JETP **49**, 664 (1979)].
[7] J. H. Rose, J. R. Smith, and J. Ferrante, Phys. Rev. B **28**, 1835 (1983).
[8] N. Shima and M. Tsukada, Surf. Sci. **194**, 312 (1988).
[9] E. R. McMullen and J. P. Perdew, Phys. Rev. B **36**, 2598 (1987).
[10] J. H. Rose, J. Ferrante, and J. Smith, Phys. Rev. Lett. **47**, 675 (1981).

Translated by M. E. Alferieff

Nonlinear percolation near a metal–insulator transition in regular textures

A. M. Satanin and S. V. Khor'kov
N. I. Lobachevskiĭ Nizhegorod State University, 603600 Nizhniĭ Novgorod, Russia

V. V. Skuzovatkin
Institute of Microstructure Physics, Russian Academy of Sciences, 603600 Nizhniĭ Novgorod, Russia

(Submitted 24 February 1997)
Pis'ma Zh. Éksp. Teor. Fiz. **65**, No. 7, 521–524 (10 April 1997)

Current percolation in weakly nonlinear two-dimensional periodic structures near a metal–insulator transition is studied. It is shown that the nonlinear conductivity exhibits critical behavior as a function of the density of the insulating and superconducting inclusions. The possibility of experimentally observing the effects predicted is discussed. [S0021-3640(97)00607-5]

PACS numbers: 71.30.+h, 74.25.Fy

Electric-field and current fluctuations are anomalously large near a metal–insulator transition. Sections where the electric field is much higher than the volume-average value are present in the system. This is why nonlinear effects are amplified in the critical region. Nonlinear effects in different objects have been actively studied experimentally in recent years.[1–3] To interpret the experiments it is important to establish a relation between the nonlinear response and the field and current correlation functions. In Refs. 2 and 4–6 it is shown that the nonlinear conductivity, the $1/f$-noise coefficient, and the amplitude of the third harmonic can be expressed in terms of the fourth moments $\langle \mathbf{e}^4 \rangle$ and $\langle \mathbf{j}^4 \rangle$ of the electric field and current, respectively. In the critical region the correlation length is greater than the sizes of the micrononuniformities. Therefore the nonlinear-response function should be a power-law function of the parameter $r=(p-p_c)/p_c$, where p is the density of the metal and p_c is the percolation threshold. However, it was noted in Refs. 3 and 5 that because the correlation functions diverge as a result of the singularities of the field the higher-order moments of the field could be sensitive to the structure of the micrononuniformities. A convenient object for studying nonlinear effects are planar structures: periodic lattices and textures. In Ref. 7 it was shown that near the percolation threshold the effective conductivity of a metal lattice with insulating and superconducting inclusions (checkerboard-type lattice), which is determined by the quartic moment $\langle \mathbf{e}^4 \rangle$ of the field, is not described by a power-law function of τ but rather behaves as $\sigma_e \sim \sigma_1 / \ln(\gamma/\tau)$. It is of interest to determine how the geometry of the micrononuniformities in periodic lattices influences the nonlinear current percolation. Specifically, it is necessary to calculate the critical exponent of the effective nonlinear conductivity and the $1/f$-noise coefficient; this will make it possible to understand why these exponents are not universal.[3]

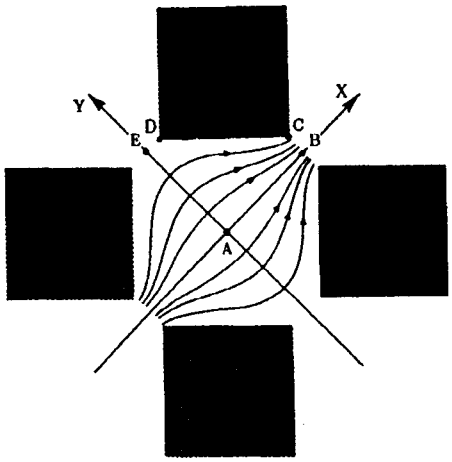

FIG. 1. Fragment of texture with insulating inclusions.

This letter studies the nonlinear current percolation in periodic lattices. Two types of lattices are studied. In the first type a metal matrix with conductivity σ_1 contains insulating inclusions with conductivity $\sigma_1 \to 0$ arranged in a checkerboard order (Fig. 1). In the second case superconducting inclusions with conductivity $\sigma_2 \to \infty$ are arranged in a checkerboard order in a metal matrix (Fig. 2). The closest distance between the corners of neighboring squares is $2d$ and the distance between the centers of the squares is $2a$. Such structures model well a metal–insulator transition above and below, respectively, the percolation threshold. In the critical region $\tau \approx 2d/a$. The threshold density $p_c = 0.5$. The nonlinear effects are taken into account by generalizing the expression for the current

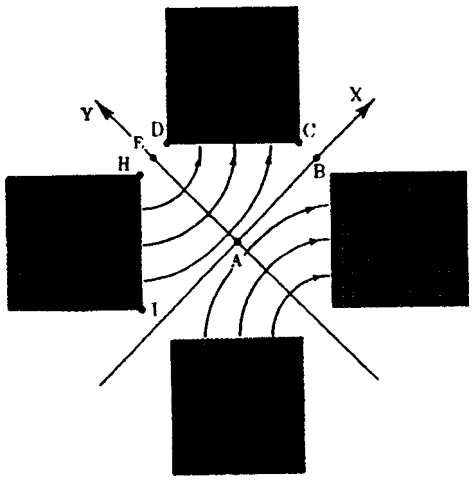

FIG. 2. Fragment of texture with superconducting inclusions.

$$\mathbf{j}=\sigma\ \mathbf{e}+\chi\mathbf{e}^2\mathbf{e} \tag{1}$$

in a normal metal. It is shown in this model that the effective nonlinear conductivity grows anomalously near the percolation threshold: $\chi_e \sim \chi_1/\tau^2 \ln^4(\tau)$ for $p>p_c$ and $\chi_e \sim \chi_1/\tau^2$ for $q<q_c$, where $q=1-p$ and $q_c=p_c$.

The effective nonlinear conductivity can be calculated according to Ref. 5

$$\chi_e=\frac{\langle \chi \mathbf{e}^4\rangle}{\langle \mathbf{e}^4\rangle}, \tag{2}$$

where $\mathbf{e}$ is the electric field in the linear medium. In this system the field distribution $e(z)$ in the linear case can be obtained exactly by the method of conformal transformations.[7] If the external field $\langle \mathbf{e}\rangle$ is directed along the X axis, then in a system containing insulating inclusions one has

$$e(z)=\frac{A}{C}\left(\frac{1-k_2^2\zeta^2(z)}{1-k_1^2\zeta^2(z)}\right)^{1/4}, \tag{3}$$

where $z=x+iy$ and the function $\zeta(z)$ is determined by the integral

$$z=C\int_0^{\zeta}\frac{dt}{\sqrt{1-t^2}(1-k_1^2t^2)^{1/4}(1-k_2^2t^2)^{1/4}}, \tag{4}$$

and k_1, k_2, and C are expressed only in terms of the geometric parameters of a cell.[7] The quantity A can be found by conformally mapping the unit cell *ABCDE* (Fig. 1) onto a rectangle with a uniform distribution of the electric field. Since such a transformation does not change the square of the field, it is easy to obtain $A=a|\langle \mathbf{e}\rangle|/K(k_1)$, where $K(k_1)$ is a complete elliptic integral of the first kind. From expression (2) with expressions (3) and (4) substituted in, we obtain an exact expression for χ_e, from which, for $\tau \ll 1$, we find that

$$\chi_e=\frac{\pi\chi_1}{2\tau^2\ln^4(\tau/\gamma)}, \tag{5}$$

where $\gamma=2\pi K^{-2}(1/\sqrt{2})$. Expression (5) can also be obtained from the following qualitative arguments. According to Eqs. (3) and (4), the electric field near some corners (for example, the corner C in Fig. 1) behaves as $|e(z)|\sim r^{-1/3}$, where r is the distance from the corner. This dependence does not result in a divergence in Eq. (2). However, it follows from Eqs. (3) and (4) for $\tau \ll 1$ that in the region $d \ll r \ll a$ the field behaves asymptotically as $|e(z)|\sim Ar^{-1}$, where r is the distance measured from the point B (Fig. 1). This behavior of the field leads to expression (5). Indeed

$$\chi_e \sim \frac{\chi_1 a^2}{\ln^4(\gamma/\tau)}\int_0^{\pi/4}\int_d^a r^{-3}dr\,d\alpha \sim \chi_1\frac{1}{\tau^2\ln^4(\gamma/\tau)}. \tag{6}$$

The derivation of expression (6) employed the fact that $A=a|\langle \mathbf{e}\rangle|/2\ln(\gamma/\tau)$ for $\tau \ll 1$. For the case of superconducting inclusions the electric field is found from Eq. (3) with k_1 replaced by k_2 (Ref. 7). Similar arguments yield the effective nonlinear conductivity in the critical region

$$\chi_e = \frac{128\chi_1}{\pi^3\tau^2}. \tag{7}$$

This formula can also be obtained from the following qualitative considerations. The field lines are normal to the boundaries of the superconducting inclusions. Therefore the planes *CD* and *HI* can be interpreted as the plates of an ''open capacitor'' (Fig. 2). It is well known that for $\tau \ll 1$ the electric field in the region $d \ll r \ll a$ behaves as $|e(z)| \sim |\langle \mathbf{e} \rangle| a r^{-1}$, where r is the distance measured from the point *E*. Therefore

$$\chi_e \sim \chi_1 a^2 \int_0^{\pi/4} \int_d^a d^{-3} dr d\alpha \sim \chi_1 \frac{1}{\tau^2}. \tag{8}$$

According to Ref. 7, the effective linear conductivity near the percolation threshold behaves as

$$\sigma_e/\sigma_1 = (\pi/4)\ln^{-1}(\gamma/\tau), \quad p > p_c;$$

$$\sigma_e/\sigma_1 = (4/\pi)\ln(\gamma/\tau), \quad q < q_c.$$

Therefore the critical exponents for the divergence of the relative density of $1/f$ noise, which, according to Refs. 3 and 5, are determined from the relations

$$\chi_e/\sigma_e^2 \sim \tau^{-k'}, \quad p > p_c;$$

$$\chi_e/\sigma_e^2 \sim \tau^{-k}, \quad q < q_c,$$

in our case are equal: $k' = k = 2$.

In conclusion, we note once again that the divergence of the effective nonlinear conductivity χ_e arises in the limit $\tau \to 0$ not because of a singularity of the field near the corners but rather because a neck of size $\sim a$, narrowing to a size of the order of d, appears as a result of the corners. In the case of insulating inclusions, the bunching of the current lines toward the neck toward a sink near the point *B* (Fig. 1) leads to the asymptotic behavior $|e(z)| \sim |\langle \mathbf{e} \rangle| a/r \ln(\gamma/\tau)$. In the case of superconducting inclusions an ''open capacitor'' whose plates are superconducting arises. The electric field in such a system behaves as $|e(z)| \sim |\langle \mathbf{e} \rangle| a r^{-1}$. It should be noted that in the structures investigated in Ref. 3 necks of this type do not make the main contribution to the higher-order moments of the electric field. This is why the critical exponents in Ref. 3 differ sharply from the checkerboard packing.

In the system studied in the present letter the critical field for nonlinearity,[1] E_c, will decrease as $E_c \sim \tau$ near the percolation threshold, i.e., nonlinear effects are anomalously large in the critical region.

The predicted effects can be checked in experiments with planar structures or in a model experiment with square openings in a foil. The anomalous growth of the effective nonlinearity can be most simply observed according to the growth of the amplitude of the third harmonic of the current.[3,8]

[1] Y. Gefen, W. H. Shin, R. B. Laibowitz, and J. M. Viggiano, Phys. Rev. Lett. **57**, 3097 (1986).
[2] R. K. Chakrabarty, K. Bardhan, and A. Basu, Phys. Rev. B **44**, 6773 (1991).
[3] M. A. Dubson, Y. C. Hui, M. B. Weissman, and J. C. Garland, Phys. Rev. B **39**, 6807 (1989).

[4] A. Aharony, Phys. Rev. Lett. **58**, 2726 (1987).
[5] D. Stroud and P. M. Hui, Phys. Rev. B **37**, 8719 (1988).
[6] D. J. Bergman, Phys. Rev. B **39**, 4598 (1989).
[7] B. Ya Balagurov, Zh. Eksp. Teor. Fiz. **79**, 1560 (1980) [Sov. Phys. JETP **52**, 787 (1980)].
[8] A. A. Snarskiĭ, Pis'ma Zh. Tekh. Fiz. **21**(1), 3 (1995) [Tech. Phys. Lett. **21**, 1 (1995)].

Translated by M. E. Alferieff

Birefringence and absorption of light during intersubband transitions of hot electrons in quantum wells

L. E. Vorob'ev, D. A. Firsov, and V. A. Shalygin
St. Petersburg State Technical University, 195251 St. Petersburg, Russia

I. I. Saĭdashev
A. F. Ioffe Physicotechnical Institute, Russian Academy of Sciences, 194021 St. Petersburg, Russia

(Submitted 25 February 1997)
Pis'ma Zh. Éksp. Teor. Fiz. **65**, No. 7, 525–530 (10 April 1997)

The changes in the birefringence and absorption of infrared radiation accompanying direct electron transitions induced between size-quantization subbands in a GaAs/AlGaAs system of doped quantum wells by heating of the electrons by an electric field applied parallel to the layers of the heterostructure are observed and investigated. An explanation of the observed effects is offered whereing the change in the absorption spectrum and the contribution of free electrons to the permittivity are related to the exchange interaction and nonparabolicity of the energy spectrum of the hot electrons. © *1997 American Institute of Physics.* [S0021-3640(97)00707-X]

PACS numbers: 78.66.Fd, 78.20.Fm

Intersubband optical transitions of electrons in quantum wells have been under intense study in recent years.[1] The physics of intersubband transitions is of interest in connection with the development of quantum-well-based detectors and fast modulators for infrared radiation[1] as well as quantum cascade lasers.[2] It is also possible to produce new types of optoelectronic devices based on hot charge carriers in quantum wells. At the same time, as far as we know, the optical phenomena accompanying intersubband transitions of hot electrons in a longitudinal electric field (parallel to the size-quantized layers) have not been investigated.

In the present work we observed and investigated the changes in the birefringence and absorption of light which are associated with intersubband optical transitions of electrons heated by a longitudinal electric field in a system of doped quantum wells. This letter proposes an explanation for the observed optical phenomena. Size-quantized GaAs/AlGaAs layers were investigated but the observed optical phenomena are of a general character for *n*-type quantum wells.

The experimental investigations were performed on a structure consisting of 50 periods of doped (donor density $N_D = 6 \cdot 10^{17}$ cm^{-3}) GaAs quantum wells 10.2 nm wide separated by undoped $Al_{0.33}Ga_{0.67}As$ barriers 25.4 nm wide. The surface electron density was equal to $6.1 \cdot 10^{11}$ cm^{-2}. Optical radiation was introduced into the sample through the side faces of the substrate (GaAs), which were beveled at an angle of 45° with respect to the optical axis of the structure (the optical axis is also the direction of growth of the

structure). The incident radiation was linearly polarized with the polarization vector oriented at an angle of 45° with respect to the optical axis. Two linearly polarized waves were excited simultaneously in the sample: an ordinary wave (*s* polarization, the electric field vector of the wave lies in the plane of the layers) and an extraordinary wave (*p* polarization, the electric field vector possesses a component along the growth axis of the structure).

The *p*-polarized wave possesses a strong absorption peak in the region of direct intersubband transitions; for *s* polarization only absorption due to indirect intrasubband electron transitions is appreciable in this spectral region. On account of the Kramers–Kronig relations, the difference in the absorption spectra of the waves with these polarizations also induces a difference in the refractive indices for them: $n_p \neq n_s$. Therefore as these two waves propagate in the sample a phase shift arises between them, and as a result the radiation at the exit from the sample is elliptically polarized even under equilibrium conditions.[3] The difference $(\alpha_p - \alpha_s)$ of the absorption coefficients of the *p* and *s* waves as well as the magnitude of the birefringence $(n_p - n_s)$ can be determined by analyzing the form of the polarization ellipse.

Our objective in the present work was to investigate the changes $\Delta\alpha_p$ and $\Delta\alpha_s$ induced in the absorption by the heating of two-dimensional electrons as well as the change $\Delta|n_p - n_s|$ in the birefringence. The 2D electrons were heated by 200-ns longitudinal electric field pulses. The equilibrium temperature of the sample was equal to $T_0 = 77$ K. A tunable CO_2 laser served as a source of radiation. The electrooptic experiments were performed for three different wavelengths of the infrared radiation. A photodetector was used to record the modulation of the radiation intensity for different angular positions of the analyzer, placed between the sample and the photodetector.

When the electrons were not heated, the sample demonstrated an intense absorption line for the *p*-polarization wave near the energy $h\nu = 111$ meV. Electrooptic measurements on the short-wavelength wing of this line revealed an appreciable decrease in the absorption coefficient α_p in an electric field (Fig. 1), while no modulation of the absorption for the *s*-polarization wave was observed. Characteristically, the observed ''bleaching'' of the sample weakened rapidly as the working wavelength moved away from the top of the equilibrium absorption peak. This made it possible to conclude (to a first approximation) that the ''red'' shift of the absorption line is due to heating of the electrons. In a field $E \approx 1000$ V/cm the magnitude of the shift corresponding to the observed values of the absorption modulation equals about 2 meV.

The data on the electric-field-induced birefringence $\Delta|n_p - n_s|$, which are also displayed in Fig. 1, correspond to the same magnitude of the spectral shift (this follows from numerical calculations based on the Kramers–Kronig relations).

We note that the absorption of light with the two polarizations is also different in the presence of interband transitions of electrons in size-quantized heterolayers (for $h\nu > E_g$, E_g is the band gap for the well material): $\alpha_p \neq \alpha_s$. These transitions contribute to the birefringence in the spectral region $h\nu < E_g$ (Ref. 4). In *n*-type structures with doped wells, under conditions of interband transitions one has $\alpha_p(\nu) = \alpha_{p0}(\nu) \times [1 - f_1(E_\nu)]$ and $\alpha_s(\nu) = \alpha_{s0}(\nu)[1 - f_1(E_\nu)]$, where $\alpha_{p0}(\nu)$ and $\alpha_{s0}(\nu)$ are the absorption coefficients for undoped wells, $f_1(E_\nu)$ is the electron distribution function for

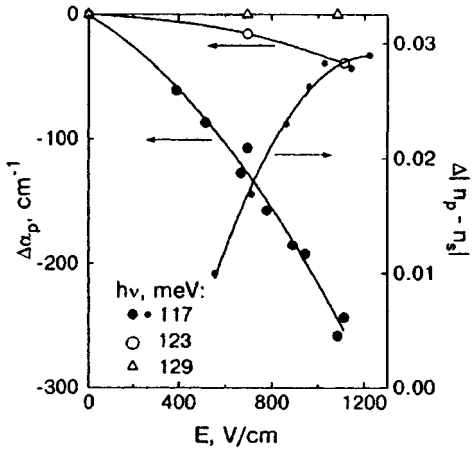

FIG. 1. Effect of a longitudinal electric field on the light absorption coefficient α_p and the magnitude of the birefringence $|n_p-n_s|$in GaAs/AlGaAs quantum wells at $T_0=77$ K.

the first size-quantization subband, and E_ν is the electron energy, corresponding to an interband transition with absorption of a photon $h\nu$, in the first subband.

When the electrons are heated, $f_1(E_\nu)$ and therefore α_p and α_s change. According to the Kramers–Kronig relation, this changes the refractive indices n_p and n_s. In other words, the interband contribution to birefringence should change as the electrons are heated. This effect is large for $h\nu \approx E_g$ and decreases rapidly with decreasing photon energy. Estimates show that for the photon energies used in our electrooptic experiments $h\nu=117, \ldots, 129$ meV the intersubband contribution to $\Delta|n_p-n_s|$ is an order of magnitude greater than the interband transition.

We note that the birefringence due to the heating and drift of electrons in an electric field and interband transitions of electrons with $h\nu \approx E_g$ was studied in Ref. 5 for the three-dimensional case.

The nature of the red shift, observed in the present work, of the absorption line is determined by the nonparabolicity and the exchange interaction. We performed a model calculation of the transformation of the intersubband absorption line accompanying heating of the electrons. We used Ekenberg's model,[6] which takes account of nonparabolicity, as the zeroth approximation for the energy spectrum of the 2D electrons. In this model the slope of the dispersion curves $E_n(\mathbf{k})$ for the ground-state $(n=1)$ and excited $(n=2)$ subbands is substantially different. This in itself already results in a spectral shift of the absorption line accompanying heating of the electrons (on account of the redistribution of the electrons over the states in $\mathbf{k}$ space).

Further calculations showed that the transformation of the intersubband absorption line accompanying heating of the electrons is affected even more by the electron–electron exchange interaction. On account of the exchange effects, the redistribution of heated electrons in $\mathbf{k}$ space is accompanied by a change in the form of the dispersion curves $E_n(\mathbf{k})$.

To calculate the exchange corrections to the energy spectrum of 2D electrons we employed the results obtained by Bandara *et al.*,[7] extending them to the case of nonzero electron temperature and excited subbands ($n>1$):

$$\Delta E(\mathbf{k}) = -\frac{e^2}{\epsilon}\int d^3r \int d^3r' \sum_m \sum_{k'} f_m(\mathbf{k}')\frac{1}{|\mathbf{r}-\mathbf{r}'|} \times \Psi^*_{m\mathbf{k}'}(\mathbf{r}')\Psi_{n\mathbf{k}}(\mathbf{r}')\Psi_{m\mathbf{k}'}(\mathbf{r})\Psi^*_{n\mathbf{k}}(\mathbf{r}), \quad (1)$$

where $\Psi_{n\mathbf{k}}(\mathbf{r}) = (\sqrt{S})^{-1}e^{i\mathbf{k}\cdot\vec{\rho}}\phi_n(x)$ is the wave function of an electron in the nth subband, $\mathbf{r}=(\vec{\rho}, x)$, $\vec{\rho}$ is a two-dimensional vector in the plane of the layer (S is the area of the structure), x is the coordinate in an orthogonal direction, $\phi_n(x)$ is an electron wave function in a one-dimensional well, $\mathbf{k}$ is the two-dimensional wave vector of an electron, and $f_m(\mathbf{k})$ is the electron distribution function in the mth subband.

Assuming that all electrons are concentrated in the bottom subband and their energy distribution is described by a Fermi function with temperature T_e:

$$f_1(\mathbf{k}) = \frac{1}{\exp[(E_1(\mathbf{k})-E_F)/k_BT_e]+1}, \quad f_m(\mathbf{k}) = 0 \quad (m \geqslant 2), \quad (2)$$

the integral (1) can be put into the form

$$\Delta E_n(\mathbf{k}) = -2\pi\frac{e^2}{\epsilon}\int \frac{d^2k'}{(2\pi)^2} f_1(\mathbf{k}') \int dx \int dx'\, \phi_1^*(x')\phi_n(x') \times \phi_1(x)\phi_n^*(x)\frac{e^{-|\mathbf{k}-\mathbf{k}'||x-x'|}}{|\mathbf{k}-\mathbf{k}'|}. \quad (3)$$

Using this expression, we performed numerical calculations of the exchange corrections to the energy spectrum of electrons in the ground-state and excited subbands for both equilibrium ($T_e=T_0$) and hot ($T_e>T_0$) electrons. In the calculations it was assumed that the lattice temperature $T_0=77$ K. The Fermi energy E_F corresponding to the given value of T_e was found from the normalization condition for the distribution function f_1 taking account of the exchange corrections $\Delta E_1(\mathbf{k})$ (by an iteration procedure). The computational results for the structure which we investigated are presented in Fig. 2.

We note that for the center of the subbands ($\mathbf{k}\approx 0$) the exchange interaction shifts the electron states downwards on the energy scale, the shift being several times greater for the first subband than for the second subband. As the electron temperature increases, the exchange corrections for the center of the subbands decrease on account of a redistribution of the electrons from the center to the periphery of the first subband. Therefore, as the electric field heats up the electrons, not only are the electrons redistributed over the states in $\mathbf{k}$ space, but the energy of the states itself changes as well.

The spectral curve of light absorption near intersubband transitions of electrons from the ground-state subband into an excited subband was calculated for the electron energy spectrum obtained $E_n(\mathbf{k})+\Delta E_n(\mathbf{k})$:

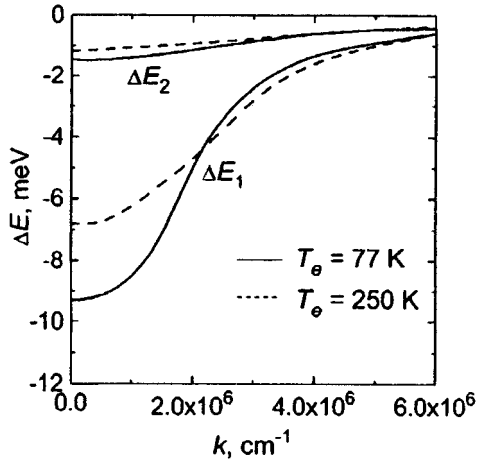

FIG. 2. Exchange corrections to the energy spectrum of equilibrium and hot 2D electrons. The calculation was performed for $T_0 = 77$ K.

$$\alpha(h\nu) \propto \frac{1}{h\nu} \int d^2k |\mathbf{M}|^2 \delta(E_2(\mathbf{k}) + \Delta E_2(\mathbf{k}) - E_1(\mathbf{k}) - \Delta E_1(\mathbf{k}) - h\nu) \times f_1(\mathbf{k})[1 - f_2(\mathbf{k})], \tag{4}$$

where the transition matrix element $\mathbf{M} \cong 0$ for a wave with s polarization and $\mathbf{M} \neq 0$ for a wave with p polarization. We underscore that in Eq. (4) f_1 and f_2 are determined by the electron temperature T_e; $\mathbf{M}$, E_1, and E_2 are determined by the lattice temperature T_0; and, ΔE_1 and ΔE_2 depend on both temperatures.

The computed intersubband absorption line shapes for the investigated structure both in equilibrium and with heated electrons are presented in Fig. 3 To facilitate comparison with experiment, the computed absorption line is additionally Lorentz-broadened (the broadening $2\Gamma_0 = 2.7$ meV is chosen in accordance with the experimental equilibrium absorption curve). The computed curves are shown on a relative scale $h\nu - h\nu_0$, where $h\nu_0$ is the equilibrium position of the intersubband absorption peak. This makes it possible to neglect the depolarization shift (which remains almost unchanged as the electrons are heated). As one can see from the figure, the model considered gives a ''red'' shift of the intersubband absorption peak and a broadening of the peak when the electrons are heated; this agrees qualitatively with the above-described experimental data on the modulation of light in a longitudinal electric field. The field-dependence of the temperature of the hot electrons can be obtained by comparing the experimentally observed decrease of the absorption coefficient for light with $h\nu = 117$ and 123 meV with the family of computed curves of intersubband absorption on hot electrons. Specifically, for $E = 1000$ V/cm we obtain that the electrons are heated up to the temperature $T_e \approx 250$ K (in this field the average power acquired by one electron is $e\mu_n E^2 = 3.7 \cdot 10^{-10}$ W, where μ_n is the electron mobility). This agrees well with the experimental data obtained in Ref. 8 for the temperature of the hot electrons in similar quantum wells by analyzing the hot photoluminescence (with the same power per electron).

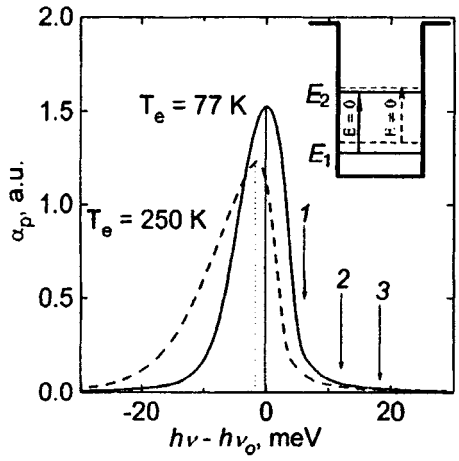

FIG. 3. Shift and broadening of the intersubband absorption line accompanying heating of 2D electrons. The calculation was performed for $T_0 = 77$ K. The arrows *1*, *2*, and *3* mark the position of the laser emission lines on which the electrooptic modulation was studied experimentally (117, 123, and 129 meV, respectively). Inset: Transitions of electrons in a quantum well under the action of light for $k = 0$.

We are grateful to A. Ya. Shik, A. G. Petrov, and A. Ya. Kazakov for a discussion of a number of questions considered in this letter. This work is supported by the Russian Fund for Fundamental Research (Grant No. 96-02-17404a), RFFI–INTAS (Grant No. 00615.i96), and the Government Committee on Science and Technology of the Russian Federation (Grant No. 1-093/4).

[1] E. Rosencher and B. Levine (eds.), *Intersubband Transitions in Quantum Wells*, NATO ASI Series, Ser. B, Physics, Vol. 288, Plenum Press, New York, 1992.
[2] J. Faist, F. Capasso, D. L. Sivco *et al.*, Science **264**, 553 (1994).
[3] D. Kaufman, A. Saar, and N. Kuze, Appl. Phys. Lett. **64**, 2543 (1994).
[4] A. Fainstein, P. Etchegion, P. V. Santos *et al.*, Phys. Rev. B **50**, 11850 (1994).
[5] L. E. Vorob'ev, V. I. Stafeev, and D. A. Firsov, Fiz. Tekh. Poluprovodn. **18**, 513, 351 (1984) [Sov. Phys. Semicond. **18**, 317 (1984)]; *ibid.*, **565**, 352 (1984)].
[6] U. Ekenberg, Phys. Rev. B **40**, 7714 (1989).
[7] K. M. S. V. Bandara, D. D. Coon, and O. Byunsung, Appl. Phys. Lett. **53**, 1931 (1988).
[8] E. Ozturn, N. C. Constantionu, A. Straw *et al.*, Semicond. Sci. Technol. **9**, 782 (1994).

Translated by M. E. Alferieff

Faraday effect in Co/TiO_2 films

Yu. A. Dynnik,[a)] I. S. Édel'man, T. P. Morozova, P. D. Kim, I. A. Turpanov, A. Ya. Beten'kova, and G. V. Bondarenko

L. V. Kirenskiĭ Institute of Physics, Siberian Branch of the Russian Academy of Sciences, 660036 Krasnoyarsk, Russia

(Submitted 25 February 1997)
Pis'ma Zh. Éksp. Teor. Fiz. **65**, No. 7, 531–534 (10 April 1997)

It is shown that in a layered medium consisting of a magnetic metal (Co) and a nonmagnetic insulator (TiO_2), the layer thickness being less than the wavelength of the light, a fundamental change occurs in the character of the Faraday-effect spectra if the number of layers is sufficiently large. When the number of pairs of layers changes from 5 to 10, a maximum appears near ~ 1.7 eV in the Faraday rotation spectrum and the ellipticity passes through zero. The results obtained are compared with the existing theory of the Faraday effect in granular structures consisting of a magnetic metal and nonmagnetic insulator. The surface plasmon energy in thin Co layers is estimated. © *1997 American Institute of Physics.* [S0021-3640(97)00807-4]

PACS numbers: 78.20.Ls, 78.66.Sq

Recently, we observed large changes in the Faraday rotation (FR) spectra in Co/TiO_2 films[1,2] as compared with the FR spectra in thick continuous Co films, we studied the dependence of the character of these changes on the thickness of the Co and SiO_2 layers, and we compared these dependences with the results of theoretical works[3–5] where the FR spectra in layered and granular media consisting of a magnetic metal and a nonmagnetic insulator were studied. The most important predictions made in Refs. 4 and 5 were that maxima should appear and the sign of the FR should be different in different sections of the spectrum. The position of the maxima was determined by the ratio of the dielectric constant ϵ_0 of the material of the nonmagnetic layers and the real part of the diagonal component ϵ_{xx} of the permittivity tensor of the magnetic layers. For the same values of the parameters of the magnetic layers, increasing ϵ_0 should cause the maxima of the FR to shift toward lower values of the energy of the light wave. In the case of Co/SiO_2 ($\epsilon_0 \cong 2.1$), only an increase in the magnitude of the FR with increasing photon energy was observed, the increase being more rapid the thicker the SiO_2 layers, in agreement with the theory of Refs. 4 and 5, and the maximum itself did not appear in the region of the spectrum studied, bounded at the short-wavelength end by the transmittance of the samples. For this reason, to make a correct comparison with the theory the insulating layers must consist of a material with large ϵ_0, for which a maximum can be expected to appear in the FR in the visible region of the spectrum. A suitable material could be rutile TiO_2, for which $\epsilon_0 \cong 5.3$. As far as we know, layered systems which include rutile have not been studied previously.

This letter reports the results of investigations of the FR and Faraday ellipticity (FE)

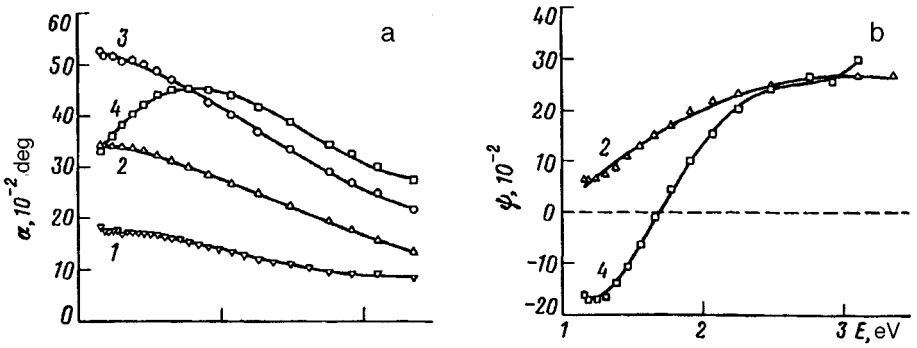

FIG. 1. a — FR spectra for the following: *1* — Sample No. 1, containing five Co layers, *2* — sample No. 2, containing five Co layers, *3* — algebraic sum of the curves for samples Nos. 1 and 2, *4* — sample No. 3, containing ten Co layers. b — FE spectra for the following: *1* — Sample No. 2, *4* — sample No. 3. The experiments were done at room temperature, with a magnetic field of 5 kOe oriented in a direction normal to the plane of the samples.

spectra in Co/TiO_2 multilayer films and their dependence on the number of layers.

The films were prepared by magnetron sputtering in dc current (Co) and ac current (TiO_2) from different targets in an argon atmosphere. Initially, five pairs of Co and TiO_2 layers, each $\sim$3.0 nm (Co) and $\sim$6 nm (TiO_2) thick, were deposited on a glass substrate sputtered (sample No. 1). The FR and FE spectra were obtained for this sample. Next, another five pairs of Co and TiO_2 layers were deposited on the same sample. For comparison, the deposition was conducted simultaneously on a clean substrate (sample No. 2) as well. Thust the sample with 10 pairs of layers (No. 3) was a ''sum'' of the two five-layer samples (Nos. 1 and 2).

The FR and FE were measured by a null method (the FE with the aid of a quarter-wave plate) in the energy range 1.0–3.4 eV.

The FR and FE spectra are displayed in Figs. 1a and 1b, respectively. For samples Nos. 1 and 2, a monotonic decrease of the FR with increasing photon energy, similar to the trend of the FR in uniform thick Co films,[6] is observed. The FR in sample No. 2 is greater than in sample No. 1, since in the second case the Co layers were thicker. Curve *3* in Fig. 1a is an algebraic sum of the curves *1* and *2*. One can see that the FR spectrum of sample No. 3, containing ten pairs of layers, is substantially different from the sum of the spectra of two samples containing 5 pairs of layers each: A wide but distinct maximum, corresponding to the passage of the FE curve through zero (Fig. 1b, curve *4*) appears in the spectrum near 1.7 eV. Therefore a qualitative change occurs in the characteristics of the medium as the number of constituent layers increases. The picture becomes similar to that predicted by a theoretical analysis[3,5] performed in the effective permittivity tensor approximation and taking account of the effect of surface plasmons in thin metal layers on the magnetooptic spectra of the layers. Proceeding from the well-known expression for the complex Faraday effect

$$\alpha - i\psi = (\pi/\lambda)\gamma\epsilon^{-1/2}, \tag{1}$$

where α is the rotation angle, ψ is the ellipticity, $\gamma=\gamma'-i\gamma''$ and $\epsilon=\epsilon'-i\epsilon''$ are the complex off-diagonal and diagonal components of the permittivity tensor of the medium, we can write down the following relations for α and ψ:

$$\alpha=(\pi/\lambda\sqrt{2})(\gamma'\sqrt{r+\epsilon'}+\gamma''\sqrt{r-\epsilon'})/r, \tag{2}$$

$$\psi=(\pi/\lambda\sqrt{2})(\gamma'\sqrt{r-\epsilon'}-\gamma''\sqrt{r+\epsilon'})/r, \tag{3}$$

where

$$r=[(\epsilon')^2+(\epsilon'')^2]^{1/2}. \tag{4}$$

In accordance with Ref. 3, a medium consisting of alternating layers of an insulator with dielectric constant ϵ_0 and a metal magnetized in a direction normal to the plane of the layers is characterized by the effective permittivity tensor with the components

$$\gamma=f\gamma_m=f(\gamma_m'-i\gamma_m'') \tag{5}$$

and

$$\epsilon=(1-f)\epsilon_0+f\epsilon_m=(1-f)\epsilon_0+f\epsilon_m'-if\epsilon_m'', \tag{6}$$

where f is the filling factor of the metal and γ_m and ϵ_m are the components of the permittivity tensor of the metal. Since ϵ_m' is negative, taking account of Eq. (6), the sign and magnitude of ϵ' in Eqs. (2)–(4) depend on f on account of Eq. (6) and for some value of f the quantity ϵ' passes through zero and the denominator in Eqs. (2) and (3) passes through a minimum. As f varies, the numerators in expressions (2) and (3) also vary. The conditions for α and ψ to pass through zero are obvious:

$$\gamma'\sqrt{r+\epsilon'}+\gamma''\sqrt{r-\epsilon'}=0, \tag{7}$$

$$\gamma'\sqrt{r-\epsilon'}-\gamma''\sqrt{r+\epsilon'}=0. \tag{8}$$

To determine the positions of the maxima, expressions (2)–(3) must be analyzed for a maximum. However, the energy (or frequency) of the maxima approximately corresponds to ϵ' passing through zero, i.e., the condition

$$(1-f)\epsilon_0+f\epsilon_m'=0. \tag{9}$$

If the diagonal component ϵ_m of the tensor is described in the Drude model similarly to Refs. 4 and 5, then the condition (9) assumes the form

$$\omega_r-\omega_p[1+(1-f)\epsilon_0/f]^{-1/2}=0, \tag{10}$$

where ω_r is the frequency of the maximum of α or ψ of the layered structure under study and ω_p is the plasma frequency of the metal. When the condition (9) holds, the coefficients of γ' and γ'' in Eqs. (2)–(3) become equal. If γ' and γ'' have the same signs, then α passes through a maximum and ψ passes through zero. Conversely, if γ' and γ'' have different signs, then α passes through zero and ψ passes through a maximum. In the experiment shown in Figs. 1a and b (curves *4*), α passes through a maximum and ψ passes through zero near 1.7 eV. Since $f\cong 0.3$ and $\epsilon_0\cong 5.3$, (10) the value $\omega_p\approx 6$ eV is obtained for the plasma frequency in Co in a thin-film state; this is consistent with the estimates in Ref. 7.

In summary, we have shown that a medium consisting of layers of a magnetic metal and a nonmagnetic insulator with thicknesses much less than the wavelength of light acquires new physical properties if the number of layers is sufficiently large. We have shown experimentally that a resonance maximum of the Faraday effect appears in such a medium. Apparently, this can be explained on the basis of the theoretical analysis performed in Refs. 3–5. However, the question of the effect of the number of layers on the properties of the medium has not been studied theoretically.

This work was supported by the Russian Fund for Fundamental Research (Grant No. 95-02-03669).

[a)]e-mail: ise@iph.krasnoyarsk.su

---

[1]I. S. Édel'man, T. P. Morozova, V. N. Zabluda *et al.*, JETP Lett. **63**, 273 (1996).
[2]I. Edelman, T. Morozova, V. Zabluda *et al.*, J. Magn. Magn. Mater. **161**, 299 (1996).
[3]M. Abe and M. Gomi, Jpn. J. Appl. Phys. **23**, 1580 (1984).
[4]P. M. Hui and D. Stroud, Appl. Phys. Lett. **50**, 950 (1987).
[5]T. K. Xia, P. M. Hui, and D. Stroud, J. Appl. Phys. **67**, 2736 (1990).
[6]K. H. Clemens and J. Jaumann, Z. Phys. **173**, 135 (1967).
[7]A. S. Davydov, *The Theory of Solids* [in Russian], Nauka, Moscow, 1976, p. 98.

Translated by M. E. Alferieff

Submillimeter electron–nuclear excitation spectra in $CsCdBr_3:Ln^{3+}$ (Ln=Tm, Ho) crystals

V. F. Tarasov and G. S. Shakurov
Kazan Physicotechnical Institute, Kazan Science Center of the Russian Academy of Sciences, 420029 Kazan, Russia

B. Z. Malkin[a)] and A. I. Iskhakova
Kazan State University, 420008 Kazan', Russia

J. Heber and M. Altwein
Technical University of Darmstadt, 64289 Darmstadt, Germany

(Submitted 25 February 1997)
Pis'ma Zh. Éksp. Teor. Fiz. **65**, No. 7, 535–540 (10 April 1997)

The ESR spectra of single and pair impurity centers of thulium and holmium ions in $CsCdBr_3:Tm^{3+}$ and $CsCdBr_3:Ho^{3+}$ crystals are measured in the frequency range 160–400 GHz. Analysis of the characteristic features of the hyperfine structure of the ESR lines and analysis of the variations in the spectra as a function of the temperature and external magnetic field shows that the Ln^{3+} ions substitute for Cd^{2+} ions and predominantly form symmetric pair centers of the type Ln^{3+}–(vacancy at a neighboring Cd^{2+} site)–Ln^{3+}. The ESR spectra of $CsCdBr_3:Ln^{3+}$ crystals are used to make a positive identification of the optical spectra of selective laser excitation. © *1997 American Institute of Physics.* [S0021-3640(97)00907-9]

PACS numbers: 76.30.Kg, 61.72.Hh

1. Lanthanide-ion-activated crystals of compound bromides $CsCdBr_3$ are being intensively studied as promising highly efficient converters of semiconductor laser radiation.[1–7] A hexagonal crystal lattice (space group D_{6h}^4 (Ref. 8)) was constructed from parallel chains of $CdBr_6$ octahedra, extending along the trigonal axis (the symmetry axis of the crystal) and possessing faces in common; the chains are coupled with one another by the Cs^+ ions at the centers of polyhedra consisting of 12 Br^- ions. Trivalent impurity ions in $CsCdBr_3$ crystals exhibit an unusual tendency to form pair centers subtituting for three neighboring Cd^{2+} ions; as a result, an electrically neutral linear dimer with C_{3v} local symmetry forms at the position of the impurity ion parallel to the symmetry axis of the crystal. In Ref. 9 it was concluded on the basis of an investigation of the microwave ESR spectrum of $CsCdBr_3:Gd^{3+}$ crystals that it is predominantly symmetric dimers, in which the impurity ions are located on different sides of a vacant Cd^{2+} site, that form, and the distance between the Gd^{3+} ions was estimated to be 5.93 Å at 77 K. It was conjectured on the basis of data from optical investigations that, together with symmetric dimers, asymmetric pair centers in which the impurity ions lie in the same side of the vacancy are formed.[5,10] The measurements of submillimeter ESR spectra of Tm^{3+}- and Ho^{3+}-activated $CsCdBr_3$ crystals performed in the present work provided direct proof of

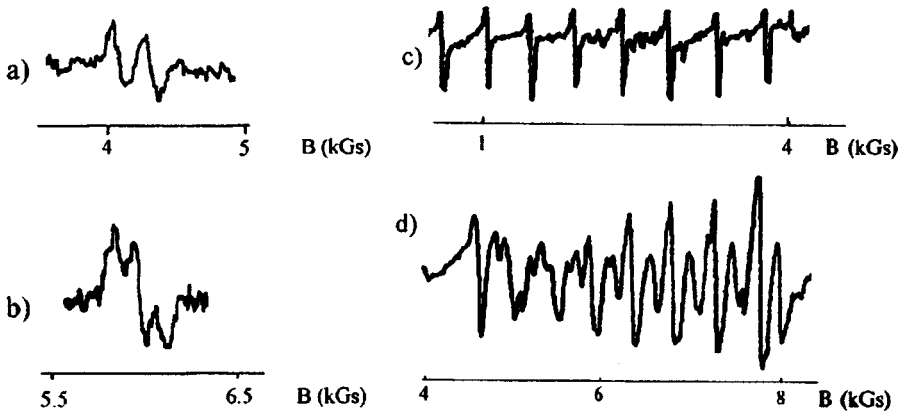

FIG. 1. ESR signals in parallel fields ($\mathbf{B}(t) \parallel \mathbf{B} \parallel c$) in $CsCdBr_3:Tm^{3+}$ (a, b) and $CsCdBr_3:Ho^{3+}$ (c, d) crystals. a) Single center, frequency 300.5 GHz; b) symmetric dimer, frequency 354.5 GHz; c) single center, frequency 238 GHz; d) symmetric dimer, frequency 324 GHz.

the formation of pair symmetric and single centers of trigonal symmetry; it was found that it is possible to make a strict identification of the corresponding optical selective-excitation spectra. Asymmetric pair centers were not found in the samples which we investigated. We note that ESR signals, corresponding to magnetic dipole transitions between two singlet electronic states, from pair centers of Ho^{3+} ions (with an interionic separation of 4.4 Å) in the submillimeter region of the spectrum have been observed in holmium nicotinate, but it was impossible to make a detailed analysis of the measured spectrum because the magnetic moment was not aligned along the axis of the dimer and there were two types of magnetically nonequivalent dimers present.[11]

2. The measurements were performed on an ESR spectrometer using backward-wave tubes as generators in the frequency range 160–400 GHz. A detailed description of the spectrometer is given in Ref. 12. The experiments were performed at a temperature of 4.2 K and a series of measurements were performed with the samples heated to 12 K. The constant magnetic field **B** (from 0 to 10 kG) was parallel to the symmetry axis of the crystal. The variable magnetic field $\mathbf{B}(t)$ was oriented either parallel or perpendicular to the constant magnetic field. The measurements were performed on samples containing 0.5 and 1 at.% Tm and 0.5 at.% Ho. The samples were grown by the Bridgman method.[5]

The ESR signals of $CsCdBr_3:Tm^{3+}$ crystals were observed only in parallel fields. Two lines with resolved hyperfine structure were observed in the spectrum of samples with a low $^{169}Tm^{3+}$ (nuclear spin $I=1/2$) density. One line possesses a doublet structure and can be referred to isolated Tm^{3+} ions. The second line has a triplet structure and corresponds to signals from symmetric dimers. The corresponding lines, but wider, were also observed in a sample with a high density of thulium. In addition, a weak line whose intensity increased substantially with increasing temperature was observed in the spectrum of these samples at 4.2 K. This line is due to transitions between the excited sublevels of a symmetric pair center. The shape of the signals from the single and pair centers is shown in Fig. 1a and b. The intervals of the hyperfine structure increase in

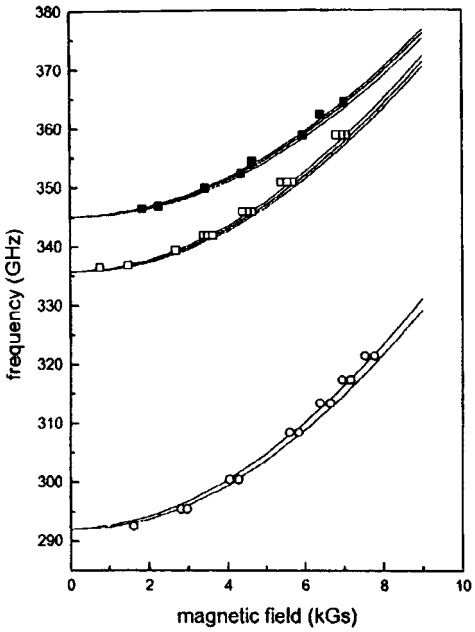

FIG. 2. Frequency spectrum of electron–nuclear excitations in a $CsCdBr_3$:Tm^{3+} crystal. Solid lines — computational results obtained with the CF parameters for single and pair (in parentheses) centers, respectively: $B_2^0 = -73.3(-75.8)$, $B_4^0 = -80.8(-83.9)$, $B_6^0 = 10.7(12.8)$, $B_4^3 = 2120(2227)$, $B_6^3 = 134(175)$, $B_6^6 = 87.5(135.2)$ cm^{-1}. The circles (single centers) and squares (pair centers) represent the experimental data.

proportion to the static magnetic induction. The magnetic field dependence of the resonance frequencies is displayed in Fig. 2.

Since the nuclear spin of the Ho^{3+} ion equals 7/2, the structure of the spectra of the $CsCdBr_3$:Ho^{3+} crystal were much more complicated. The lines of the single and pair centers overlap, but it turned out that they could be distinguished according to the characteristic magnetic field dependence of the hyperfine structure. A well-resolved hyperfine structure (eight components) of two lines of a doublet–doublet transition in single centers was observed in parallel fields; this structure corresponds to the case when the signs of the g factors of the ground and excited states are different (see Fig. 3). In a transverse experimental geometry, a line due to the doublet–doublet transition in single centers and possessing a characteristic hyperfine structure with 16 components was also observed. The ESR signals of pair centers of the holmium ions were observed in both parallel and transverse fields. In the latter case, a doublet–singlet transition line was observed together with doublet–doublet transition. The hyperfine structure of the lines of pair centers is the result of a superposition of several electronic transitions with close frequencies, the difference between which is determined by the interionic interaction in the dimer. In the case of a magnetic dipole–dipole interaction this difference of the frequencies is comparable in order of magnitude to the hyperfine interaction constant of Ho^{3+} ions. The shape of the ESR signals from single and symmetric pair centers in parallel fields is displayed in Figs. 1c and d.

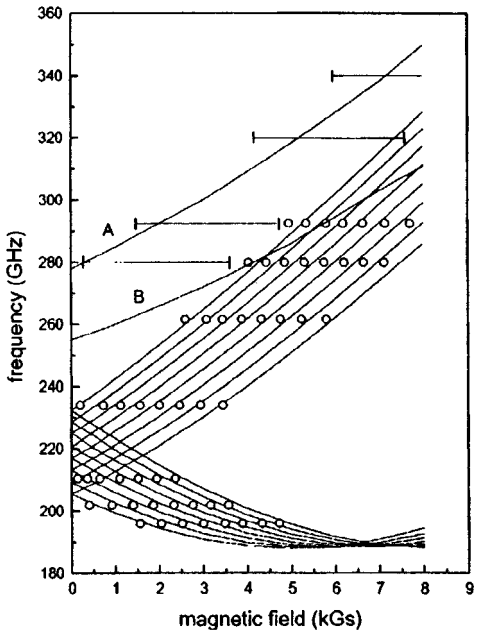

FIG. 3. Spectrum of longitudinal electron–nuclear excitations in a $CsCdBr_3$:Ho^{3+} crystal ($\mathbf{B} \parallel c$): $B_2^0 = -76.8(-77.6)$, $B_4^0 = -79.8(-90.3)$, $B_6^0 = 9.5(14.5)$, $B_4^3 = 2840(2750)$, $B_6^3 = 245.3(192.7)$, $B_6^6 = 108.3(145.8)$ cm^{-1} (see Fig. 2). The curves *A* and *B* determine the upper and lower limits of one of the bands of the computed excitation spectrum of a symmetric dimer. The horizontal segments represent the results of the measurements of the resonance magnetic fields.

Besides the above-described signals, the spectra of the experimental samples contain a series of weak lines, to identify which additional measurements measurements must be performed.

3. The states of a rare-earth ion within the ground-state multiplet with total angular momentum **J** are described by the Hamiltonian

$$H_i = H_{0i} + g_J \mu_B \mathbf{B} \cdot \mathbf{J}_i + A \mathbf{J}_i \cdot \mathbf{I}_i , \tag{1}$$

where i is the number of the ion, μ_B is the Bohr magneton, g_J is the Landé factor, A is the hyperfine structure constant,

$$H_0 = B_2^0 O_2^0 + B_4^0 O_4^0 + B_4^3 O_4^3 + B_6^0 O_6^0 + B_6^3 O_6^3 + B_6^6 O_6^6$$

is the energy of the ion in the crystal field (CF), and O_p^k are Stevens operators. The Hamiltonian of the dimer (we take into account explicitly only the magnetic dipole-dipole interaction; R is the distance between the ions) has the form

$$H = H_1 + H_2 + \frac{(g_J \mu B)^2}{R^3} (J_{x1} J_{x2} + J_{y1} J_{y2} - 2 J_{z1} J_{z2}). \tag{2}$$

According to calculations of the local structure of a lattice with an isolated symmetric pair center, the distances between the thulium and holmium ions equal 5.943 and 5.937

Å, respectively.[13] Therefore, for prescribed single-ion parameters (specifically, we assumed in the present work that the hyperfine interaction constants equal their values in the free ions), the electron–nuclear interaction spectra are described completely by the CF parameters B_p^k. The values of the CF parameters (see the captions to Figs. 2 and 3) were obtained by varying the initial parameters found in the exchange-charge model,[13] and by comparing the computed and measured ESR spectra. The Stark structure calculated for the Tm^{3+} and Ho^{3+} multiplets using these CF parameters agrees with the optical measurements.[3,7,13] Specifically, for single Tm^{3+} centers the energies of the sublevels of the $^3H_6$ multiplet equal (the values obtained by the selective laser spectroscopy and the symmetry — the irreducible representations of the C_{3y} group — of the corresponding states are given in parentheses): 0 (0, Γ_1), 9.7 (9.7, Γ_2), 71.6 (75, Γ_3), 87 (99.5, Γ_1), 109 (121, Γ_3), 198 (236, Γ_2), 277 (296, Γ_3), 296 (320, Γ_1), 306 (340, Γ_3) cm^{-1}. In symmetric dimers the relative changes in the energies of these states are not large: 0 (0, Γ_1), 11.34 (11.7, Γ_2), 73.5 (76.7, Γ_3), 91.2 (101.2, Γ_1), 112.8 (122.6, Γ_3), 195 (238, Γ_2), 290 (298, Γ_3), 317 (328, Γ_1), 324 (?, Γ_3) cm^{-1}.

The ground (Γ_1) and nearest excited (Γ_2) singlet states of the Tm^{3+} ion (with energy difference Δ) mix very little with the other sublevels of the $^3H_6$ multiplet in a magnetic field. In this case the following effective spin Hamiltonian ($S=1/2$) can be used to calculate the spectra of singlet–singlet transitions of a symmetric dimer:[14]

$$H_{\text{eff}}=\Delta(S_{x1}+S_{x2})+g\mu_B B_z(S_{z1}+S_{z2})+a(S_{z1}I_{z1}+S_{z2}I_{z2})+4\epsilon S_{z1}S_{z2}, \tag{3}$$

where

$$g=2gJ\langle\Gamma_1|J_z|\Gamma_2\rangle, \quad a=2A\langle\Gamma_1|J_z|\Gamma_2\rangle, \quad \epsilon=-2\langle\Gamma_1|J_z|\Gamma_2\rangle^2\frac{(g_J\mu_B)^2}{R^3}.$$

To within terms which are linear in the hyperfine interaction constant A, the energies of the four electron–nuclear states of an isolated Tm^{3+} ion are $E=\pm 1/2[\nu_e^2\pm g\mu_B Ba]^{1/2}$, where $\nu_e=[\Delta^2+(g\mu_B B)^2]^{1/2}$.

The variable magnetic field $B_z(t)$ induces transitions only between states with identical projections of the nuclear spin with frequencies (we assume $\hbar=1$) $\nu_m=[\nu_e^2+mg\mu_B Ba]^{1/2}$, where $m=\pm 1$.

The energy levels of pairs of ions (a and b) and the corresponding wave functions are as follows (we construct the electronic wave functions as products $|1\rangle=|+\rangle_a|+\rangle_b$; $|2\rangle=|+\rangle_a|-\rangle_b$; $|3\rangle=|-\rangle_a|+\rangle_b$; and $|4\rangle=|-\rangle_a|-\rangle_b$, where $|\pm\rangle$ are the eigenfunctions of the operator S_z, and we represent the eigenfunctions of the total nuclear angular momentum $I=1,\ 0$ as $|I,m\rangle$, where $m=I_z=0,\ \pm 1$):

$$E_m(\pm)=\pm\left(\nu_m+\epsilon\left(1-\frac{\Delta}{\nu_m}\right)^2\right), \quad \Psi_{Im}(\pm)=0.5(|1\rangle+|4\rangle\pm|2\rangle\pm|3\rangle)|I,m\rangle;$$

$$E_m(1)=-\epsilon, \quad \Psi_{Im}(1)=(|2\rangle-|3\rangle)|I,m\rangle/\sqrt{2};$$

$$E_m(2)=\epsilon\left(\left(2-\frac{\Delta}{\nu_m}\right)^2-1\right), \quad \Psi_{Im}(2)=(|1\rangle-|4\rangle)|I,m\rangle/\sqrt{2},$$

where the frequencies ν_{+1} and ν_{-1} were defined above, and $\nu_0 = \nu_e$. At low temperatures ($T \ll \Delta/k$) magnetic dipole transitions $E(-) \leftrightarrow E(2)$ with the frequencies $\nu_m = \epsilon(3(\Delta/\nu_m)^2 - 2) + \nu_m$ can be observed and, in contrast to the spectrum of a single Tm^{3+} ion with a doublet hyperfine structure, the spectrum of a symmetric dimer contains three lines with intervals $g\mu_B Ba/2\nu_e$, the intensity of the central component being two times greater than that of the outer components. Information about the relative arrangement of the Tm^{3+} ions can be obtained from the value of the coupling constant ϵ; this constant, determined from the difference of the frequencies of the transitions $E(-) \leftrightarrow E(2)$ and $E(2) \leftrightarrow E(+)$, agrees with the proposed model of a symmetric dimer. The transition frequencies computed in the approximation under study (see Fig. 2, $A = -0.389$ GHz, $g = 12.30$ in the dimer and 12.39 for a single center) are practically identical to the results obtained by diagonalizing the complete matrices of the operators (1) and (2).

Our computed energies of the Stark sublevels of the $^5I_8$ multiplet of the Ho^{3+} ions in single and pair centers, respectively, are (the values obtained in Ref. 3 by optical spectroscopy are presented in parentheses): 0 (Γ_3), 6.67 and 5.55 (Γ_2, 5.5), 7.25 and 8.8 (Γ_3, 9), 22.8 and 28.1 (Γ_1, 26), 142 and 151 (Γ_3, 155), 162 and 158 (Γ_2, 162), 159 and 177 (Γ_3, 178), 169 and 183 (Γ_1, 188), 184 and 193 (Γ_1, 190.53), 207 and 211 (Γ_3, 217), 221 and 216 (Γ_3, 237) cm^{-1}. The measured ESR spectrum of Ho^{3+} ions corresponds to magnetic dipole transitions within the lower group of Stark sublevels of the ground-state multiplet $^5I_8$ (doublet–singlet–doublet). In an external magnetic field this group mixes substantially with other states, so that it is impossible to study the spectrum analytically. For single centers the electron–nuclear excitation spectrum was found by diagonalizing the complete rank-136 matrix of the operator (1). The spectrum of longitudinal and transverse excitations (with magnetic moments directed parallel and perpendicular to the constant magnetic field, respectively) for a symmetric pair center of the Ho^{3+} ions was calculated in several steps. First, the energies and wave functions of the Zeeman sublevels of the $^5I_8$ multiplet was calculated with a given magnitude of the magnetic field. The magnetic dipole-dipole interaction operator is treated as a perturbation, determined as the direct product of the spaces of the wave functions of the five lowest electronic states of two ions. Numerical diagonalization of the matrix of the hyperfine interaction operator taking account of the 16 bottom electronic states (rank 1024) gives the energies and wave functions of the electron–nuclear states of the dimer. The absorption spectrum in a fixed magnetic field at low temperatures was obtained, specifically, as an envelope of the sum of the Gaussian lines of transitions from 256 states, genetically related with the bottom electronic doublets, with integral intensities equal to the squared moduli of the corresponding matrix elements of the operators $J_{1z} + J_{2z}$ for longitudinal excitations and $J_{1x} + J_{2x}$ for transverse excitations. The computational results agree well with the measurements. A detailed description of the spectra will be presented in a more detailed paper. Here we only note that three lines with an eight-component structure (see Fig. 1d) can be distinguished in the spectrum of the longitudinal excitations (the corresponding frequency region is shown in Fig. 3); the relative position and relative intensities of these lines vary in a magnetic field.

We are grateful to the Russian Fund for Fundamental Research (Grant No. 96-02-18263) and the German Academic Exchange Office (DAAD) for financial support.

[a)]e-mail: boris.malkin@ksu.ru

[1] R. B. Barthem, R. Buisson, and R. L. Cone, J. Chem. Phys. **91**, 627 (1989).
[2] N. J. Cockroft, G. D. Jones, and D. C. Nguyen, Phys. Rev. B **45**, 5187 (1992).
[3] M. Mujaji, G. D. Jones, and R. W. G. Syme, Phys. Rev. B **48**, 710 (1993).
[4] R. Ramaz, R. M. Macfarlane, J. C. Vial *et al.*, J. Lumin. **55**, 173 (1993).
[5] J. Neukum, N. Bodenschatz, and J. Heber, Phys. Rev. B **50**, 3536 (1994).
[6] F. Pelle, N. Gardant, M. Genotelle *et al.*, J. Phys. Chem. Solids **56**, 1003 (1995).
[7] K. M. Murdoch and N. J. Cockroft, Phys. Rev. B **54**, 4589 (1996).
[8] G. L. McPherson, A. M. McPherson, and J. A. Atwood, J. Phys. Chem. Solids **41**, 495 (1980).
[9] L. M. Henling and G. L. McPherson, Phys. Rev. B **16**, 4756 (1977).
[10] C. Barthou and R. B. Barthem, J. Lumin. **46**, 9 (1990).
[11] V. F. Tarasov, G. S. Shakurov, B. Z. Malkin *et al.*, J. Alloys Compounds (1996), in press.
[12] V. F. Tarasov and G. S. Shakurov, Appl. Mag. Res. **2**, 571 (1991).
[13] B. Z. Malkin, M. Rodionova, and J. Heber, in press.
[14] J. M. Baker, C. A. Hutchison Jr., and P. M. Martineau, Proc. R. Soc. London, Ser. A **403**, 221 (1986).

Translated by M. E. Alferieff

Parity effect and charge-binding transition in submicron Josephson junction arrays

M. V. Feigel'man, S. E. Korshunov, and A. B. Pugachev
L. D. Landau Institute of Theoretical Physics, Russian Academy of Sciences, 117940 Moscow, Russia

(Submitted 3 March 1997)
Pis'ma Zh. Éksp. Teor. Fiz. **65**, No. 7, 541–546 (10 April 1997)

We reconsider the Berezinskiĭ–Kosterlitz–Thouless (BKT) transition to an insulating state in Coulomb-dominated Josephson junction arrays. We show that the previously predicted picture of the Cooper-pair BKT transition at $T=T_2$ is valid only under the condition that T_2 is considerably below the parity-effect temperature $T^*\approx 0.1\Delta$, and that even in that case it is not a rigorous phase transition but only a crossover, whereas the real phase transition takes place at $T_1\approx T_2/4$. Our theory is in agreement with available experimental data on Coulomb-dominated Josephson arrays and also sheds some light on the origin of the unusual reentrant temperature dependence of the resistivity in an array with a nearly critical ratio E_C/E_J. © *1997 American Institute of Physics.* [S0021-3640(97)01007-4]

PACS numbers: 74.50.+r, 74.80.Dm, 73.23.Hk

1. Two-dimensional arrays of micron-scale superconducting islands have been extensively studied in recent years, both experimentally[1–4] and theoretically.[5–7] It is now well established that their low-temperature behavior is determined by a competition between the Josephson coupling energy E_J and the effective charging energy $E_C=e^2/2C$, where C is some relevant electrical capacitance (to be discussed below). Macroscopic superconductive coherence is observed at low temperatures in arrays with $E_J\gg E_C$, whereas arrays with $E_J\ll E_C$ show insulating behavior at $T\to 0$. At nearly critical values of the ratio $x=E_J/E_C\sim x_{\rm cr}$ a direct transition between superconducting (SC) and insulating (I) behavior as function of x is observed in zero magnetic field.[2] Moreover, a very weak magnetic field $B\leqslant 1$ G (producing small fractions of a flux quantum per unit cell of the array) was found to switch arrays with $x\approx x_{\rm cr}$ between SC-like and I-like behavior as a function of temperature; recently a very interesting intermediate region was found[2] in which the resistance $R(T)$ is basically constant in the temperature range 10 mK$\leqslant T\leqslant$200 mK, which indicates the existence of a ''2D metal'' state sandwiched between the SC and I phases.

The above-mentioned basic properties of 2D arrays are in qualitative agreement with the existing theories[5,7] (except for the recently observed 2D metal state); however several important features are not yet understood. In particular, the resistance of the insulating arrays shows purely activational behavior $R(T)\propto\exp(E_a/T)$ with a constant activation energy E_a throughout the whole temperature interval studied,[2–4] whereas theoretically the charge-binding Berezinskiĭ–Kosterlitz–Thouless (BKT) transition[8,9] from the conducting

to the insulating phase is expected to occur[5] at a temperature $T_2 \approx E_C/\pi$. Such a transition should occur due to the nearly logarithmic form of the Coulomb interaction between charges in arrays in which the self-capacitance C_0 of the islands is very small compared to the inter-island (junction) capacitance C. In the currently studied arrays the ratio $C/C_0 \sim 100$ (as measured at very low temperatures, about 10 mK, cf., e.g., Ref. 2), which should result in a logarithmic interaction throughout the whole array (the effective interaction length Λ should be estimated with allowance for the 3D nature of the electric field, which leads[2,10] to $\Lambda \sim C/C_0 \sim 100$) and, consequently, in a charge-binding BKT transition.

In the case of islands in the SC state and under the condition $E_J \ll E_C$ the temperature of this transition has been estimated[5] as $T_2 \approx E_C/\pi$, whereas in the case of normal islands (i.e., with superconductivity suppressed by a magnetic field) it is expected to be a factor of 4 lower, $T_1 \approx E_C/4\pi$, due to the twofold decrease of the available elementary charge. Nevertheless, no indication of such a transition in an array of SC islands has been found experimentally (except in a very recent preprint,[11] which is discussed below). Another surprising feature observed in Ref. 2 is the nonmonotonic (''reentrant'') temperature behavior of the resistance $R(T)$ of an array with a nearly critical ratio E_J/E_C at $T \leqslant 200$ mK.

In the present letter we show that the above experimental observations can be naturally understood once the temperature dependence of the effective Coulomb-interaction between the charges in an array is properly taken into account. In a very broad sense our analysis follows the ideas of Efetov,[12] who laid a groundwork for the description of quantum fluctuations in granular superconductors; namely, we consider the screening of the Cooper-pair Coulomb-interaction by normal quasiparticles existing in each superconductive island at finite temperatures. However, we believe that Efetov's treatment of the effect he proposed was technically not quite correct, and we therefore present here another theoretical approach to the same problem.

Our main qualitative result can be formulated as follows: at temperatures above the so-called parity-effect[13–16] temperature $T^* \approx \Delta/\ln \mathcal{M} \ll \Delta$ [where $\mathcal{M} = V\nu(0)\sqrt{8\pi T\Delta} \sim 10^4$–$10^5$, V is the volume of the island, and $\nu(0)$ is the density of states at the Fermi level in absence of superconductivity] the presence of thermal quasiparticles [numbering $\sim \mathcal{M} \exp(-\Delta/T) \gg 1$] on each island rules out any possibility of observing the BKT transition of Cooper pairs at T_2. Since in most of the arrays studied to date the above-defined characteristic temperature T_2 has been in the range 0.3–0.5 K, whereas the parity-effect temperature $T^* \approx 0.2$ K $< T_2$, the absence of anything like a BKT transition near T_2 is quite natural (measurements below T^* were not possible in these arrays[3,4] since $R(T)$ becomes immeasurably high [$\geqslant 10^9 \Omega$]). On the other hand, a single-electron BKT transition is a completely different issue: we *do* expect such a transition to be observable at approximately the same temperature $T_1 \approx T_2/4$ as in arrays with islands in the normal state.

2. Let us now proceed to the derivation of our results. With one important modification, we will follow Ref. 5. In the limit when charge tunneling is weak and is important only for the establishment of thermodynamic equilibrium, an array of superconducting islands can be described by a classical partition function of the form:

$$Z=\sum_{\{n\}}\exp\left[-\frac{1}{2}\sum_{i,j}G_{ij}n_in_j-\frac{D}{T}\sum_j\frac{1-(-1)^{n_j}}{2}\right],\quad G_{ij}=\frac{e^2}{T}C_{ij}^{-1}. \tag{1}$$

The first term in the exponent in Eq. (1) stands for the electrostatic energy of the array, which in the case when only the mutual capacitance C of nearest-neighbor islands is of importance corresponds to a logarithmic interaction of the charges in a two-dimensional array:

$$G_{i=j}-G_{ij}\approx\frac{2E_C}{T}\left(\frac{1}{2\pi}\ln R_{ij}+\frac{1}{4}\right),\quad E_C=\frac{e^2}{2C}, \tag{2}$$

whereas the second term describes the dependence of the free energy of a superconducting island on the parity of the number of electrons n_j on this island.[13,15,16]

The free energy difference $D(T)$ between the islands with odd and even numbers of electrons can be expressed as

$$D(T)=-T\ln\tanh(\Omega_{oe}/T). \tag{3}$$

where $\Omega_{oe}=-T\ln(Z_{\rm odd}/Z)$ and $Z_{\rm odd}$ is the ''odd grand canonical partition function'' introduced in Ref. 13 in a study of the parity effect. An exact expression for the function $\Omega_{oe}(T)$ can be found in Ref. 15, but for $T\ll\Delta$ a good approximation is

$$\Omega_{oe}(T)/T\approx\mathcal{M}e^{-\Delta/T},\quad \mathcal{M}=V\nu(0)\sqrt{8\pi T\Delta}. \tag{4}$$

The ratio Ω_{oe}/T in that limit is proportional to the number of thermally excited quasiparticles on one island.

In terms of statistical mechanics, partition function (1) defines a Coulomb lattice gas in which the fugacities of odd charges $Y=\exp(-D/T)$ differ from the fugacities of even charges (which are equal to one). Comparison of Eq. (4) with Eq. (3) for $T\ll T^*=\Delta/\ln\mathcal{M}$ then shows that the parity-dependent free energy difference $D(T)\approx\Delta-T\ln\mathcal{M}\gg T$ and so $Y\ll 1$, whereas in the opposite limit $T\gg T^*$ the quantity $D(T)$ becomes exponentially small and Y is very close to one.

Previously it has been assumed[5] that in the regime when island charges behave as classical variables the main difference between an array of normal islands and an array of superconducting islands is that in an array of normal islands the charge of each island is quantized in units of e, whereas in an array of superconducting islands the charge is quantized in units of $2e$. The consequence for an array whose electrostatic properties are dominated by mutual capacitance of nearest neighbors is that the temperature T_2 of the BKT transition in an array of superconducting islands (appearance of free double charges) should be exactly four times higher than the temperature $T_1\sim E_C/4\pi$ of the BKT transition in the analogous array of normal islands (the appearance of free single charges). Comparison with Eq. (1) shows that such a description of an array of superconducting islands would be correct only in the limit $D(T)/T\to\infty$. Since $D(T)$ is always finite this description turns out to be misleading. The behavior of the array at temperatures close to $T_2=E_C/\pi$ depends qualitatively on the relation between T_2 and T^*; we consider both cases in turn.

3. At $T_2\geqslant T^*$ an array of superconducting islands is described by practically the same partition function as an array of normal islands, since $D(T_2)\ll T_2$ in that case. The phase transition to the insulating state in such a system can be associated with the binding

of the charges ± 1 into neutral pairs; it takes place at a temperature T_1 which is slightly lower than the simple estimate $T_1^{(0)}=E_C/4\pi$ which can be obtained by comparison of the energy of a single charge with its entropy. The difference between T_1 and $T_1^{(0)}$ is due to the renormalization of the charge interaction by bound pairs of charges and decreases with decreasing fugacities. The appearance of the free single charges induces screening of the Coulomb-interaction for all types of charges, and therefore the double charges also are free at $T>T_1$. Not even a trace of a separate phase transition related to the debinding of double charges can be expected to be observed in such a situation, which corresponds to the experiments of Refs. 1–4.

4. In the opposite case $T_2<T^*$ there is a range of temperatures $T_2<T<T^*$ in which the fugacity Y of single charges is much smaller than one. This leads to an increase in the phase transition temperature, but it still has to remain lower than $T_1^{(0)}$. The difference with the case $Y\approx 1$ is that for $Y\ll 1$ the concentration n_1 of free single charges remains small even at temperatures considerably higher than T_1. In the region $T_1<T<T_2$ this concentration can be estimated with the use of the standard Debye–Hückel approximation, which gives for n_1 the self-consistent equation

$$n_1=2Y\exp\left\{-\frac{1}{2}\int\frac{d^2\mathbf{q}}{(2\pi)^2}\,\frac{1}{K[2(1-\cos\,q_x)+2(1-\cos\,q_y)]+n_1}\right\} \tag{5}$$

(where $K=T/2E_C$), the solution of which for small n_1 can be expressed as

$$n_1\approx 2\,\exp\left\{-\frac{D(T)+aE_C-[\ln(4E_C/T)]E_C/4\pi}{T-T_1^{(0)}}\right\}, \tag{6}$$

where $a=0.276\ldots$. The main effect of the Coulomb interaction is that it produces a singularity at $T=T_1^{(0)}$ in the exponent in Eq. (6). When the shift of the phase transition temperature is taken into account, $T_1^{(0)}$ should be replaced by T_1. Note that second and third terms in the numerator of the exponent almost cancel each other in the relevant range of parameters.

For $D(T)\gg T$ the screening of the interaction is noticeable only on large scales, and the concentration of free double charges also remains small. On the other hand, at the temperature $T_2=4T_1\approx E_C/\pi$ the free double charges have to appear even when $Y=0$ on account of the mutual influence of pairs of double charges (cf. Ref. 5). That means that for $D(T)\gg T$ a crossover characterized by a proliferation of free double charges occurs in the vicinity of T_2.

Close to the transition temperature T_1 the self-consistent approximation is no longer valid, and more advanced methods should be used. It is easy to show that when only the single and double charges are taken into account, the Coulomb gas model described by partition function (1) becomes isomorphic (in the continuous approximation) to the sine–Gordon model defined by the Hamiltonian

$$H=\int d^2\mathbf{r}\left[\frac{K}{2}(\nabla\theta)^2-2Y\cos\,\theta-2\,\cos\,2\theta\right];\quad K=\frac{T}{2E_C}. \tag{7}$$

The renormalization group equations for the Hamiltonian (7) can be found in Ref. 17. As expected, their solution shows that for temperatures lower than T_2 the presence of double

charges (in form of neutral pairs) does not introduce any qualitative changes. In the close vicinity of T_1 the temperature dependence of n_1 deviates from the self-consistent result (6) and exhibits the standard BKT critical behavior[9] with

$$n_1(T) \propto \exp\left[-\frac{b}{\sqrt{1-T/T_1}} \right], \tag{8}$$

where b is of the order of unity. The linear dc resistance of the array should be inversely proportional to the density of free charges n_1. Taking into account Eqs. (6) and (8), we get an estimate for this resistance at temperatures near T_1:

$$\ln\frac{R(T)}{R_1} \approx \min\left[\frac{D(T)}{T-T_1}, \frac{b}{\sqrt{4\pi}}\left(\frac{E_C}{T-T_1} \right)^{1/2} \right], \tag{9}$$

where R_1 is inversely proportional to the probability of a tunneling event, which is only weakly dependent on the temperature: $R_1 \sim R_n \mathcal{M}$, where R_n is the normal-state tunneling resistance (cf. Ref. 18).

5. The representation (7) is also useful for comparison between our results and Efetov's treatment of screening by quasiparticles,[12], which can be expressed just as the replacement of the original capacitance matrix C_{ij} by an ''effective'' one defined (at $T \ll \Delta$) as

$$C_{ij}^{\text{eff}} = C_{ij} + \delta_{ij} \cdot V\nu(0)(2e)^2 \sqrt{\frac{2\pi\Delta}{T}} e^{-\Delta/T}. \tag{10}$$

Let us now formally expand the second term in Eq. (7) to second order in θ and neglect the rest of terms. One can easily see that the expression obtained in this way for the effective interaction between $2e$ charges (generated by expansion of the partition function in powers of the $\cos 2\theta$ term) would coincide with the expression obtained by inversion of the effective capacitance (10). Physically the formal operation above would mean neglect of the discrete nature of electric charge, which might be reasonable if charge transport between islands could proceed via some ''classical'' channels able to provide charge in continuous amounts (like the charging of a macroscopic electrical capacitor by an external voltage source). It is not the case for submicron arrays with tunnel junctions, where the charges of the islands can change only by a quantum $1e$ (as is reflected by the periodic nature of the second term in Eq.(7)). However, the basic qualitative feature of Efetov's result — the screening of Cooper pair charges by normal excitations — remains valid in spite of the absence of any such simple notion as an effective capacitance matrix.

6. It follows from our results that in order to observe some growth of the effective activation energy [defined as $E_a = d \ln R(T)/d(1/T)$] as T approaches T_2 from above, one needs to use an array with a Coulomb energy E_C several times less than Δ, so that $T_2 \leqslant T^*$. This conclusion is in complete agreement with recent experimental data,[11] where some moderate growth of $E_a(T)$ in the temperature range around 0.2–0.3 K was observed. This experiment differs from several previous ones of the same type[2–4] (where a constant E_a was observed) by having lower values of E_C and a bit higher reported Δ. On the other hand, we do not agree with the interpretation given in Ref. 11, that the growth of $E_a(T)$ is a precursor of the BKT transition at T_2 for their SC arrays. As follows from our results, no such a transition exists at T_2, which agrees with the rather modest

(compared to BKT behavior) growth of $E_a(T)$ observed in Ref. 11 at $T \sim T_2$. Note that the agreement between the data reported in Ref. 11 for normal arrays and the expected genuine BKT transition at T_1 is much better than the above-mentioned comparison for SC arrays.

The above theoretical results point out that any analysis of experimental data on superconductor–insulator transition in artificial arrays of superconducting islands (as well as in dirty thin films near SC–I transitions) should take into account the existence of a characteristic temperature scale for the parity effect, T^* (note that T^* is magnetic-field dependent and is strongly depressed by fields of the order of H_{c2}). In particular, the behavior of the I–V characteristics in the intermediate temperature range $T^* < T < \Delta$ cannot be unambiguously related to the genuine ground-state properties of the system, as is exemplified by the nonmonotonic behavior of $R(T)$ observed in Ref. 2 at a nearly critical ratio E_J/E_C. We interpret this unusual behavior as follows: at moderately low T screening by quasiparticles is effective and reduces the Coulomb repulsion of Cooper pairs, leading to decreasing behavior of $R(T)$; at still lower T this screening is gone, the Coulomb repulsion increases, and the effective ratio $E_J/E_C^{\rm eff}$ enters the ''insulating'' part of the phase diagram, leading to an increase of $R(T)$ as T is decreased further.

We are grateful to V. B. Geshkenbein, A. Kitaev, N. B. Kopnin, A. I. Larkin, J. E. Mooji, Yu. V. Nazarov, G. Schön, M. Skvortsov and H. van der Zant for many helpful discussions. Financial support from INTAS-RFBR Grant 95-0302 (M.V.F.) and Swiss National Science Foundation collaboration Grant 7SUP J048531 (M.V.F. and A.V.P.), as well as the DGA Grant 94-1189 (M.V.F.) and RFBR Grant 96-02-18985 (S.E.K) is gratefully acknowledged.

[1] H. S. J. van der Zant, F. C. Fritschy *et al.*, Phys. Rev. Lett. **69**, 2971 (1992).
[2] H. S. J. van der Zant, W. J. Elion, L. J. Geerlings, and J. E. Mooji, Phys. Rev. B **54**, 10081 (1996).
[3] T. S. Tighe, M. T. Tuominen, J. M. Hergenrother, and M. Tinkham, Phys. Rev. B **47**, 1145 (1993).
[4] P. Delsing, C. D. Chen, D. B. Haviland *et al.*, Phys. Rev. B **50**, 3959 (1994).
[5] R. Fazio and G. Schön, Phys. Rev. B **43**, 5307 (1991).
[6] R. Fazio *et al.*, Helv. Phys. Acta **65**, 228 (1992).
[7] F. Hekking, G. Schoen and D. Averin (eds.), *Proceedings of the NATO Advanced Research Workshop on Mesoscopic Superconductivity*, Karlsruhe, 1994 [Physica B **203**, Nos. 3–4 (1994)].
[8] V. L. Berezinskiĭ, Zh. Éksp. Teor. Fiz. **59**, 907 (1970) [Sov. Phys. JETP **32**, 493 (1971)]; J. M. Kosterlitz and D. J. Thouless, J. Phys. C **6**, 1181 (1973).
[9] J. M. Kosterlitz, J. Phys. C **7**, 1046 (1974).
[10] J. E. Mooji and G. Schoen, in *Single Electron Tunnelling*, Eds. H. Grabert and M. Devoret, Plenum, New York 1992 (Chapter 8 and references therein).
[11] A. Kanda and S. Kobayashi, submitted to Phys. Rev. B (1996).
[12] K. B. Efetov, Zh. Éksp. Teor. Fiz. **78**, 2017 (1980) [Sov. Phys. JETP **51**, 1015 (1980)].
[13] M. T. Tuominen, J. M. Hergenrother, T. S. Tighe, and M. Tinkham, Phys. Rev. Lett. **69**, 1997 (1992).
[14] F. W. J. Hekking, L. I. Glazman, K. A. Matveev, and R. I. Shekhter, Phys. Rev. Lett. **70**, 4138 (1993); P. Joyez, P. Lafarge, A. Filipe *et al.*, Phys. Rev. Lett. **72**, 2458 (1994).
[15] D. V. Averin and Yu. V. Nazarov, in *op. cit.* 7, p. 310.
[16] L. Glazman *et al.*, in *op. cit.* 7, p. 316.
[17] J. A. Jaszczak and W. F. Saam, Phys. Rev. B **37**, 7619 (1988).
[18] B. Janko and V. Ambegaokar, Phys. Rev. Lett. **75**, 1154 (1995).

Published in English in the original Russian journal. Edited by Steve Torstveit.

Stationary soliton on a charged surface of liquid helium and hydrogen films

A. A. Levchenko,[a)] G. V. Kolmakov, L. P. Mezhov-Deglin, and V. B. Shikin
Institute of Solid-State Physics, Russian Academy of Sciences, 142432 Chernogolovka, Moscow District, Russia

E. Teske and P. Leiderer
Universität Konstanz, D78434 Konstanz, Germany

(Submitted 6 March 1997)
Pis'ma Zh. Éksp. Teor. Fiz. **65**, No. 7, 547–552 (10 April 1997)

A change in the shape of a charged surface of liquid hydrogen and helium — the formation of a solitary wave (a positively charged hump for hydrogen and a negatively charged dimple for helium) – is observed in an electric field exceeding a critical value under conditions of total compensation of the applied field by the surface charge. © *1997 American Institute of Physics.* [S0021-3640(97)01107-9]

PACS numbers: 67.70.+n, 67.55.Hc

It is well known that a flat charged liquid surface in an external perpendicular electric field E becomes unstable when the intensity of the field exceeds a critical value.[1] Previously the change in the shape of a negatively charged surface of a thick layer of liquid helium (the electrons are localized above the helium) has been investigated in detail in the case when the depth d of the liquid (distance from the free surface to the metal substrate) is much greater than the capillary length $\lambda=\sqrt{\alpha/\rho g}$. Here α and ρ are the surface tension and density of liquid helium and g is the acceleration of gravity. The theoretical calculations have been performed under conditions when the electrons localized above the surface do not completely compensate the applied electric field. It was found that for $d\gg\lambda$ and for a fixed number of charges above the surface, when the field exceeds some critical value a periodic deformation, accompanied by modulation of the surface charge density, with a period of the order of λ and a finite amplitude which depends on the degree of supercriticality,[2–4] arises on the surface of the liquid, i.e., a reconstruction — a transition of the liquid surface from a flat surface into a new stable state — is observed. This phenomenon was studied experimentally in Refs. 5–7.

In the opposite situation, when $d\ll\lambda$, the range of wave numbers at which instability develops starts at $k=0$ (Ref. 8), and in the one-dimensional approximation, as follows from Ref. 9, a localized stationary wave (soliton), whose size depends on the applied field, can arise on the surface.

Until recently it was not clear whether or not it is possible to observe reconstruction of a surface under conditions when the distance between the control electrode and the charged surface of the liquid has a value $d\sim\lambda$, and the electric field is completely compensated by a layer of charge on the surface of the liquid.

The surface of liquid helium and hydrogen can be charged, for example, by local-

izing electrons above the surface or positive ions beneath the surface. The problems of the stability and reconstruction of negatively or positively charged liquid surfaces are equivalent. For this reason, in this letter experiments with a negatively charged helium surface are combined with experiments with a positively charged hydrogen surface.

This letter reports the experimental observation of a stationary reconstructed surface of charged helium and hydrogen films under conditions when the charges completely compensate the applied electric field and presents data on the shape of the reconstructed surface. The transition from a flat state into a new reconstructed state is ''soft.'' It is found that the solitary stationary axisymmetric wave (soliton) corresponding to a dimple on a negatively charged liquid-helium surface (electrons above the helium) and a hump on a positively charged liquid-hydrogen surface (positive charges localized beneath the surface) is a stable form of the reconstructed surface.

EXPERIMENTAL PROCEDURE

The properties of a negatively charged liquid-helium surface in the normal state and a positively charged liquid-hydrogen surface were studied in the experiments.

The experimental cells had the form of flat capacitors (diodes) arranged horizontally in cylindrical optical containers. The distance between the capacitor plates was equal to 8 mm in the experiments with liquid helium and 6 mm in the experiments with liquid hydrogen. The diameter of the plates ($D \geqslant 20$ mm) was several times greater than the distance between the plates. The liquid was condensed on the bottom plate of the capacitor. The liquid column was 0.1 and 0.15 mm high for helium and 3 ± 0.1 mm high for hydrogen. We recall that the capillary length in helium $\lambda = 0.4$ mm at $T = 4.2$ K and $\lambda = 1.8$ mm at 17 K for hydrogen, i.e., the distance d between the control electrode (top plate in hydrogen, bottom plate in helium) and the free surface of the liquid was comparable to the capillary length λ.

The liquid-helium surface was charged with electrons with the aid of a pointed tip placed in vapor in the presence of a perpendicular compressing field. The change in the shape of the surface was followed according to the change in the interference pattern produced by two laser beams reflected from the bottom half-transmitting (metallized) plate of the diode and the top, mirror plate. The observational procedure is described in Ref. 10, for example.

In the experiments with liquid hydrogen the bottom plate, coated with a layer of radioactive material, of the diode served as the source of charge. Under the action of the applied electric field the positive charges (H_2^+ ions surrounded by a layer of solidified hydrogen) was pressed against the surface located at a distance d from the top metal electrode; in this case, virtually no current flowed through the surface. The experimental arrangement is described in Ref. 11. The shape of the charged surface was monitored with a TV camera, which gave an image of the profile of the liquid in the gap between the plates of the diode. A change in the shape of the surface with increasing electric field was also judged according to the deflection of the laser beam reflected from the surface of the liquid.

We underscore the fact that the measurements were performed under conditions of a bounded geometry (cylindrical ampul with a diameter several times greater than the

interelectrode distance) and the total amount of liquid in the helium and hydrogen films in the experimental cell remained unchanged.

EXPERIMENTAL RESULTS

For low voltages between the diode plates the equipotentially charged surface of the liquid curves smoothly. When a critical voltage U_{c1} is reached, a macroscopic section (a dimple on the surface of helium and a hump on the surface of hydrogen) with a characteristic diameter of several millimeters appears on the surface. It should be noted that in both helium and hydrogen the reconstructed section could arise on the surface at random points. In the experiments with hydrogen an a single hump could be moved to the center of the diode by slightly changing the inclination of the cell.

Figure 1 shows two interference patterns of the charged surface of a liquid-helium film — before and after the appearance of a deformed section (marked by arrows in Fig. 1b). The diameter of the dark spot at the center of the deformed section equals 1.5 mm. The potential difference between the diode plates was $U=170$ V, the measurement temperature $T=4.2$ K, and the liquid layer was 0.15 mm thick. The charge density far from the deformed section remained practically unchanged. This follows from the fact that the distances between the interference fringes at the edges of the charged surface are the same. This is specially noted in order to underscore the fact that the liquid surface remains an equipotential surface after it is deformed.

The deformed section was stable for 1.2 s, after which it discharged on the bottom plate of the diode. For a 0.1 mm thick liquid layer and $U=400$ V the lifetime of the deformed section decreased to 0.4 s, but once again the lifetime was much longer than the characteristic relaxation time of disturbances in the electron layer above the helium surface.

Figure 2a shows a photograph of the equilibrium profile of a reconstructed surface of a layer of liquid hydrogen with the potential difference between the plates of the diode $U=1620$ V and temperature $T=17$ K. The points in Fig. 2b were obtained by scanning this profile. In a constant field the form of the profile remained unchanged over an observation time of longer than 10^3 s.

The height of the deformed section of the surface (hump) at the center of the diode could be regulated by varying the voltage between the diode plates in the range $U=1300-1700$ V. No surface reconstruction was observed for subthreshold voltages U ($U_{c1}\approx 1300$ V at the given temperature). At voltages above 1750 V the reconstructed surface becomes unstable and a discharge is observed (second critical voltage U_{c2}). At the moment of the discharge, of the order of 10^8 charges arrive at the collector. After the discharge the surface relaxes to the initial flat state. Then the process repeats. In Ref. 11 we reported the observation of quasiperiodic oscillations of the charge surface of liquid hydrogen in strong fields. A similar phenomenon — the appearance of ionic jets (geysers) on the surface of superfluid helium in strong fields — was observed in Ref. 12.

Figure 3 displays the maximum angle of reflection β of a laser beam from the liquid surface, measured at a temperature of 14.6 K, versus the voltage U. One can see that the dependence of the reflection angle on the control voltage $\beta(U)$ changes substantially at voltages above the first critical voltage (in the present measurements $U_{c1}\approx 1500$ V).

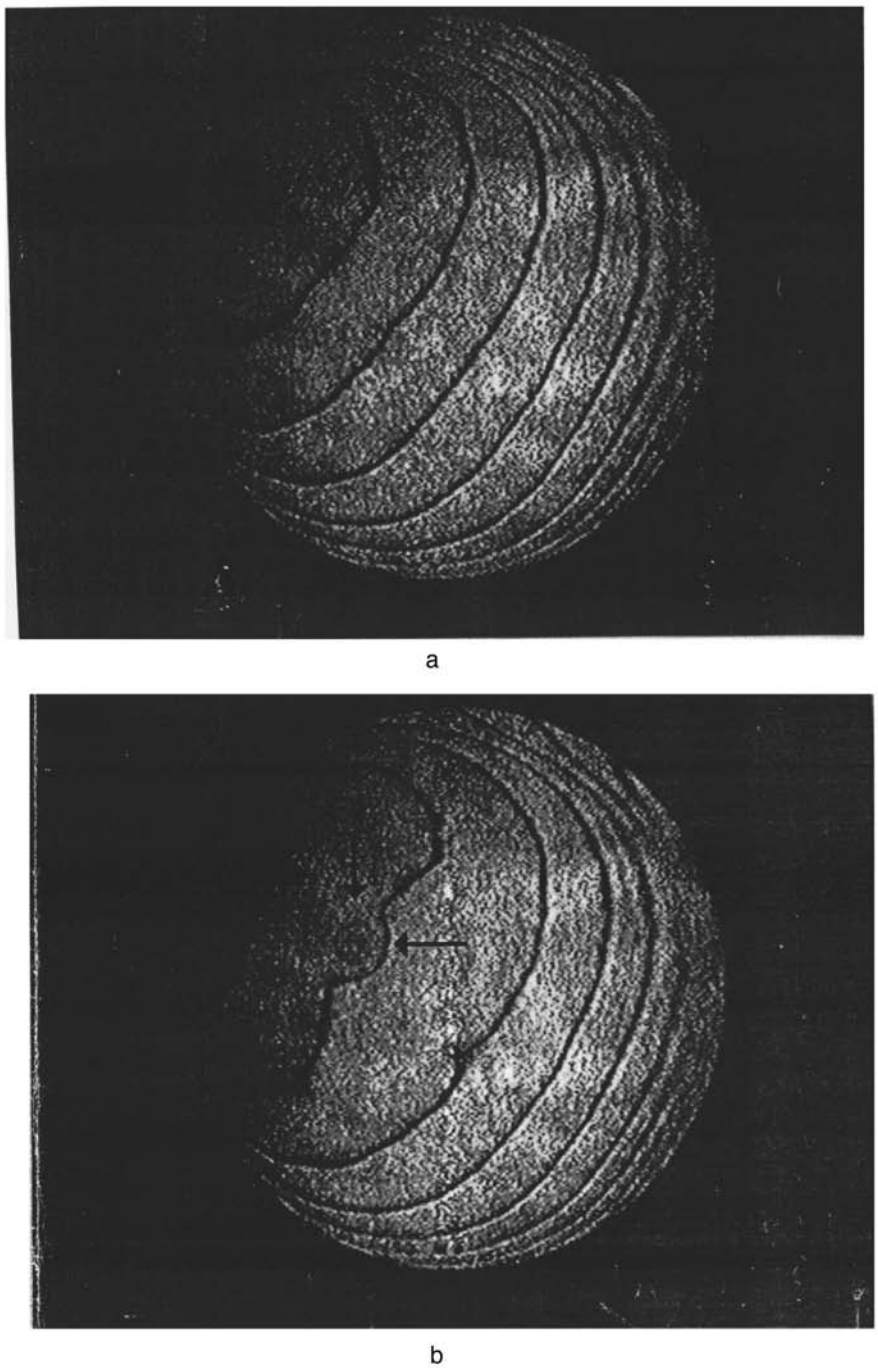

FIG. 1. Interferogram of an exponentially charged liquid-helium surface before (a) and after (b) the formation of a dimple (marked by arrows). Temperature of the liquid — 4.2 K. Diameter of the visible section of the liquid — 20 mm.

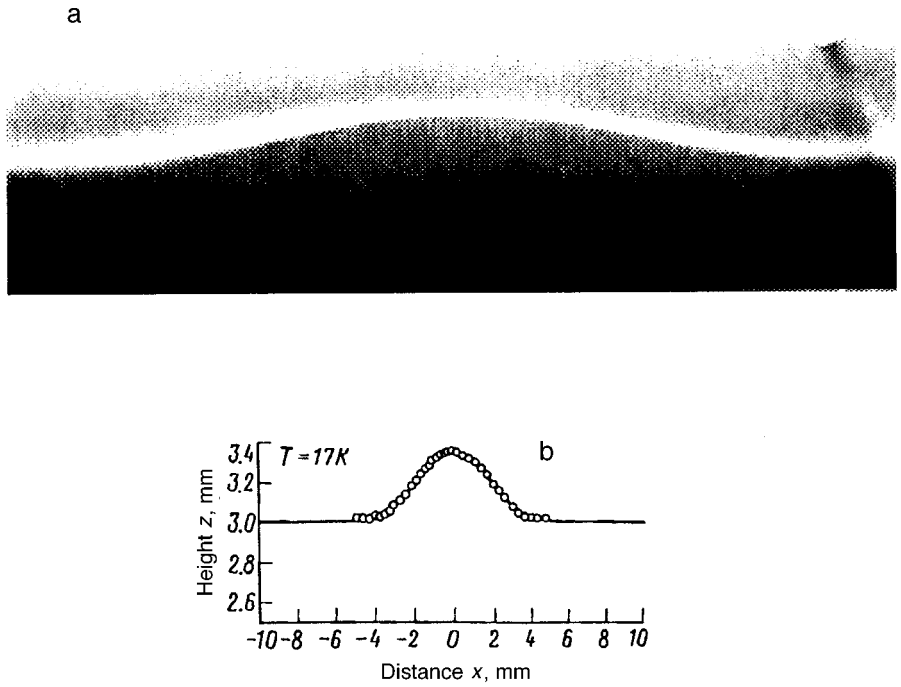

FIG. 2. a) Photograph of the profile of a reconstructed equipotentially charged surface of liquid hydrogen. The linear size in the horizontal direction equals 10 mm. Temperature of the liquid — 17 K. b) Profile obtained for the reconstructed section (hump) by scanning the photograph (circles). Solid line — the function (1) with the parameters $A = 0.38$ mm and $R = 2.5$ mm.

DISCUSSION OF THE RESULTS

First the following important question must be answered. Do the observations repeat the experiments of Ref. 10 where dimples were observed on the surface of a thick ($d \gg \lambda$) helium film on a metal substrate? The answer is unequivocally no.

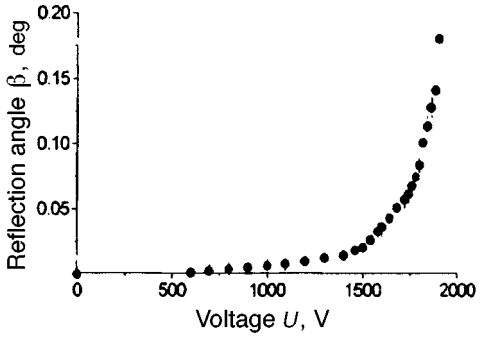

FIG. 3. Maximum angle of reflection of a laser beam from a charged liquid-hydrogen surface as a function of the voltage U. The temperature of the liquid is equal to 14.6 K.

The experimental situation in our work is qualitatively different from the situation observed in Ref. 10 and discussed in Refs. 3 and 4. In our experiments the charge density is determined by the applied voltage (the charges completely compensate the external electric field) and equals the maximum possible density $n=n_c=E^2/4\pi$ on the entire surface, while in Ref. 10 the charge density on a flat surface far from the reconstructed section (dimple) is close to zero, $n \ll n_c$. Moreover, in the experiments with hydrogen the number of charges beneath the surface varies and increases with the applied voltage.

The observations showed that the lifetime of the reconstructed helium and hydrogen surfaces is quite long. This makes it possible to talk about the observation of a stationary charged solitary wave (a dimple in helium or a hump in hydrogen).

A number of qualitative conclusions can be drawn from the experimental results (Figs. 1 and 2).

1) Surface reconstruction in a stationary electric field in a finite-diameter cell with $d \sim \lambda$ is possible with both fixed (helium) and variable (hydrogen) numbers of charges at the surface.

2) Under conditions when the charge density on an equipotential surface is fixed by an external field, a solitary stationary wave — a dimple in the experiments with electrons above a helium surface or a hump in experiments with positive charges beneath a hydrogen surface — arises on the surface in fields exceeding a critical value U_{c1}. The possibility of the appearance of such a wave is predicted in a one-dimensional approximation in Ref. 9.

3) As the field increases further, a pulsed discharge is observed, i.e., there exists a second critical field (and, correspondingly, a voltage U_{c2}) above which the reconstructed surface of the liquid is unstable.

In Ref. 9 the one-dimensional case corresponding to the formation of a periodic system of ''rolls'' on an infinite surface of a thin helium film ($d \ll \lambda$) in a field exceeding some critical field is studied. The shape of a solitary roll (1D soliton), corresponding to an infinitely long period (for the experiment, much greater than the diameter of the experimental cell), is described by the expression

$$z(x)=A\ \cosh^{-2}(x/R), \tag{1}$$

where A is the amplitude and R is the characteristic size of the soliton.

Unfortunately, the computational results obtained in Ref. 9 cannot be used to describe a real, substantially non-one-dimensional situation. Nonetheless, it was found that the form of the hump observed in experiments with liquid hydrogen is described satisfactorily by expression (1), provided that the hump is axisymmetric and x is replaced by the distance r from the center of the soliton. Then R is the characteristic radius of the soliton. Numerical fitting of the profile of the hump (points in Fig. 2b) gave the values $A=0.38$ mm and $R=2.5$ mm (solid curve in Fig. 2b).

The evolution of the shape of the hump with increasing applied voltage can also be judged from the curve $\beta(U)$ in the experiment with hydrogen. From the plot shown in Fig. 3 it is evident that there exist two different regimes of variation of the shape of the free surface of the liquid — below and above the first critical field U_{c1}. The initial section

($U<U_{c1}$) corresponds to the standard drawing of the charged liquid into the field of the capacitor, the reflection angle being proportional to the square of the applied voltage: $\beta \propto U^2$. In fields above the first critical field, i.e., in the region $U_{c1}<U<U_{c2}$, the experimental dependence can be described by the relation $\beta \approx (U-U_{c1})^m$, where the exponent $2<m<3$. This section of the curve $\beta(U)$ describes the change in the slope of the lateral surface of the soliton with increasing voltage U.

In summary, the reconstruction of an equipotential charged surface of a liquid in a stationary electric field above a critical field was observed in the experiments under the conditions $d \sim \lambda$, where d is the distance between the charged surface and the control electrode and λ is the capillary length. For further analysis of the observed phenomenon it could be important that the measurements were performed in a finite-size flat capacitor with diameter much greater than the characteristic lengths d and λ.

This work was supported in part by grants from NASA-RKA (Project No. TM-17) and INTAS-93 (Project No. 93-933).

[a)]e-mail: levch@issp.ac.ru

[1] L. D. Landau and E. M. Lifshitz, *Electrodynamics of Continuous Media*, Pergamon Press, New York [Russian original, Nauka, Moscow, 1982].
[2] L. P. Gor'kov and D. M. Chernikova, JETP Lett. **18**, 68 (1973); Dokl. Akad. Nauk SSSR **228,** 829 (1976) [Sov. Phys. Dokl. **21**, 328 (1976)].
[3] V. I. Mel'nikov and S. V. Meshkov, Zh. Éksp. Teor. Fiz. **82,** 1910 (1982) [Sov. Phys. JETP **55**, 1099 (1982)].
[4] V. B. Shikin and Yu. P. Monarkha, *Two-Dimensional Charged Systems in Helium* [in Russian], Nauka, Moscow, 1989.
[5] P. Leiderer, Phys. Rev. B **20**, 4511 (1979).
[6] M. Wanner and P. Leiderer, Phys. Rev. Lett. **42**, 315 (1979).
[7] P. Leiderer, M. Wanner, Phys. Rev. Lett. A **73,** 185 (1979).
[8] D. M. Chernikova, Fiz. Nizk. Temp. **2,** 1374 (1976) [Sov. J. Low Temp. Phys. **2**, 669 (1976)].
[9] V. B. Shikin and P. Leiderer, Fiz. Nizk. Temp. (in press).
[10] P. Leiderer, W. Ebner, and V. B. Shikin, Surf. Sci. **113**, 405 (1982).
[11] A. A. Levchenko and L. P. Mezhov-Deglin, Fiz. Nizk. Temp. **22,** 46 (1996) [Low Temp. Phys. **22**, 33 (1996)].
[12] V. P. Volodin and M. S. Khaĭkin, JETP Lett. **30**, 572 (1979).

Translated by M. E. Alferieff

Can colliding nerve pulses be reflected?

O. V. Aslanidi and O. A. Mornev
Institute of Theoretical and Experimental Biophysics, Russian Academy of Sciences, 142292 Pushchino, Moscow Region, Russia

(Submitted 26 February 1997)
Pis'ma Zh. Éksp. Teor. Fiz. **65**, No. 7, 553–558 (10 April 1997)

A new effect not previously observed is predicted on the basis of numerical experiments with the Hodgkin–Huxley equations [A. L. Hodgkin and A. F. Huxley, J. Physiol. **117**, 500 (1952)], which describe quantitatively the dynamics of generation, propagation and interaction of nerve pulses: colliding nerve pulse reflection. The range of governing parameters in which the effect might be revealed in real experiments is indicated. © *1997 American Institute of Physics.* [S0021-3640(97)01207-3]

PACS numbers: 87.22.Jb, 03.40.Kf

It is a matter of general experience that the functioning of a living organism as a whole involves the unidirectional transmission of signals—nerve pulses—from receptors to the central divisions of the nervous system involved in information processing (the brain), and further to peripheral executive organs (e.g., muscles). Stability of the process of unidirectional information transmission along nerve fibers (axons) is provided, in particular, by the fact that nerve pulses traveling towards each other along an axon are not reflected after collision but instead decay (are annihilated): if they were reflected, the directed current of signals in a functioning nerve fiber would be irreversibly disorganized in a cascade of re-reflections induced by a single oncoming pulse. Therefore, most physiologists will answer the title question in the negative.

Omitting here the physical mechanisms of generation and propagation of nerve pulses (these mechanisms are already well understood and are explained in detail in the physics literature[1–3]), we recall the cause of the decay of such pulses upon collision: it lies in the fact that following along the nerve fiber in the wake of a traveling pulse front, which reverses the charge of the axon membrane,[a)] there is a refractory zone of finite length, covering the trailing edge and tail of the pulse, where the opposite charge reversal and recovery of the membrane subsystems to the initial resting state occurs. In the refractory zone a nerve fiber is unexcitable, and the existence of these zones prevents two colliding pulses from passing through or reflecting.

In two well-known papers,[1,4] it was proposed to use the annihilation of colliding nerve pulses and of their closest dynamical analogs—combustion waves and concentration waves in chemical media with autocatalysis (they are referred to as autowaves in excitable media[5,6])—as a characteristic feature distinguishing these waves from another type of solitary waves—solitons propagating in conservative dispersive media.[b)] However, do colliding autowaves always decay? Contrary to intuitive expectations, the recent

numerical results[7–9] obtained for simplified mathematical models of excitable media have demonstrated that in such media under certain conditions one can expect the emergence of regimes (called soliton-like), which correspond to reflection of colliding autowaves. These results immediately raise the question of implementation of soliton-like regimes in real biological systems.

The main result of the present work is the prediction of experimental conditions for which the reflection of colliding nerve pulses will occur. The indicated conditions are revealed in numerical experiments with the known system of nonlinear differential equations of Hodgkin and Huxley,[10] which reproduce this effect. These equations give an exact description of the dynamics of nerve pulse propagation, and all the essential results obtained by integration of these equations are supported by experiments not only qualitatively, but quantitatively as well.[11] It is hoped that the reflection of nerve pulses will also be revealed in direct experiments with a real object.

The data presented in this work make it possible to explain the dynamical mechanism of the predicted effect (see below). The results are also of applied interest as it is hoped that investigation of soliton-like regimes in biological excitable media will promote understanding of the mechanisms of a number of pathologies associated with the failure of rhythmical activity in an organism—for example, in the heart, whose contractions, as is known, are initiated by electric excitation waves similar in many respects to nerve pulses.[11,12]

The system of Hodgkin–Huxley equations used in numerical experiments has the form[1,10]

$$CV_t=\frac{a}{2R}\,V_{xx}-\overline{g_{\mathrm{Na}}}m^3h(V-V_{\mathrm{Na}})-\overline{g_{\mathrm{K}}}n^4(V-V_{\mathrm{K}})-\overline{g_L}(V-V_L),$$

$$m_t=\alpha_m(V)(1-m)-\beta_m(V)m,\quad h_t=\alpha_h(V)(1-h)-\beta_h(V)h;$$

$$n_t=\alpha_n(V)(1-n)-\beta_n(V)n; \tag{1}$$

here V is the electrical potential of the inner medium of an axon, measured from the resting potential[c] V_R (the potential of the outer medium is set equal to zero); the subscripts t and x denote time and spatial derivatives; C is the membrane capacitance per unit area; R is the specific internal resistance of a nerve fiber; a is the radius of a nerve fiber; $\overline{g_{\mathrm{Na}}}$, $\overline{g_{\mathrm{K}}}$ and $\overline{g_L}$ are the maximum sodium and potassium conductances of the membrane and the membrane leakage conductance (per unit area of the membrane); V_{Na}, V_{K} and V_L are the sodium and potassium equilibrium potentials and the reversal potential of the leakage current; m and n are kinetic variables of activation of the sodium and potassium currents; h is a kinetic variable of inactivation of the sodium current; the functions $\alpha(V)$ and $\beta(V)$ with subscripts m, h and n determine the rate constants of the corresponding processes at a given V. Standard values of a, C, R, $\overline{g_{\mathrm{Na}}}$, $\overline{g_{\mathrm{K}}}$, $\overline{g_L}$, V_{Na}, V_L and V_R from Ref. 10 and standard expressions for $\alpha_m(V)$, $\beta_m(V)$, $\alpha_h(V)$, $\beta_h(V)$, $\alpha_n(V)$ and $\beta_n(V)$, corrected[d] in Ref. 13, were used. Regimes of pulse propagation and

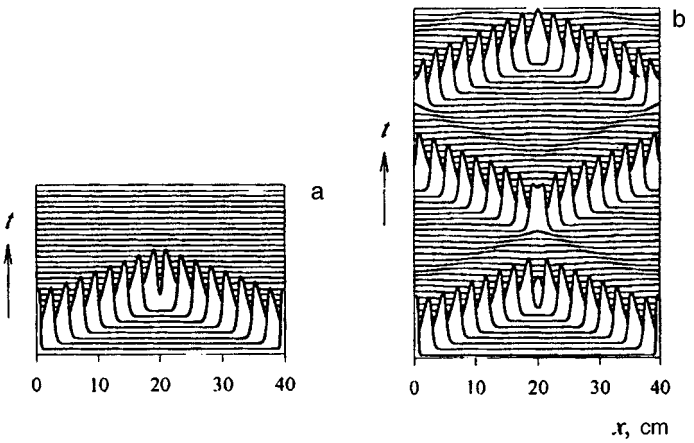

FIG. 1. Interaction of colliding nerve pulses: a) annihilation of pulses at the standard value $V_K = -12.0$ mV; b) reflection of pulses at $V_K = -2.5$ mV. Here and in Figs. 2 and 3 the profiles of the potential $V = V(x,t)$ along the axon at times $t = n\tau$ ($\tau = 2$ ms, $n = 1,2,\ldots$) are shown.

interaction were studied at different values of the parameter V_K. Note that in real experiments, shifts of the V_K value can be implemented by altering the relation between the inter- and intracellular concentrations of potassium ions.[11]

In view of the radical novelty of the effects revealed, let us give a detailed description of the conditions of the numerical experiments. Equations (1) were integrated numerically on the segment $0 \leqslant x \leqslant L$ (with $L = 40$ cm), simulating a nerve axon. At the boundary points $x = 0, L$ zero-flux conditions $\partial V/\partial x = 0$ were imposed. Calculations were performed by the standard explicit method on a mesh consisting of 201 points; the time and space steps of numerical integration were $\Delta x = 0.20$ cm and $\Delta t = 0.01$ ms ($\Delta x = 0.100$ cm and $\Delta t = 0.002$ ms in control experiments). Computations were performed for two cases: (a) nerve pulses were initiated at the left and right ends of the fiber and subsequently traveled toward each other and collided (Fig. 1); (b) a single nerve pulse was initiated at the left end and propagated to the right end (Figs. 2 and 3). The following initial conditions corresponded to case (a): $V = 110$ mV at the extreme points of the space grid, with numbers 0, 1, 2 and 199, 200, 201; $V = V_0$ at all other points; $m = m_0$, $h = h_0$, $n = n_0$ at all grid points (V_0, m_0, h_0 and n_0 are the stationary values of the corresponding variables at a given value of V_K). The initial conditions for case (b) differed from the previous in that the value $V = 110$ mV was specified only at the points with numbers 0, 1, 2.

The results of the numerical experiments are as follows.

For $V_K < -2.5$ mV the usual (annihilation) regime of nerve pulse interaction is implemented in system (1): two pulses traveling toward each other from the ends of the nerve fiber decay after having collided (Fig. 1a), and the steady state $V(x) \equiv V_0$, $m(x) \equiv m_0$, $h(x) \equiv h_0$ and $n(x) \equiv n_0$ is established along the fiber.

For -2.50 mV $\leqslant V_K < -2.46$ mV the soliton-like regime is realized in system (1):

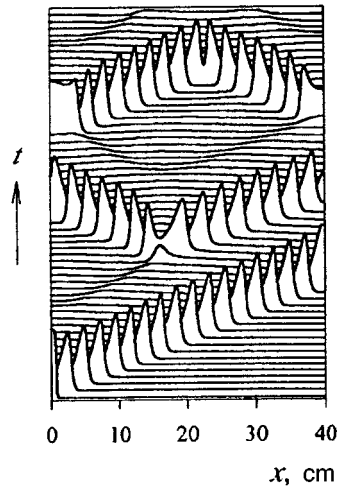

FIG. 2. Generation of extra pulses at $V_K = -2.45$ mV.

two colliding pulses are reflected, move apart in opposite directions (Fig. 1b), collide with the impermeable fiber boundaries, and are reflected once again. Then this cycle recurs again and again. It can be assumed that the soliton-like regime is described by spatially nonuniform time-periodic solutions of the Hodgkin–Huxley equations. The mechanism of pulse reflection is as follows. In the soliton-like regime the traveling pulse presents a doublet consisting of a high-amplitude pulse-leader and a low-amplitude wave following this pulse (Fig. 1b). When doublets interact, the leaders are annihilated, and the collision of the low-amplitude waves after a short delay leads to their summation. As a result of the summation, the potential V at the site of the collisions reaches a super-

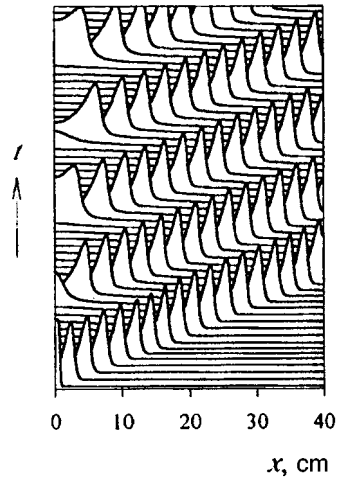

FIG. 3. Self-generation of pulses at $V_K = -2.4$ mV.

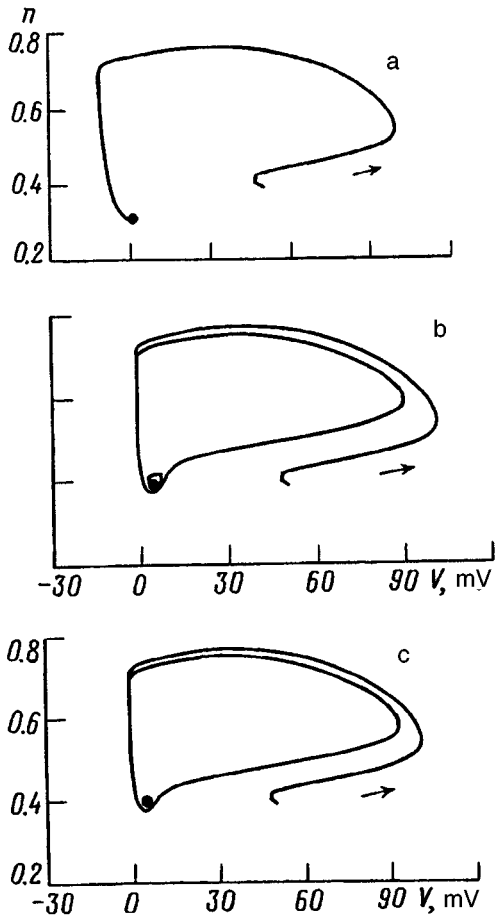

FIG. 4. Projection onto the plane of variables (V,n) of the phase trajectory of a nerve pulse in the system of equations (1) without diffusion, for different values of the parameter V_K. a) $V_K=-12.0$ mV; b) $V_K=-2.5$ mV; c) $V_K=-2.4$ mV. In (a) and (b) a steady stationary point of the system can be seen; in (c) a stable limit cycle emerges as a result of bifurcation at $V_K=-2.42$ mV. In case (b) the soliton-like regime is realized in system (1) with the diffusion term.

threshold value, causing regeneration of the doublets,[e)] which thereafter move apart in opposite directions. The process of reflection of excitation pulses from impermeable fiber ends evolves according to the same scenario.

For -2.46 mV$\leqslant V_K<-2.40$ mV a more complex regime was observed in system (1) (Fig. 2). The amplitude of the wave, following the leader of a doublet initiated at the left end of the fiber, rapidly increases as it travels, reaches the threshold value and initiates two ''extra'' pulses. These pulses move apart to the opposite ends of the axon and are reflected from them. The regime observed after that is similar to the soliton-like one, except that as the regime is in progress, the low-amplitude waves can give rise to new extra pulses which also take part in interactions.

For $V_K \geqslant -2.40$ mV the specifying of initial conditions at the left end of the fiber initiates there a self-generation of pulses which periodically pass along the axon (Fig. 3). This regime is a transitional one: with time the fiber switches to the stable regime of spatially uniform self-oscillations of the electrical potential.

As our numerical studies show, the soliton-like regime is observed in system (1) when the parameters of a system of ordinary differential equations without diffusion,[f] obtained by neglecting the term $aV_{xx}/2R$ in system (1), are close to the bifurcation values corresponding to the global limit-cycle bifurcation. This bifurcation leads to the emergence of a stable limit cycle in the phase space of the system without diffusion, which coexists with a stable stationary state $V=V_0$, $m=m_0$, $h=h_0$, $n=n_0$ which existed before the bifurcation as well (Fig. 4). *Hypothesis:* A necessary condition for the occurrence of soliton-like solutions to nonlinear partial parabolic equations describing excitable media is that the corresponding systems of local kinetic equations be close to the global limit-cycle bifurcation. This condition is satisfied not only for system (1) but also for the systems of Refs. 7–9, where soliton-like regimes have previously been found.

In conclusion let us indicate the conditions for which it can be hoped that the regime of reflection of colliding nerve pulses will be realized in real experiments with axons. It has been shown above that this regime is observed in the range $-2.50\ \text{mV} \leqslant V_K < -2.46$ mV. The latter corresponds to the following interval of K^+ ion concentration in the outer medium bathing the axon: $[K^+]_0^{\min} < [K^+]_0 < [K^+]_0^{\max}$, where $[K^+]_0^{\min} = 10.0$ mM, $[K^+]_0^{\max} = 10.1$ mM. Conversion of the intervals was performed by the Nernst formula[11] $V_K = (RT/F)\ln([K^+]_0/[K^+]_i) - V_R = 58 \log([K^+]_0/120) + 60$ linking the V_K(mV) values with concentration values for the given ions in the outer medium ($[K^+]_0$, mM) and the inner medium of the axon ($[K^+]_i$, mM); here for the temperature T and concentration $[K^+]_i$ we have taken the standard values $T = 280$ K, $[K^+]_i = 120$ mM.[10,11] The reflection of colliding nerve pulses should presumably be pursued in experiments with a fiber placed in a physiological solution with a K^+ concentration in the indicated interval. In spite of the narrow range of $[K^+]_0$ values corresponding to the soliton-like regime ($\Delta[K^+]_0 = [K^+]_0^{\max} - [K^+]_0^{\min} = 0.1$ mM), preparation of a physiological solution with K^+ concentration within the limits of stated accuracy is quite feasible under laboratory conditions. It is possible that the parameters of the real nerve fiber would differ somewhat from that of the ''standard axon'' used in system (1); then the interval of concentrations ($[K^+]_0^{\min}$, $[K^+]_0^{\max}$) corresponding to the soliton-like regime would be also shifted relative to the calculated values. A search for the reflection of colliding nerve pulses in this context is a challenge for the experimenter: the effect should be pursued in the borderline region separating the parameter regions corresponding to the annihilation and self-oscillation regimes.

[a] Recall that in resting state the inner medium of the axon is charged negatively, and at the peak of a nerve pulse—positively.
[b] It is known that conservation laws prohibit annihilation of solitons; in one-dimensional media they escape the interaction undestroyed.
[c] The resting potential is the potential of the inner medium in a steady stationary state of the axon.
[d] In Ref. 13 the non-physical anomalies originally present in the functions given in Ref. 10 have been removed.
[e] Recall that the dynamics of nerve pulse generation has a threshold nature.[11]

[f)]This system of local kinetics describes the dynamics of the process at a small electrically isolated site of the axon.

[1] A. C. Scott, Rev. Mod. Phys. **47**, 487 (1975).
[2] V. S. Markin, V. F. Pastushenko, Y. A. Chizmadzhev, Usp. Fiz. Nauk **123**, 289 (1977) [Sov. Phys. Usp. **20**, 836 (1977)].
[3] V. A. Vasiliev, Y. M. Romanovskiĭ, V. G. Yakhno, Usp. Fiz. Nauk **128**, 625 (1979) [Sov. Phys. Usp. **22**, 615 (1979)].
[4] A. C. Scott, F. Y. E. Chu, D. W. McLaughlin, Proc. IEEE **61**, 1443 (1973).
[5] L. S. Polak, A. S. Mikhaĭlov, *Self-Organization in Nonequilibrium Physico-Chemical Systems* [in Russian], Moscow: Nauka, 1983.
[6] V. I. Krinsky (ed.), *Self-Organization. Autowaves and Structures Far from Equilibrium*, Berlin: Springer, 1984.
[7] V. Petrov, S. K. Scott, K. Showalter, Philos. Trans. R. Soc. **347**, 631 (1994).
[8] J. Kosek, M. Marek, Phys. Rev. Lett. **74**, 2134 (1995).
[9] O. A. Mornev, O. V. Aslanidi, R. R. Aliev *et al.*, Dokl. Akad. Nauk **347**, 123 (1996).
[10] A. L. Hodgkin, A. F. Huxley, J. Physiol. **117**, 500 (1952).
[11] B. I. Khodorov, *General Physiology of Excitable Membranes* [in Russian], Moscow: Nauka, 1975.
[12] D. P. Zipes, J. Jalife, *Cardiac Electrophysiology*, Philadelphia: Sanders, 1990.
[13] B. D. Hassard, N. D. Kazarinoff, Y.-H. Wan, *Theory and Application of Hopf Bifurcation*, Cambridge: Cambridge University Press, 1981.

Translated by the authors

On strategies for opaque and translucent eavesdropping in a quantum-cryptographical system

S. N. Molotkov

Institute of Solid-State Physics, Russian Academy of Sciences, 142432 Chernogolovka, Moscow District, Russia

(Submitted 3 March 1997)
Pis'ma Zh. Éksp. Teor. Fiz. **65**, No. 7, 559–564 (10 April 1997)

The confidentiality of a quantum-cryptographical system based on the energy–time uncertainty relation is discussed with respect to opaque and translucent eavesdropping strategies. © *1997 American Institute of Physics.* [S0021-3640(97)01307-8]

PACS numbers: 03.65.Bz

In quantum cryptography the information carriers are quantum states. It has been proved that it is impossible to clone a state which is unknown beforehand.[1] The secrecy of quantum-cryptographical systems is based on the fact that any measurement on a set of nonorthogonal states that makes it possible to extract nonzero information changes the states.[1,2]

Eavesdropping strategies can be conventionally divided into two types.[3] Opaque eavesdropping reduces to performing a measurement on an information carrier. In the case of translucent eavesdropping, information is extracted from an ancillary state (ancilla), which is prepared and ''attached'' by the eavesdropper to the carrier. Then a measurement is performed on the state of the ancilla.

Different strategies for a quantum-cryptographical system based on two nonorthogonal states have previously been discussed in Refs. 4–6.

In the present letter I wish to propose a physical implementation of a strategy for translucent eavesdropping in a cryptographical system[7] on the basis of nondestructive measurement of the frequency spectrum of the signal.

To describe the state of a one-photon wave packet it is convenient to employ the representation given in Refs. 8–10. The operator of a one-photon wave packet has the form

$$\hat{A}^+(f)=\int_0^\infty f(\omega)\hat{a}^+(\omega)d\omega, \tag{1}$$

where $f(\omega)$ is a complex amplitude and $\hat{a}^+(\omega)$ is an operator, satisfying the Bose commutation relations, that creates a photon in a monochromatic Fock state. The operators $\hat{A}(f)$ and $\hat{A}^+(f)$ also satisfy the Bose commutation relations provided that the amplitude $f(\omega)$ is normalized to 1:

$$\int_0^\infty |f(\omega)|^2 d\omega=1. \tag{2}$$

The field corresponding to a one-photon wave packet is obtained by operating with the creation operator (1) on the vacuum state

$$|1\rangle_f = \hat{A}^+(f)|0\rangle = \int_0^\infty f(\omega)\hat{a}^+(\omega)|0\rangle d\omega = \int_0^\infty f(\omega)|1_\omega\rangle d\omega, \tag{3}$$

where $|1_\omega\rangle$ is a monochromatic one-photon state.

The key generation protocol in the scheme of Ref. 7 consists of sending randomly one of three one-photon wave packets from one legitimate user A to another B. Two packets are narrow-band packets with carrier frequencies ω_1 and ω_2 (logical 0 and logical 1) and spectrum widths $\sigma_{1,2}$ (we assume below that $\sigma_1 = \sigma_2 = \sigma$) and do not overlap (they are orthogonal). The third one-photon wave packet with a short duration and correspondingly a wide frequency spectrum is necessary in order to discover attempts at eavesdropping. The secrecy of the scheme based on nonorthogonal states is guaranteed by a theorem which forbids cloning of such states.[1,2] Such a theorem does not exist for orthogonal states, and for this reason confidentiality is guaranteed by the energy–time uncertainty relation.[7] More precisely, confidentiality is guaranteed by the fact that a time not less than $1/\sigma$ is required in order to detect systematically a one-photon wave packet with a spectral width σ (see, for example, the discussion of different points of view in Refs. 11–15).

The third signal has a spectrum of width $\sigma_\infty \geqslant |\omega_1 - \omega_2|$ and a carrier frequency $\omega_\infty \approx \omega_{1,2}$. The corresponding duration of this signal is $\Delta t \approx 1/\sigma_\infty \ll 1/|\omega_1 - \omega_2|$.

The user B selects in each measurement randomly and independently of A one of two narrow-band photodetectors, tuned to the frequency ω_1 or ω_2, or a wide-band photodetector. After performing a series of measurements the user B reports through an open channel which type of photodetector was used in each separate measurement — narrow- or wide-band, but in the case of narrow-band detectors the user B does not report which detector specifically. The measurements in which narrow-band photodetectors were used give an identical sequence of 0s and 1s — the key. To detect possible eavesdropping attempts, measurements in which A has sent short-duration signals to B are used. The emission time of such signals at A and the arrival time at B are known with accuracy Δt.

To have information about the key an eavesdropper must distinguish 0 from 1 (ω_1 from ω_2). This requires that the measurements be performed with narrow-band photodetectors with a bandwidth of not worse than σ, but according to the uncertainty relation such measurements cannot be performed systematically over times shorter than $\Delta T \geqslant 1/\sigma \gg \Delta t$. Since the user A chooses the signal type randomly, the eavesdropper unavoidably falls into a situation in which he has performed measurements with a narrow-band photodetector, while the signal sent into the line had a wide spectrum. The difference between the emission and arrival times of such a packet is known with accuracy $\Delta t \ll \Delta T$, much better than the delay ΔT introduced by the eavesdropper performing a measurement.

To obtain quantitative estimates, it is necessary to know the specific form of the signals. For definiteness, we shall assume that the spectral shape of all three signals is Gaussian:

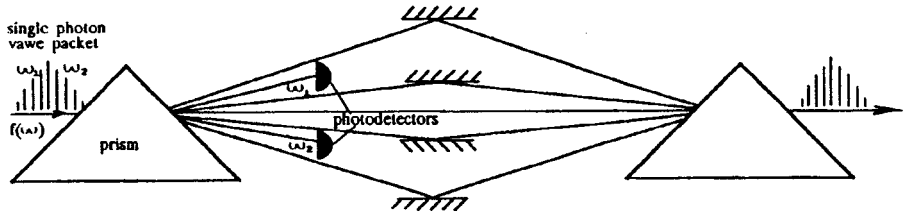

FIG. 1. Qualitative scheme of opaque eavesdropping.

$$f_{1,2,\infty}(\omega)=\frac{1}{(2\pi\sigma_{1,2,\infty}^2)^{1/4}}\ \exp\left(-\frac{(\omega-\omega_{1,2,\infty})^2}{2\sigma_{1,2,\infty}^2}\right). \tag{4}$$

The intensity of a one-photon wave packet can be represented in the form

$$I_{1,2,\infty}(t)=2\frac{\sigma_{1,2,\infty}}{\sqrt{\pi}}\exp(-\sigma_{1,2,\infty}^2t^2). \tag{5}$$

The probability of detecting a photon in a time window ΔT equals

$$P(\Delta T)=\int_0^{\Delta T}I(t)dt=\Phi(\sigma_{1,2,\infty}\Delta T),\quad \Phi(x)=\frac{2}{\sqrt{\pi}}\int_0^x\exp(-t^2/2), \tag{6}$$

where $\Phi(x)$ is the error integral.

Formula (6) is an estimate of the time of occurrence of an event (detection) on the basis of the Mandel'shtam–Tamm relations.[12] For experiments of this type, when the detector operates in a waiting mode and the experiment stops when the awaited event has occurred, the estimate (6) is, of course, valid (see the discussion in Ref. 15).

If a wide-band signal is detected, then the probability that a one-photon wave packet enters the detector in the time window ΔT is described by the function $\Phi(\sigma_\infty\Delta T)$, which rapidly approaches 1 if $\Delta T\geqslant 3\sigma_\infty$. The latter fact means that for a short signal, time delays ΔT exceeding $3\sigma_\infty$ are detected with a probability close to 1. The variance of the measurement times of narrow-band signals cannot be less than the waiting time for the event to occur. The latter time is not less than the reciprocal of the width of the signal spectrum $\approx 1/\sigma$ (the time required for a one-photon wave packet to ''pass'' into the detector). A measurement of a wide-band signal by an eavesdropper using a narrow-band photodetector with bandwidth σ reduces to cutting out from the wide spectrum (with a filter, for example) a line of the order of σ and then detecting it. The probability of detecting a narrow band from a wide spectrum over a time ΔT does not exceed $P(\Delta T)\leqslant|f_\infty|^2\Phi(\sigma\Delta T)\leqslant(\sigma/\sigma_\infty)\Phi(\sigma\Delta T)$ (here $f_\infty\approx 1/\sqrt{\sigma_\infty}$ is the amplitude of the wide-band signal at the maximum).

The measurement scheme for opaque eavesdropping is displayed qualitatively in Fig. 1.

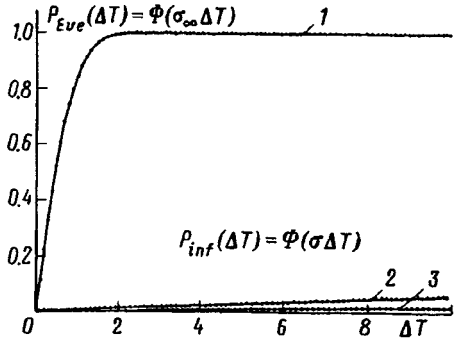

FIG. 2. Probabilities of detecting an eavesdropper $P(\Delta T)_{\mathrm{Eve}}=(\sigma_\infty/\sigma)(\sigma/\sigma_\infty)\Phi(\sigma\Delta T)$ (curve *1*), where $N\sim\sigma_\infty/\sigma$. Curves *2* and *3* — probabilities that an eavesdropper obtains information about one bit in the key $P_{\mathrm{inf}}(\Delta T)\approx(\sigma/\sigma_\infty)\Phi(\sigma\Delta T)$. The parameter ratios σ/σ_∞ are 0.005 and 0.001 for curves *2* and *3*, respectively. These values correspond to narrow-band signal spectrum widths $\sigma=5$ ns^{-1} and 1 ns^{-1} and a wide-band signal duration of 1 ps.

After the one-photon wave packet has been decomposed into a spectrum, during each measurement an eavesdropper can ''insert'' photodetectors into the trajectories corresponding to the frequencies ω_1 and ω_2 for a time ΔT (the triggering waiting time).

If one of the narrow-band signals is present in the line, then the eavesdropper records a photon over the triggering waiting time ΔT with probability $\Phi(\sigma\Delta T)$ and possesses information about a given bit in the key. If, however, a wide-band signal is present in the line, then any of two photodetectors can be triggered. The triggering probability over the waiting time ΔT equals $P(\Delta T)=\sigma|f_\infty(\omega_{1,2})|^2\Phi(\sigma\Delta T)\approx(\sigma/\sigma_\infty)\Phi(\sigma\Delta T)\ll 1$.

The probability of detecting a wide-band signal with a narrow-band photodetector is low: $p\approx\sigma/\sigma_\infty\ll 1$. Correspondingly, the probability that a detector is not triggered is $q\approx 1-\sigma/\sigma_\infty$. If there are N transmissions of a wide-band signal, then the probability of detection in m experiments is given by the Bernoulli distribution $P_m=C_N^m p^m q^{N-m}$. The probability of detection in at least one of N experiments equals $P(N)=1-(1-\sigma/\sigma_\infty)^N$ and approaches 1 for $N\approx\sigma_\infty/\sigma$. Therefore if only one of the narrow-band signals is sent on N wide-band probe signals and the eavesdropper expects in each measurement a detection within a time ΔT, then the probability of detecting the eavesdropper is $P_{\mathrm{Eve}}(N)=P(N)\Phi(\sigma_\infty\Delta T)\approx 1$. At the same time, the probability that an eavesdropper obtains information over the waiting time ΔT equals $P_{\mathrm{inf}}=\Phi(\sigma\Delta T)\ll 1$. Plots of the functions $\Phi(\sigma\Delta T)$ and $\Phi(\sigma_\infty\Delta T)$ for different values of the ratio σ/σ_∞ are presented in Fig. 2.

We shall now discuss a strategy for translucent eavesdropping. The measurement scheme is displayed in Fig. 3. After decomposition into a spectrum, each monochromatic mode is directed into a Kerr cell (the application of Kerr cells in nondestructive measurements is discussed in Ref. 16, for example). An auxiliary probe field is also passed through the Kerr cells and a measurement is then performed on the probe field. The Hamiltonian describing the interaction of probe fields with the monochromatic modes

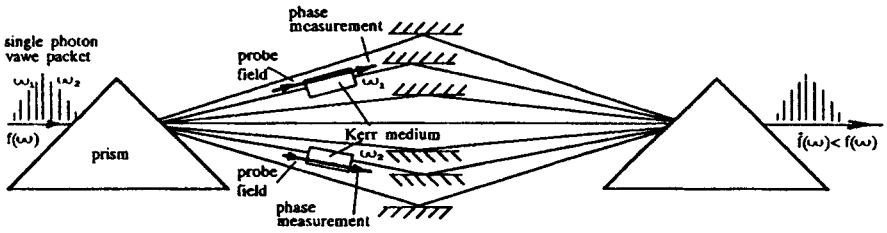

FIG. 3. Qualitative scheme of translucent eavesdropping.

from a one-photon wave packet, after passage through the prism, has the form

$$\hat{H}=\sum_i \chi_i^{(3)}\hat{N}_i\hat{n}_{\omega_i}, \tag{7}$$

where $\chi_i^{(3)}=\chi_i^{(3)}(-\omega_i;\omega_i,-\omega_{pi},\omega_{pi})$ is the third-order nonlinear susceptibility, ω_{pi} and ω_i are the frequencies of the probe field and the ith monochromatic component of the one-photon wave packet, $\hat{N}_i$ is the operator of the number of photons in the ith probe field, and $\hat{n}_{\omega_i}$ is the operator of the number of photons in ith monochromatic one-photon mode in a wave packet. The combined evolution of the probe fields and the monochromatic modes in the cells is described by the evolution operator

$$\hat{U}=\exp\left(i\sum_k \chi_k\hat{N}_k\hat{n}_{\omega_k}\delta t_k\right), \tag{8}$$

where $\delta t_k=L_k/v_k$, v_k is the velocity of light in the cell, L_k is the length of the cell, and $\tilde{\chi}_k=\chi_k^{(3)}L_k/v_k$. Let the probe fields be described by the state vectors $|\Psi_k\rangle$. Since the fields are independent, the general state vector is

$$|\Psi\rangle=\prod_k |\Psi_k\rangle. \tag{9}$$

The effect of the evolution operator on the state of a one-phonon wave packet and probe fields reduces to the following:

$$|\Phi\rangle=\hat{U}|1\rangle_f|\Psi\rangle=\sum_i f(\omega_i)|1_{\omega_i}\rangle\exp(i\tilde{\chi}_i\hat{N}_i)\prod_{j\neq i}|\Psi_j\rangle. \tag{10}$$

Now let the eavesdropper and the user B perform measurements with the aid of the projection operator

$$\hat{P}=\left(\sum_i |1_{\omega_i}\rangle\langle 1_{\omega_i}|\right)(|\Psi\rangle\langle\Psi|). \tag{11}$$

For B such a measurement means using a wide-band photodetector, and for the eavesdropper the measurement reduces to projecting the probe fields onto the initial state. If the probe fields were not ''attached'' to the carrier ($\hat{U}\equiv 1$), then the probability of outcomes measurements with $\hat{P}$ equals 1 ($|\langle\Phi|\hat{P}|\Phi\rangle|^2=1$ — the fields are definitely in

the initial state). The probability that user B detects a photon in each measurement also equals 1. However, if Kerr cells were used, then the probability of a such measurement is

$$P=\sum_i |\tilde{f}(\omega_i)|^2<1, \quad \tilde{f}(\omega_i)=\langle\Psi_i|\exp(i\tilde{\chi}_i\hat{N}_i)|\Psi_i\rangle. \tag{12}$$

Formula (12) can apparently be interpreted as a decrease in the probability of detecting a photon at the receiving end of the line (see also Ref. 17).

If a coherent state

$$|\Psi_i\rangle=\exp(-|\alpha_i|^2/2)\sum_{k=0}^{\infty}\frac{\alpha_i^k}{\sqrt{k!}}|k\rangle, \tag{13}$$

where the average number of photons is $\langle\hat{N}_i\rangle=|\alpha_i|^2$, is used as a probe state, then after a measurement on the probe field the amplitude of the one-photon wave packet becomes

$$|\tilde{f}(\omega_i)|^2=|f(\omega_i)|^2|\exp[(\exp(i\tilde{\chi}-1))|\alpha_i|^2]|\approx|f(\omega_i)|^2\exp(-\langle\hat{N}_i\rangle\tilde{\chi}_i^2/2)<|f(\omega_i)|^2. \tag{14}$$

In this formula, for a coherent probe field, the decrease in the amplitude is limited by the product $\langle N\rangle\tilde{\chi}^2$, which cannot be less than 1, in the exponential.[17–20] The situation is analogous for other types of fields.[17–20] Such an unavoidable decrease in amplitude follows from the principle of complimentarity and is unavoidable price to be paid for information about whether or not a photon has ''passed'' along a given trajectory (the given spectral component is different from zero).

In the case of a wide-band signal, the eavesdropper with a translucent strategy effectively decreases the amplitude in an interval $\sim\sigma$ in the region of the spectral components ω_1 and ω_2. The fraction of these states in a one-photon packet is of the order of $\sim\sigma/\sigma_\infty\ll 1$. The probability that part of the spectrum is ''cut out'' in a nondestructive measurement by the eavesdropper in a given experiment does not exceed $\delta\omega|f_\infty(\omega_{1,2})|^2|\langle\Psi|\exp(i\tilde{\chi}\hat{N})|\Psi\rangle|^2\leqslant(\sigma/\sigma_\infty)\ll 1$, where $\delta\omega\approx\sigma$. Therefore the probability of detecting translucent eavesdropping when sending a single wide-band signal is low and equals, in order of magnitude, $\sigma/\sigma_\infty\ll 1$. We note that for an eavesdropper the probability of detecting a change in phase of the probe field in a measurement of a wide-band signal is likewise small to the extent that $\delta\omega|f_\infty(\omega_{1,2})|^2$ is small. Just as in the case of opaque eavesdropping, to detect an eavesdropper with a probability close to 1 the fraction of the wide-band probe signals with respect to narrow-band signals must be $\sigma_\infty/\sigma\gg 1$.

In closing, I wish to thank B. A. Volkov, S. V. Iordanskiı, G. B. Lesovik, S. S. Nazin, S. T. Pavlov, and I. I. Tartakovskiı for fruitful discussions in the course of this work. This work is supported by the Russian Fund for Fundamental Research, Project No. 96-02-19396.

[1] W. K. Wotters and W. H. Zurek, Nature **299**, 802 (1982).
[2] C. Bennett, Phys. Rev. Lett. **68**, 3132 (1992); C. H. Bennett, G. Brassard, and N. D. Mermin, Phys. Rev. Lett. **68**, 557 (1992).
[3] A. K. Ekert, B. Huttner, G. M. Palma, and A. Peres, Phys. Rev. A **50**, 1047 (1994).

[4] C. H. Bennett, Tal Mor, and J. A. Smolin, ''Parity bit in quantum cryptography,'' http://xxx.lanl.gov/quant-ph/9604040.
[5] E. Biham and Tal Mor, ''On the security of quantum cryptography against collective attack,'' http://xxx.lanl.gov/quant-ph/9605007.
[6] Hoi-Kwong Lo and H. F. Chau, ''Quantum cryptography in noisy channels,'' http://xxx.lanl.gov/quant-ph/9511025.
[7] C. N. Molotkov and S. S. Nazin, JETP Lett. **63**, 924 (1996); S. N. Molotkov, JETP Lett. **64**, 702 (1996); also http://xxx.lanl.gov/quant-ph/9612013; /9612012.
[8] U. M. Titulaer and R. J. Glauber, Phys. Rev. **145**, 1041 (1966).
[9] H. Fearn and R. Loudon, Opt. Commun. **64**, 485 (1987); H. Fearn and R. Loudon, J. Opt. Soc. Am. B **6**, 917 (1989).
[10] R. A. Campos, B. E. Salech, and M. Teich, Phys. Rev. A **42**, 4127 (1990).
[11] N. Bohr, in *Selected Scientific Works* [Russian translation], Nauka, Moscow, 1971, Vol. 2, p. 675.
[12] L. I. Mandel'shtam and I. E. Tamm, Izv. Akad. Nauk SSSR Ser. Fiz. **9**, No. 1/2, 122 (1945).
[13] N. S. Krylov and V. A. Fok, Zh. Éksp. Teor. Fiz. **17**, 93 (1947); V. A. Fok, Zh. Éksp. Teor. Fiz. **42**, 1135 (1962) [Sov. Phys. JETP **15**, 784 (1962)].
[14] V. V. Dodonov and V. I. Man'ko, Tr. Fiz. Inst. Akad. Nauk SSSR **183**, 52 (1987).
[15] A. S. Kholevo, *Probabilistic and Statistical Aspects of Quantum Theory* [in Russian], Nauka, Moscow, 1980.
[16] N. Imoto, H. A. Haus, and Y. Yamamoto, Phys. Rev. A **32**, 2287 (1985); M. Kitagawa, N. Imoto, and Y. Yamamoto, Phys. Rev. **35**, 5270 (1987); I. L. Chuang, and Y. Yamamoto, Phys. Rev. Lett. **76**, 4281 (1996).
[17] Z. Y. Ou, Phys. Rev. Lett. **77**, 2352 (1996).
[18] C. W. Helstrom, *Quantum Detection and Estimation Theory*, Academic Press, New York, 1976.
[19] R. Loudon, *The Quantum Theory of Light*, Clarendon Press, Oxford, 1973.
[20] A. S. Lane, S. L. Braunstein, and C. M. Caves, Phys. Rev. A **47**, 1667 (1993).

Translated by M. E. Alferieff